Lockheed

HUNTSVILLE RESEARCH & ENGINEERING CENTER

LOCKHEED MISSILES & SPACE COMPANY, INC.

A SUBSIDIARY OF LOCKHEED AIRCRAFT CORPORATION

HUNTSVILLE, ALABAMA

HREC-6772-1
LMSC-HREC D225700-I

LOCKHEED MISSILES & SPACE COMPANY

HUNTSVILLE RESEARCH & ENGINEERING CENTER

HUNTSVILLE RESEARCH PARK

4800 BRADFORD DRIVE, HUNTSVILLE, ALABAMA

STUDY OF AERODYNAMIC SURFACE CONTROL OF SPACE SHUTTLE BOOST AND REENTRY

VOLUME I

FINAL REPORT

March 1972

CR-123644

Contract NAS8-26772

by

C. J. Chang
C. L. Connor
G. P. Gill

APPROVED: C. J. Trautwein

W. Trautwein, Supervisor
Vehicle Dynamics & Control Section

T. R. Beal

T. R. Beal, Manager
Dynamics & Guidance Department

George D. Perry

for J. S. Farrior
Resident Director

FOREWORD

This report presents the work performed during the period of April 1971 to March 1972 by Lockheed's Huntsville Research & Engineering Center while under contract to the National Aeronautics and Space Administration for the Aero-Astrodynamics Laboratory of Marshall Space Flight Center (MSFC), Contract NAS8-26772.

Mr. J.M. Livingston of NASA-MSFC, Aero-Astrodynamics Laboratory, S&E-AERO-DF, was the MSFC Contracting Officer's Representative for the ascent portion of this study. Mr. R. C. Lewis of NASA-MSFC, Aero-Astrodynamics Laboratory, S&E-AERO-DOA, was the Contracting Officer's Representative for the reentry portion of the study. Mr. G. P. Gill was the project engineer at Lockheed. Major contributors were Dr. C. J. Chang, Dr. W. Trautwein and Mr. C. L. Connor. The hybrid programming was performed by Mr. D. C. Cruse and Mr. A. M. Hansing. Mr. K. R. Leimbach, Mr. W. G. Green, Mr. P. O. McCormick and Mr. J. B. Baker provided assistance in establishing payload sensitivities.

This report is divided into two volumes. Volume I presents the optimization technique, the problem formulation and the results obtained. Volume II presents all the Appendices which describe derivations of mathematical models and all peripheral studies related to contract performance.

PRECEDING PAGE BLANK NOT FILMED

CONTENTS

CONTENTS (Continued)

Section 1
INTRODUCTION AND SUMMARY

1.1 OVERVIEW OF ENTIRE STUDY

The basic problem to which Lockheed has addressed itself in this study is one of applying modern optimal control techniques to design shuttle booster engine reaction control systems and aerodynamic control systems for both ascent and reentry. Furthermore, since each type control system has its own region of relatively major effectiveness due to the extreme range of environmental parameters, an area must exist between these in which a transition is made. This introduces a second problem with which this report is concerned; that of optimal blending of engine reaction control and aerodynamic control. Very little has previously been known concerning this control blending problem including such basic items as what criterion should be used to judge the relative "goodness" of a blending scheme. The basic criterion for both design problems (individual control system design and the blending of the two) that was selected by Lockheed was that of reducing control system related weight penalties.

A very powerful design tool has been developed by Lockheed over the past several years, which allows direct design goals to be represented in a performance functional which, in turn, is used with optimal control techniques to design practical control systems. This design procedure is carried out on a hybrid computer. In order to permit substantial savings in manhours and computer time in future applications, considerable effort was expended under this contract in developing a very advanced computer software package that largely automated the handling of the raw data through to computer setup and checkout.

As mentioned above, the design approach taken was that of reducing control system weight related penalties. Since most of the required weight sensitivities were not available, experts from various disciplines were brought in for their derivations from available data. Each of these peripheral studies were reviewed, analyzed and reduced to a form appropriate for the high-speed simulations required for the optimizations. General analyses were then performed so that designers could be made aware of the most significant areas with which to be concerned and at an early stage of design work.

1.2 SUMMARY OF RESULTS

A very versatile total hybrid software package was developed that significantly reduces off-line engineering involvement, and produced very rapid data processing through complete setup and checkout of the hybrid program. The Lockheed direct optimization scheme was incorporated into this package for investigations of the three axis engine reaction control systems for both ascent and reentry of fully reusable "Phase B" Space Shuttle Configurations.

Major control system related weight penalty sensitivities were generated. Analysis of these sensitivities indicated that for ascent, the most significant parameter was the structural weight required to carry the booster/orbiter interface loads during the latter portion of the launch trajectory. Other weight penalties of lesser importance that were neverthelessiincluded in the ascent simulation were due to main engine gimbal angle requirements and trajectory position and velocity deviations. Analysis of the sensitivities for the reentry portion indicated that the most significant control system related weight penalties were associated with the hybraulic system as dictated by elevon deflection, deflection rate and rudder deflection rate. Furthermore, these become significant only in the transonic region of the reentry trajectory and may be largely ignored in favor of auxiliary propulsion fuel considerations, another direct weight penalty, until this period. Other sensitivities analyzed and included in the reentry control study were the thermal

protection system (TPS) firing and nonfiring effects, TPS requirements related to aerodynamic control surface deflection rates, and structural weight associated with aerodynamic control surface deflection angles.

1.3 OUTLINE OF THE REPORT

Section 2 describes the optimization technique and its various options of operating over a total trajectory in one or several sequential steps using a floating optimization time interval, of using either a single or a two-level minimization scheme, and of generating either constant control gains or gain rates. Grid and gradient search operations, sensitivity reduction to uncertainties and performance evaluation capability are described briefly.

Section 3 is the complete formulation of the ascent study. Included are derivations of the 6D perturbation equations of motion, the control and blending law selection and a large subsection describing and analyzing the ascent control related penalties. Driving functions for the optimization process were two synthetic wind profiles. Structural loads at the booster/orbiter interface were found to have a significant impact on shuttle booster structural weight and payload injection weight. Much of the work on the ascent portion of this study was performed under another contract which is reported in Ref. 2.

Section 4 is the formulation of the reentry portion of this study. It includes derivation of the 6D perturbation equations of motion and the process followed in the control and blending law selections. A subsection contains the derivation and description of a tool whereby initial gains for 3-axes APS and aerodynamic control gains are synthesized as time-varying quantities for the entire reentry trajectory. These gains were used as initial guesses for the optimization, thereby ensuring initial stability and giving a good intuitive starting point for the process. The final subsection describes in detail derivations of the various reentry control related weight penalties and analyzes their relative effectiveness. The most significant of

these were hydraulic system effects related to elevon deflection, deflection rate and rudder deflection rate during the transonic portion of reentry. Other sensitivities analyzed but determined to be of relatively less importance are TPS weight related to engine firings and aerodynamic surface deflection rates and structural weight associated with aerodynamic control surface deflection angles.

Section 5 contains a detailed description of Lockheed's total hybrid software concept as applied to the incident study. This concept was developed to overcome several common problems in hybrid and analog computation that are notorious time consumers, both of manhours and machine time. The net effect is to permit an engineer to be relieved of most of his ordinary involvement during the problem programming and checkout phases as well as to speed up this process through automatic programming methods. Furthermore, computer setup and checkout time is drastically reduced even for vehicle or trajectory changes where little or no wiring changes are required. Maximum engineering interface is brought back in at the hybrid simulation level after checkout so that rapid engineered solutions may be found to the design problem. Program language and construction are designed for maximum versatility and ease of off-line programming modification with high-speed on-line processing.

Section 6 discusses the results of the two phases of the optimization study.

Section 7 contains the conclusions and recommendations obtained from this study.

Section 8 lists all references cited, as well as others which were employed in the performance of this contract.

Section 2
OPTIMIZATION APPROACH

2.1 BASIC SCHEME

The basic scheme of the Hybrid Optimization program is a direct optimization method, whereby only forward integrations of the dynamic equations are performed. The vehicle system dynamics and control system loops are simulated on the analog console of a hybrid computer as shown schematically in Fig. 2.1-1. During each simulation, the performance is evaluated by computing the performance index, J, which has been selected to best reflect the design objectives. After the simulation, J is transferred to the digital console where a minimization scheme is programmed to determine the minimum of J with respect to the adjustable parameters, namely the controller gain slopes.

2.2 UPDATE INTERVAL

During development of the hybrid optimizer, it was found that although optimal results were obtained by carrying out the optimization over the total flight time as one interval, better engineered results could be obtained by optimizing over a number of limited time intervals independently. For the ascent portion of this study, the total flight time was therefore divided into a finite number of update intervals of length $(t_{\nu+1} - t_{\nu}) = \Delta t$ of typically 5 seconds as indicated in Fig. 2.2-1.

While rigorous optimal gain schedules as obtained from calculus of variations will be general functions of time, the class of optimal gain schedules to be generated by the present method was restricted to piecewise linear

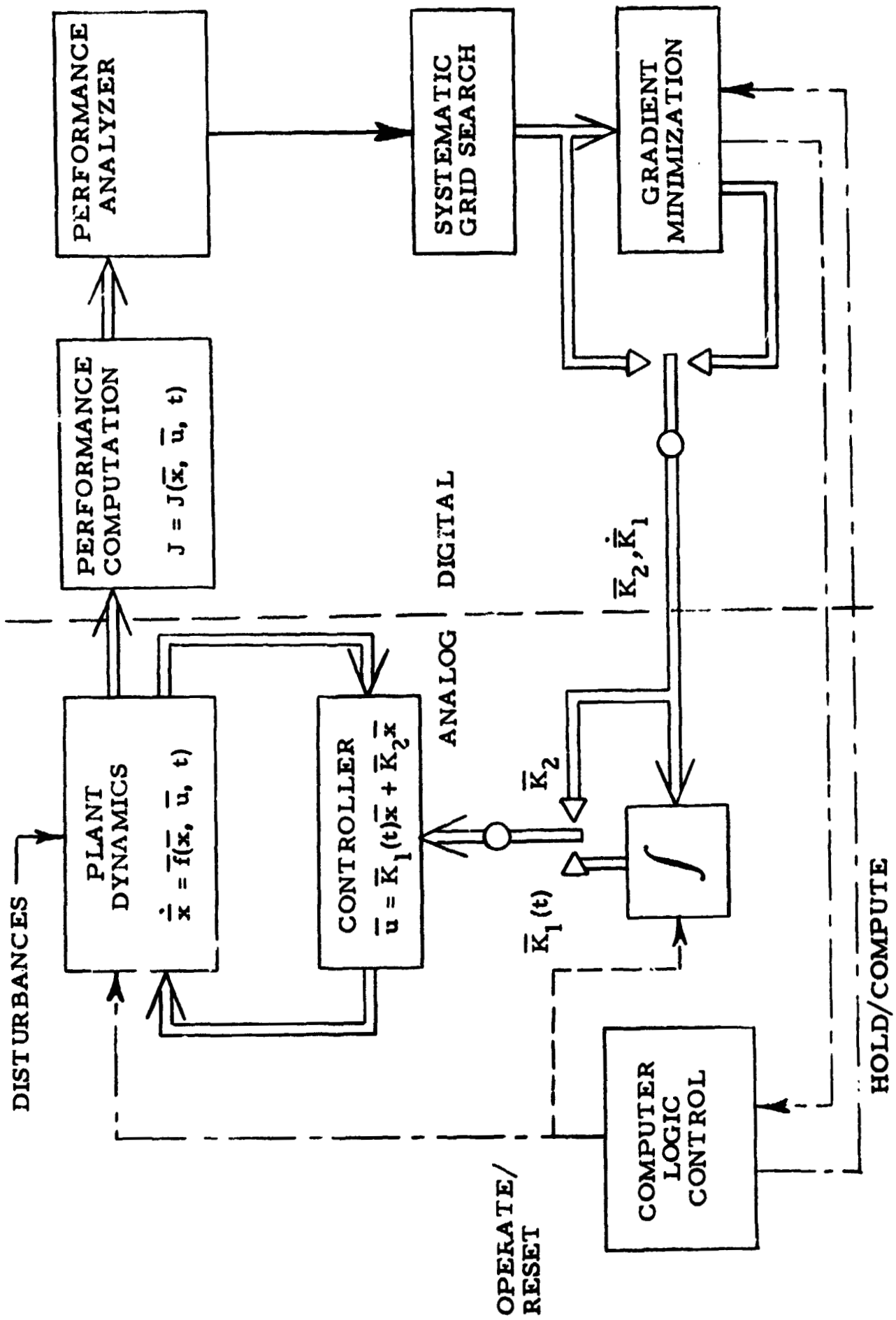

Fig. 2.1-1 Basic Control System Optimization Scheme

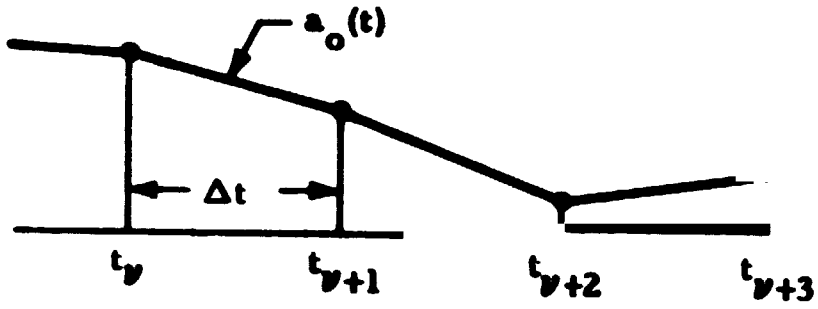

Fig. 2.2-1 - Desired Polygonal Form of Optimal Gain Schedules

functions of time as in Fig. 2.2-1. This largely reduces the computational load and at the same time keeps the resulting optimal schedules closer to a practical form more suitable for implementation. Piecewise constant schedules, as defined at break points t_ν, $t_{\nu+1}$, ..., have been found to be unacceptable in this approach because of the transients generated from large numbers of step-type gain changes.

2.3 OPTIMIZATION INTERVAL

At each update time, t_ν, the optimizer performs a series of fast-time forward integrations while iteratively adjusting the controller gain slopes in order to evaluate the vehicle performance. A minimum duration is required for these forward integration intervals. Methods to establish this minimum look-ahead time interval, T, were discussed in Section 6 of Ref. 1. For the ascent shuttle dynamics, the minimum value of T which sufficiently detects the significant effects of a particular set of gain schedules is between 15 and 20 sec. Figure 2.3-1 shows a general example.

As sketched in Fig. 2.3-2, a number of slopes for each controller gain is simulated by fast-time forward integrations of the system dynamics with period T. The gradient optimization technique chooses the optimum slope originating at t_ν, based on the J function, then the system dynamics are integrated in real time to $t_{\nu+1}$ at which time the process is repeated. Final optimization results yield for each controller gain being optimized a polygonal form as shown in Fig. 2.2-1.

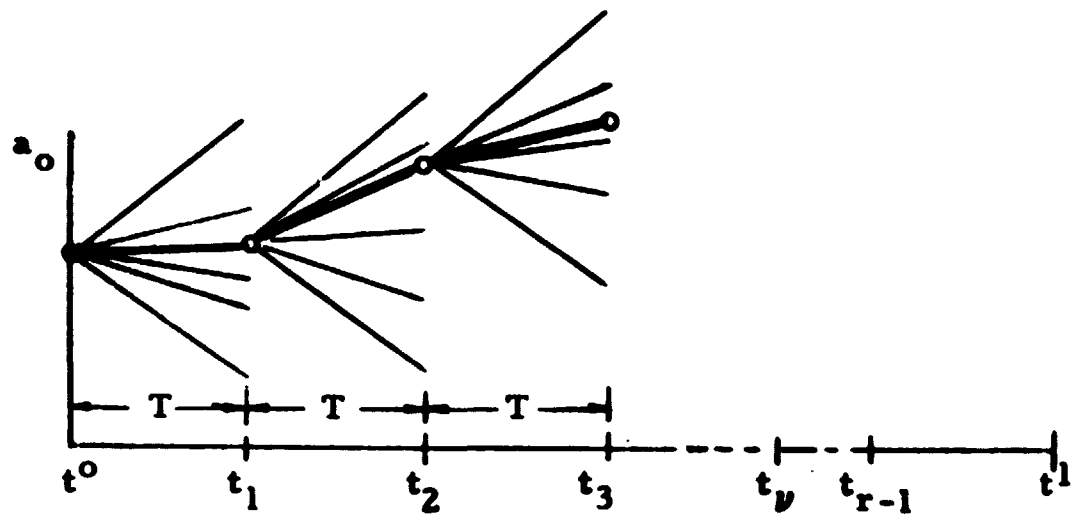

(a)

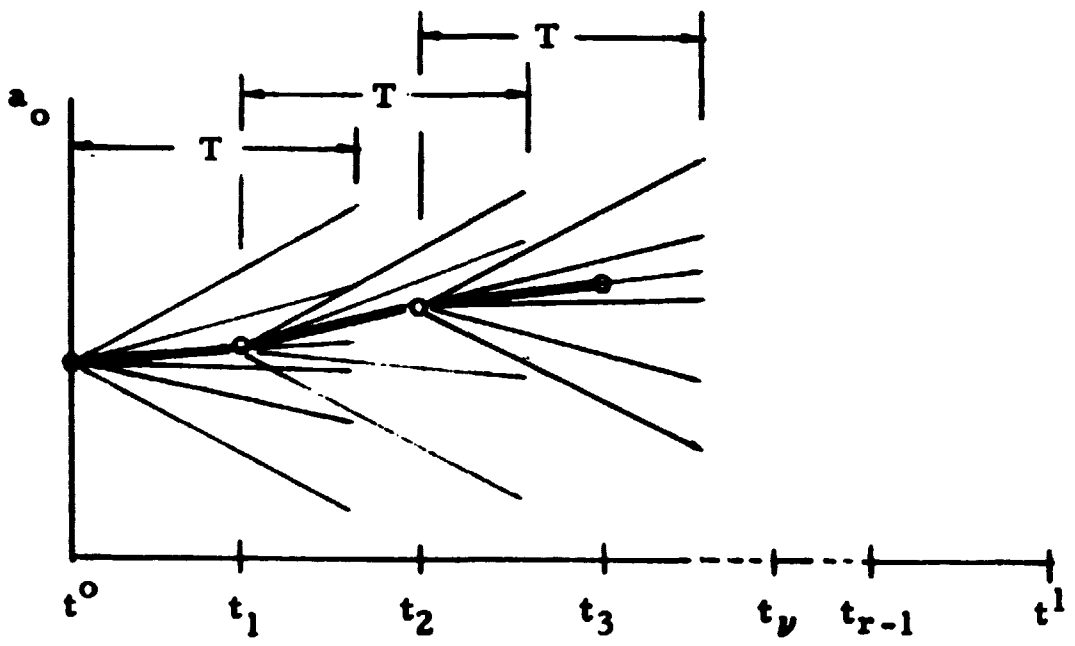

(b)

Fig. 2.3-1 - Total Mission Time (t^o, t^1) Broken Down into Finite Number r of Updating Intervals (t^o, t_1), (t_1, t_2), . . . , $(t_\nu, t_{\nu+1})$ (t_{r-1}, t^1). Optimization Intervals $(t_\nu, t_\nu+T)$ are identical to updating intervals $(t_\nu, t_{\nu+1})$ as in (a) or are longer than updating intervals as in (b).

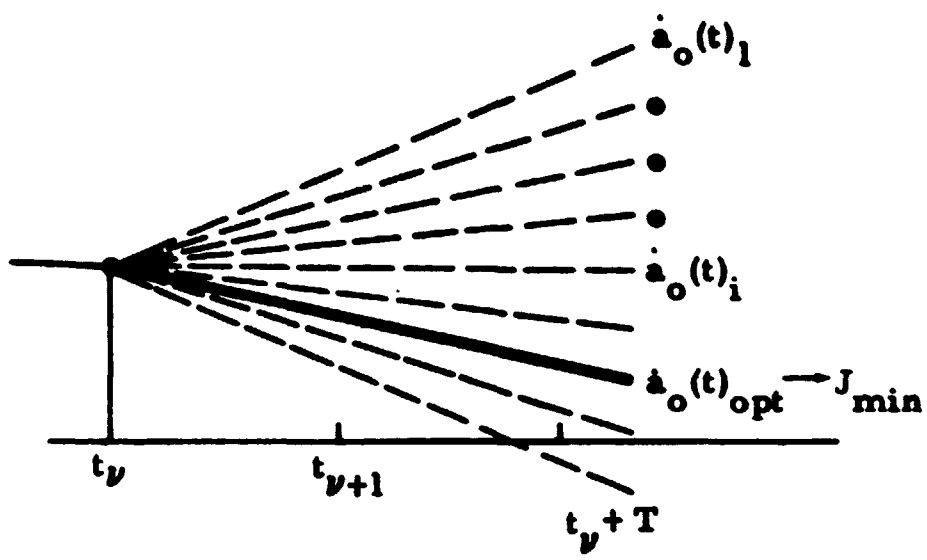

Fig. 2.3-2 - During Optimization Cycle at Flight Time, t_ν, a Large Number of Linear Gain Schedules are Evaluated for their Load Relief Performance

2.4 GRID SEARCH

In earlier development stages of the optimizer, it was found that the gradient technique ran the risk of finding local minima rather than absolute minima for given dynamics and performance index J. Modifications to avoid this problem resulted in a systematic grid search being added to the program. A two-dimensional case is shown in Fig. 2.4-1. This modification resulted into two basic optimization steps at each update interval t_ν:

- Systematic Grid Search

  All possible parameter combinations within a grid of specified limits and fineness are evaluated for J. This complete survey of parameter space largely reduces the risk of finding local rather than absolute minima.

- Gradient Search

  A powerful gradient minimization scheme based on the method of conjugate gradients uses the minimum of the grid search as starting point for a modern method of steepest descent to locate the minimum more precisely.

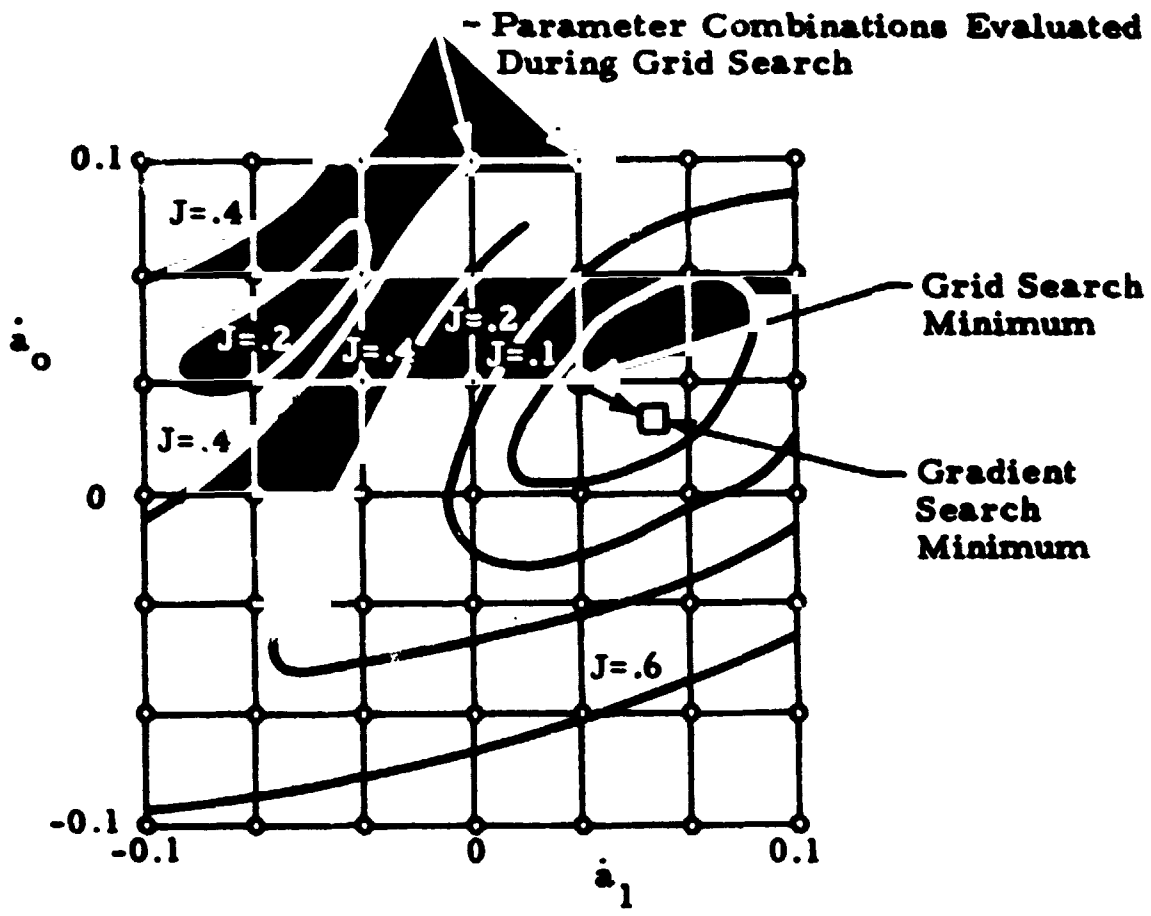

Fig. 2.4-1 - Parameter Optimization Performed in Two Phases: (1) Systematic Grid Search (o) for Complete Survey of Parameter Space; Grid Point of Minimum J (◉) Serves as Starting Point for (2) Gradient Search Which Locates the Mirimum More Precisely (□). From Grid Search Contour Plots (Lines of J = Const) can be Drawn for Better Insight into J-Topology.

The optimizer has been extensively modified under this contract and put into convenient modular form. As indicated in Fig. 2.1-1, both optimization steps need not be taken. Furthermore the feedback law includes constant gains as well as gains which are a function of time. In this way, the user is permitted the choice of selecting the accuracy of the minimization process and the type of feedback most appropriate for the incident problem.

2.5 REDUCING THE SENSITIVITY TO PARAMETER UNCERTAINITES

The hybrid optimizer has the capability to design a truly optimal system; that is, one which anticipates the occurrence of a number of possible conditions, tests performance against a criterion which is a function of these possible conditions, and adjusts the control parameters so as to optimize this performance criterion. For example, in the case of launch vehicle control systems, it might be desirable to minimize peak bending moments or to minimize control system weight related penalties, assuming the possible occurrence of a variety of different environmental or failure conditions.

This capability of "Parameter Uncertainty Desensitization" was easily added to the optimizer. Instead of considering only one operating condition, the optimizer was modified to consider two conditions which may be defined as the two most adverse operating conditions. At each grid point, both conditions are simulated, and the worst condition is chosen as the condition to be optimized. The gradient search performs in the same manner except when gradients are being computed. Experience had proven that no radical change in performance could be detected by the small perturbations of the controller gain slopes needed to compute gradients. This method of considering two adverse operating conditions can be readily expressed as solving a "minimax" problem; i.e., minimizing the maximum of several functions.

2.6 PERFORMANCE EVALUATION

The most practical feature of this hybrid optimizer is the ability to specify design goals in the most direct manner with virtually no mathematical constraints on its functional form. This high degree of flexibility in selecting performance criteria of arbitrary form was fully utilized by choosing a minimax criterion for initial shuttle ascent studies. The criterion selected for this study was that of weight. That is, for the ascent portion of the study orbit insertion weight was maximized and for reentry, control system related weight penalties were minimized. Aerodynamic control was optimized separately from control by means of engines. Both types of control were then blended as discussed in Section 3.2 for ascent and 4.2 for reentry.

Section 3
FORMULATION OF ASCENT STUDY

The ascent blending study was performed with the use of an existing hybrid simulation developed under another contract (NAS8-25578). Minor changes and additions were necessary to extend the capability of this simulation to include aerodynamic surface control.

3.1 VEHICLE EQUATIONS OF MOTION

A set of 6-DOF perturbation equations of motion describing the dynamics of a large shuttle ascent vehicle about a nominal zero-lift trajectory was derived in Ref. 2. All assumptions and approximations are given in this document. These equations are listed as follows with sign conventions and notations shown in Fig. 3.1-1.

Translations

$$\ddot{x} = -k_{\dot{\phi}}\dot{\theta} - k_3\alpha + k_{xc}\delta_c + k_{xe}\delta_e$$

$$\ddot{y} = k_{\dot{\phi}}\dot{\phi} + k_{\dot{\psi}}\dot{\psi} + k_1\delta_\psi + k_{y\beta}\beta + k_{ya}\delta_a + k_{yr}\delta_r + k_2\psi + k_3\phi$$

$$\ddot{z} = k_{\dot{\theta}}\dot{\theta} - k_1\delta_\theta + k_{z\alpha}\alpha + k_{ze}\delta_e + k_{zc}\delta_c$$

where

$$k_{\dot{\phi}} = \alpha_o U_o \qquad k_1 = -T/m$$

$$k_3 = g\sin\chi_\theta \qquad k_{y\beta} = \bar{q}SC_{y_\beta}/m \qquad k_\theta = U_o$$

$$k_{xc} = -\bar{q}S_c C_{A_{\delta_c}} \qquad k_{ya} = \bar{q}S_a C_{y_{\delta_a}}/m \qquad k_{z\alpha} = -\bar{q}SC_{N_\alpha}/m - g\cos\chi_\theta/57.3$$

$$k_{xe} = -\bar{q}S_e C_{A_{\delta_e}} \qquad k_{yr} = -\bar{q}S_r C_{y_{\delta_r}}/m \qquad k_{ze} = -\bar{q}S_e C_{N_{\delta_e}}/m$$

$$k_\psi = -U_o \qquad k_2 = g\cos\chi_\theta \qquad k_{zc} = -qS_c C_{N_{\delta_c}}/m$$

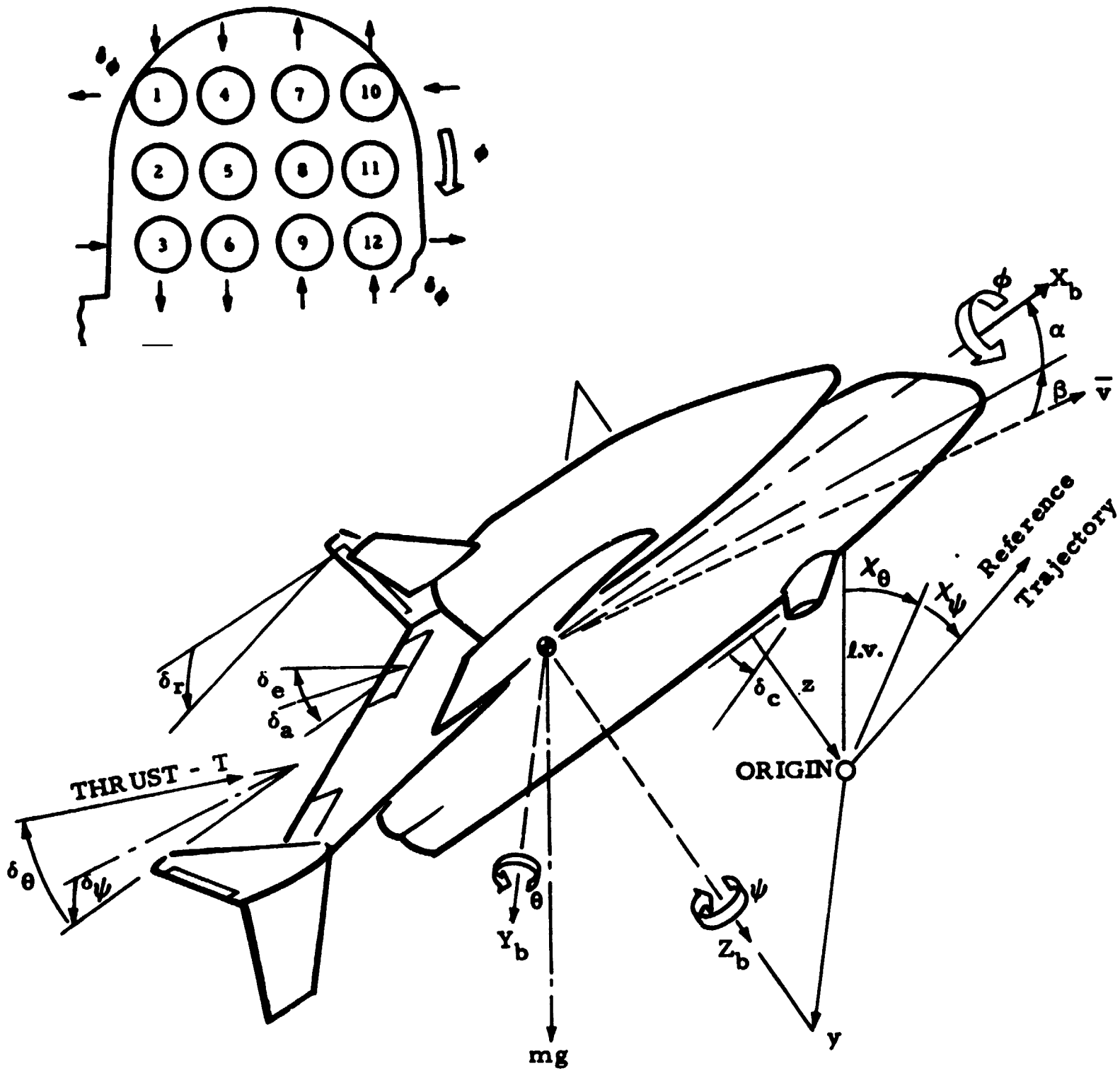

Fig. 3.1-1 - Sign Conventions and Notations for 6-Degree-of-Freedom Shuttle Ascent Perturbation Equations of Motion

Rotation

$$\ddot{\phi} = k_{\phi\psi}\ddot{\psi} + k_{\ell\theta}\delta_\theta + k_{\ell\psi}\delta_\psi + k_{\ell\phi}\delta_\phi + k_{\ell\dot{\phi}}\dot{\phi} + k_{\ell\dot{\psi}}\dot{\psi} + k_{\ell\beta}\beta + k_{\ell a}\delta_a + k_{\ell r}\delta_r$$

$$\theta = k_{m\alpha}\alpha + k_{m\theta}\delta_\theta + k_{m\dot{\theta}}\dot{\theta} + k_{me}\delta_e + k_{mc}\delta_c$$

$$\ddot{\psi} = k_{n\psi}\psi + k_{n\dot{\phi}}\dot{\phi} + k_{n\dot{\psi}}\dot{\psi} + k_{n\beta}\beta + k_{na}\delta_a + k_{nr}\delta_r$$

where

$$k_{\phi\psi} = I_{xz}/I_x$$

$$k_{\ell\theta} = -T(y_{cg} - \ell_y)/I_x$$

$$k_{\ell\psi} = -T(z_{cg} - \ell_z)/I_x$$

$$k_{\ell\phi} = T\ell_\phi/I_x$$

$$k_{\ell\dot{\phi}} = \frac{\bar{q}b^2 S C_{\ell p}}{2U_o I_x}$$

$$k_{\ell\dot{\psi}} = \frac{\bar{q}b^2 S(C_{\ell r} - C_{\ell\dot{\beta}})}{2U_o I_x}$$

$$k_{\ell\beta} = \frac{\bar{q}b S C_{\ell\beta}}{I_x}$$

$$k_{\ell_a} = \frac{\bar{q}b S_a C_{\ell_{\delta_a}}}{I_x}$$

$$k_{\ell_r} = \frac{-\bar{q}b S_r C_{\ell_{\delta_r}}}{I_x}$$

$$k_{m\alpha} = \frac{\bar{q}\bar{c}SC_{m\alpha}}{I_y}$$

$$k_{m\theta} = \frac{-T\ell_x}{I_y}$$

$$k_{m\theta} = \frac{\bar{q}\bar{c}^2 S(C_{m_q} + C_{m_{\dot{\alpha}}})}{2U_o I_y}$$

$$k_{me} = \frac{-q\bar{c}S_e C_{m_{\delta_e}}}{I_y}$$

$$k_{mc} = \frac{\bar{q}\bar{c}SC_{m_{\delta_c}}}{I_y}$$

$$k_{n\psi} = \frac{-T\ell_x}{I_z}$$

$$k_{n\phi} = \frac{\bar{q}b^2 S C_{n_p}}{2U_o I_z}$$

$$k_{n\psi} = \frac{\bar{q}b^2 S(C_{n_r} - C_{n_{\dot{\beta}}})}{2U_o I_z}$$

$$k_{n\beta} = \frac{-\bar{q}bSC_{n_\beta}}{I_z}$$

$$k_{n\alpha} = \frac{\bar{q}bS_a C_{N_{\delta_a}}}{I_z}$$

$$k_{nr} = \frac{\bar{q}bS_r C_{N_{\delta_r}}}{I_z}$$

3.2 CONTROL LAW AND BLENDING LOGIC

The control laws used in the ascent study are simple position plus rate feedback loops with an additional sideslip feedback term in the yaw channel. The initial approach to the blending of the aerodynamic surfaces was to establish adjustable ratios (k_c for canard control, k_e for elevon control, k_r for rudder control, and k_a for aileron control blending), which could be optimally adjusted to feed back the position/rate signals in parallel with the thrust vector control system. These control laws and blending logic are shown in Fig. 3.2-1 and are listed as follows:

$$\delta_\theta = -H_\theta(s)\left[a_{o\theta}\theta + a_{1\theta}\dot{\theta}\right]$$

$$\delta_\psi = -H_\psi(s)\left[a_{o\psi}\psi + a_{1\psi}\dot{\psi} - b_{o\psi}\beta\right]$$

$$\delta_\phi = -H_\phi(s)\left[a_{o\phi}\phi + a_{1\phi}\dot{\phi}\right]$$

$$\delta_c = -k_c H_c(s)\left[a_{o\theta}\theta + a_{1\theta}\dot{\theta}\right]$$

$$\delta_e = -k_e H_e(s)\left[a_{o\theta}\theta + a_1\dot{\theta}\right]$$

$$\delta_r = -k_r H_r(s)\left[\alpha_{o\psi}\psi + a_{1\psi}\dot{\psi} - b_{o\psi}\beta\right]$$

$$\delta_a = -k_a H_a(s)\left[a_{o\phi}\phi + a_{1\phi}\dot{\phi}\right]$$

where

$$H_\theta(s) = H_\psi(s) = H_\phi(s) = \frac{15}{S+15}$$

$$H_c(s) = H_e(s) = H_r(s) = H_a(s) = \frac{3}{S+3}$$

k_c, k_e, k_r, k_a = blending ratios

Refer to Fig. 3.2-1.

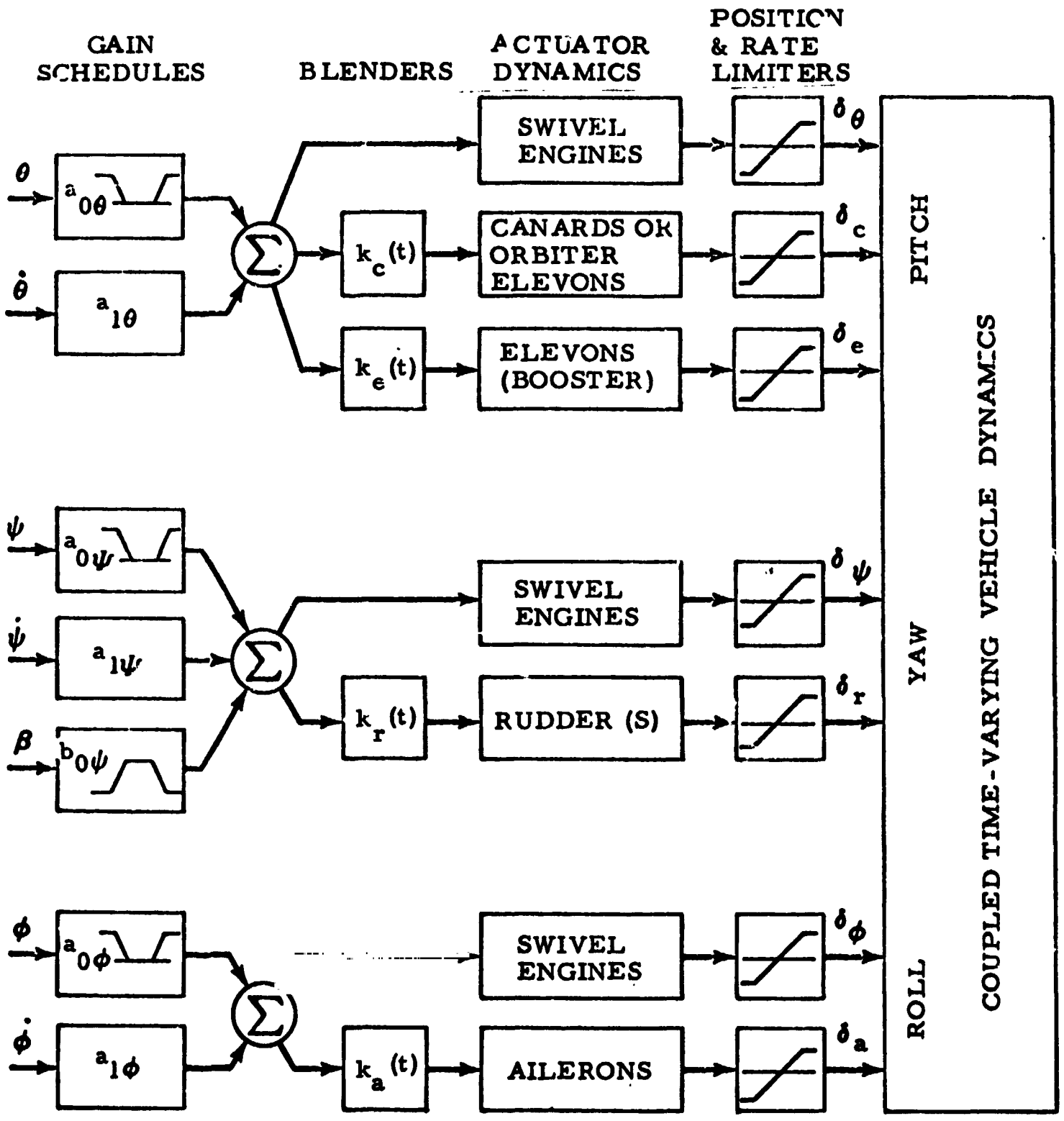

Fig. 3.2-1 - General Structure of Ascent Control System with Four Independent Blending Schedules for Canard, Elevon, Rudder and Aileron Blending

3.3 ASCENT CONTROL RELATED PENALTIES AND SENSITIVITY ANALYSIS

The overriding design criterion in all booster control problems should be to stabilize the vehicle while the orbital insertion weight is maximized. Such a payload maximization criterion combines all the standard design criteria (load relief, minimum drift, etc.) in the most meaningful manner and provides the key to a computerized optimal design approach. Since there are virtually no constraints imposed on the mathematical form of the performance criterion in Lockheed's Direct Optimization approach other than positive definiteness, the following performance index was formulated which comprises the major ascent control system related payload penalties which should be minimized for optimum performance:

$$J' = \sum_{i=1}^{6} \frac{\partial P}{\partial R_i} \left| R_{i_{max}} - R_{i_o} \right| + \sum_{j=1}^{3} \frac{\partial P}{\partial \delta_j} \left| \delta_{j_{max}} - \delta_{j_o} \right|$$

$$+ \sum_{m=1}^{3} \left[\frac{\partial P}{\partial x_m} x_{m_{max}} + \frac{\partial P}{\partial v_m} v_{m_{max}} \right]$$

$$+ \frac{\partial P}{\partial H_M} \left| H_{M_{max}} \right| \longrightarrow \text{MIN}$$

where

P = payload penalty or decrease

R_i = forces at the booster-orbiter interface

δ_i = main booster engine gimbal angles for roll, pitch, yaw control including δ_{trim}

x_m = deviations from reference trajectory in x, y, z direction

v_m = velocity errors with respect to reference trajectory in x, y, z direction

H_M = hinge moment due to aerodynamic surface deflection

The subscript "o" denotes design values corresponding to the nominal payload capability.

The design goal of maximum payload can then be achieved by minimization of this payload penalty functional J'.

In order to avoid excessive angular rates by the vehicle in response to gust-type wind disturbances, an additional cost functional was formulated:

$$J'' = \frac{1}{T}\int_{t}^{t+T}\left[\left|\frac{\dot{\phi}}{\dot{\phi}_{ME}}\right| + q_{\dot{\theta}}\left|\frac{\dot{\theta}}{\dot{\theta}_{ME}}\right| + q_{\dot{\psi}}\left|\frac{\dot{\psi}}{\dot{\psi}_{ME}}\right|\right]dt$$

where $\dot{\phi}$, $\dot{\theta}$, $\dot{\psi}$, are the roll, pitch, and yaw rates, respectively, and the subscript "ME" denotes maximum expected values. $q_{\dot{\theta}}$ and $q_{\dot{\psi}}$ are weighting coefficients reflecting the design constraints imposed on the various vehicle rates. J'' should be kept small to assure smooth flying qualities. The criteria (J) and (J'') can be readily combined into a single performance criterion

$$J = J' + q\,J'' \longrightarrow \min.$$

which makes possible the minimization of all payload penalties while a weighted flying quality criterion qJ'' is simultaneously satisfied.

Engineering experience had shown that the major insertion weight penalty contribution would be the booster dry weight which is dependent upon the

structural loads encountered during powered ascent. The interface loads transmitted through the attachment points between booster and orbiter were identified as having a strong impact on the booster fuselage weight. It was therefore necessary for the equations of motion describing these interface loads to be derived and extended to the hybrid simulation studies to allow for continuous computation of these loads for vehicle performance evaluation. The general approach to the development of these interface equations are given in the following paragraphs. A more detailed derivation is included in Ref. 2.

The structural design of the supports between booster and orbiter depend on the maximum interface loading on each of the supports during the entire ascent phase of the flight. Knowing the motion of the composite vehicle ($\vec{U}, \vec{\Omega}$) from the 6-D ascent simulation for the nominal trajectory, the nominal interface forces and moments can be determined as part of the external forces acting on the orbiter only (subscript o) which lead to the orbiter's known motion $\vec{U}_o$, $\vec{\Omega}_o$:

$$(\vec{F})_I = (M)_o \left[\dot{\vec{U}} + \vec{\Omega} \times \vec{U}\right] - (\vec{F}_{aero})_o - (\vec{F}_{cg\ offset})_o - (\vec{W})_o$$

$$(\vec{M})_I = \left[I_o\right] \dot{\vec{\Omega}} + \vec{\Omega} \times \left[I_o\right] \vec{\Omega} - (\vec{M}_{aero})_o$$

For the actual trajectory (i.e., perturbed trajectory), the perturbed interface forces and moments are given by

$$(\vec{f})_I = (M)_o \left[\dot{\vec{u}} + \vec{\Omega} \times \vec{u} + \vec{\omega} \times \vec{U}\right] - (f_{aero})_o - (f_{cg\ offset})_o - (\vec{w})_o$$

$$(\vec{m})_I = \left[I_o\right] \dot{\vec{\omega}} + \vec{\omega} \times \left[I_o\right] \vec{\Omega} + \vec{\Omega} \times \left[I_o\right] \vec{\omega} - (\vec{m}_{aero})_o$$

where capital letters and lower case letters indicate nominal and perturbed values, respectively, and $\vec{F}_I$ and $\vec{M}_I$ are interface forces and moments. $(F_{aero})_o$ and $(M_{aero})_o$ are the aerodynamic forces and moments acting on the

orbiter alone. $(\vec{F}_{cg\ offset})_o$ is the centrifugal force due to offset of orbiter cg from that of the composite vehicle, and $(\vec{W})_o$ is the weight of the orbiter. The nominal interface forces and moments will be determined by the 6-D Shuttle Data program, whereas the perturbed forces and moments can be obtained from the analog simulation. The force components acting on each support, as shown in Fig. 3.3-1, can be determined by:

$$\vec{R} = [A]\ (\overrightarrow{FM})_I + [A]\ (\overrightarrow{fm})_I$$

where

$\vec{R} = (R_{1x}, R_{1y}, R_{1z}, R_{2z}, R_{3z}, R_{4z})$ are force components acting on the supports

$[A]$ is a 6x6 matrix, where elements are functions of $\ell_1, \ell_2, \ell_3, \ell_4$

$\overrightarrow{FM} = ((\vec{F})_I, (\vec{M})_I)$

$\overrightarrow{fm} = ((\vec{f})_I, (\vec{m})_I)$

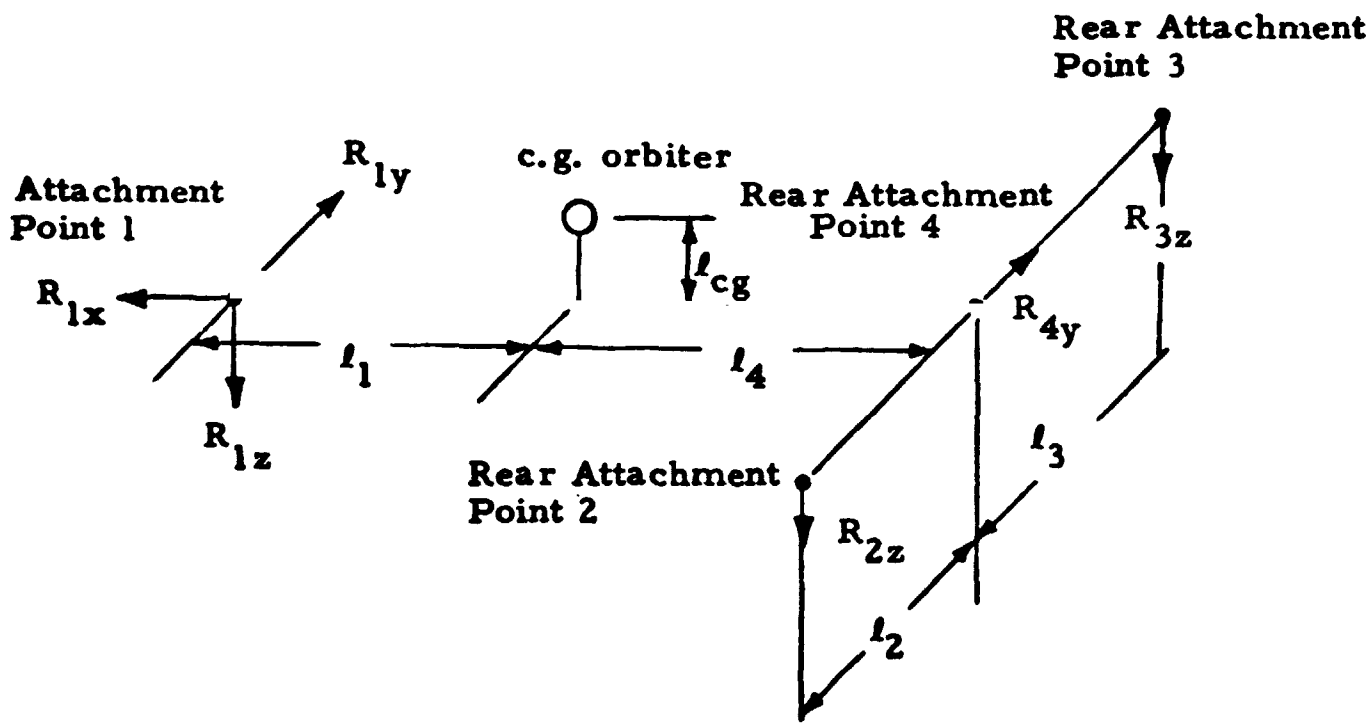

Fig. 3.3-1 - Components of Interface Load at the Attachment Points of Shuttle Booster and Orbiter (MDAC-20 Configuration)

This derivation yields the total interface force at each station as listed as follows.

$$R_{1x} = f_{x1} + F_{x1}$$

$$R_{1z} = g_1(f_{z1} + F_{z1}) + g_2 R_{1x} + g_3(\hat{m}_1 + M_1)$$

$$R_{1y} = g_4(\hat{n}_1) + g_5(f_{y1})$$

$$R_{4y} = f_{y1} - R_{1y}$$

$$R_{2z} = g_6 \hat{f}_1 + g_7 f_{y1} + g_8(f_{z1} + F_{z1}) + g_9 R_{1z}$$

$$R_{3z} = f_{z1} + F_{z1} - R_{1z} - R_{2z}$$

where

$g_1 = \ell_4/(\ell_1 + \ell_4)$

$g_2 = \ell_{cg}/(\ell_1 + \ell_4)$

$g_3 = -1/(\ell_1 + \ell_4)$

$g_4 = 1/(\ell_1 + \ell_4)$

$g_5 = \ell_4/(\ell_1 + \ell_4)$

$g_6 = -1/2\ell_2$

$g_7 = -\ell_{cg}/2\ell_2$

$g_8 = 1/2$

$g_9 = -1/2$

(lower case f_{x1}, f_{y1}, ..., $\hat{m}_1$ indicate perturbation interface forces and moments acting on body 1 (orbiter))

F_{x1} = nominal interface force along x-axis on body 1 (orbiter) due to trajectory and vehicle configuration

F_{z1} = nominal interface force along z-axis on body 1 (orbiter) due to trajectory and vehicle configuration

M_1 = nominal interface moment along y-axis on body 1 (orbiter) due to trajectory and vehicle configuration

3.3.1 Structural Weight

This section deals with methods of obtaining the orbit insertion weight partials for implementation into the performance index function to realize maximum orbital payload. A structural analysis of the booster fuselage in the region of the orbiter attachment points revealed that the peak interface forces R_{2z}, R_{3z}, R_{4y} strongly affect the booster hydrogen tank design shown in Fig. 3.3-2. The hydrogen tank is compression-critical rather than pressure critical. The stress resultant N_x in the axial direction determines the design. In a first approximation, no circumferential variation was considered and N_x was determined by summing the effects of axial compression and bending from a one-dimensional internal load analysis. Given the maximum compressive loads, the stiffeners of each barrel can be designed by using the formulation given in Ref. 3. Three failure modes are considered: general instability, skin buckling, and web crippling. Their simultaneous occurrence determines the design point; i.e., the dimensions w, b, and t_s on Fig. 3.3-2. Then a weight thickness $\bar{t}$ can be computed.

To find the variation of the tank weight with aft interface loads, the following procedure is followed:

1. For each flight condition of interest, the interface loads and the complete set of maximum axial compressive stress resultants N_x is computed.
2. The weight thickness of each barrel is determined.
3. The total tank weight is computed.

For the first step the internal shears and moments resulting from the external forces and moments must be determined. The external forces considered are distributed aerodynamic effects obtained from model measurements, inertia effects computed from the simulated accelerations and given mass

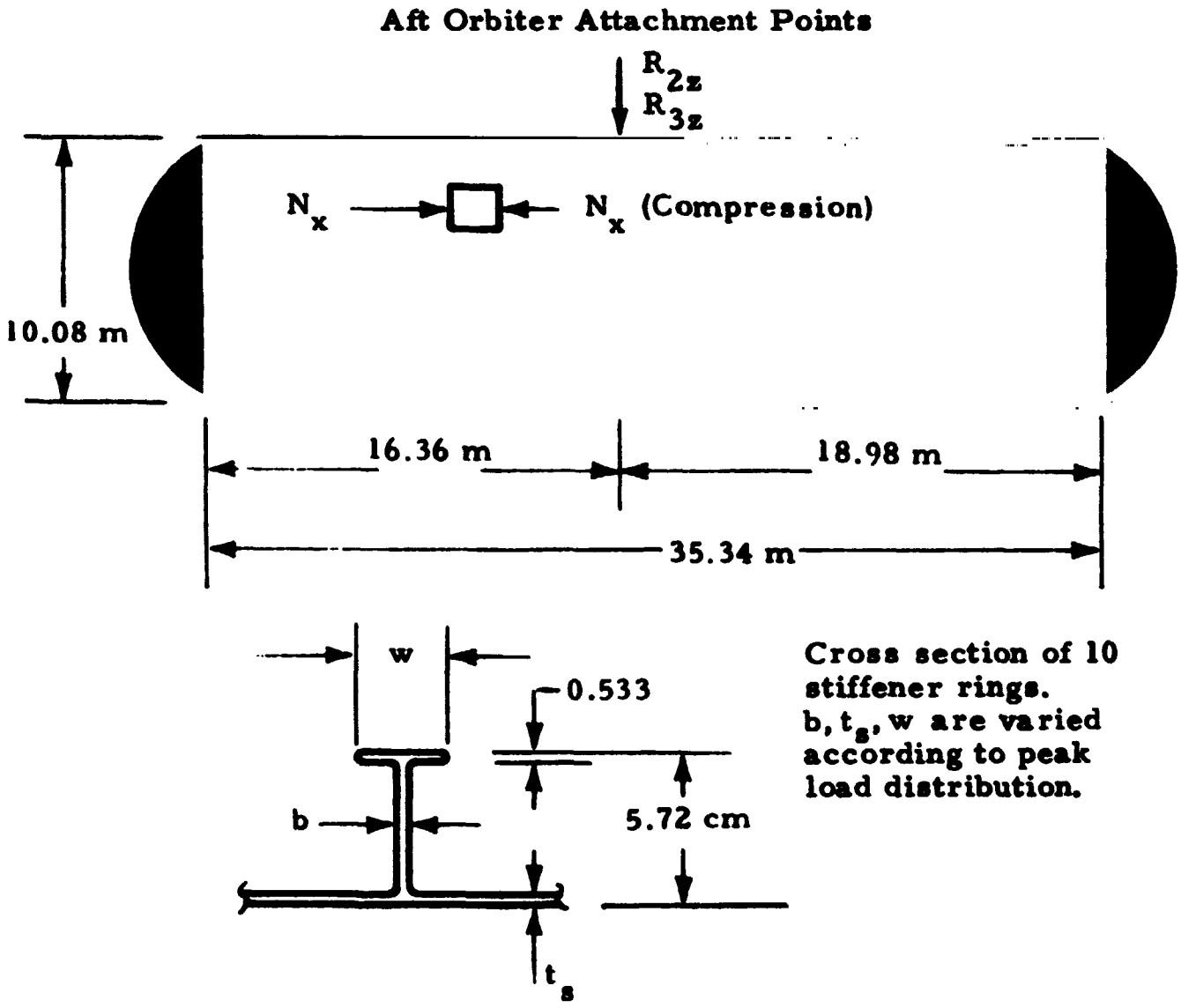

Fig. 3.3-2 - Booster Hydrogen Tank Stiffener Geometry

distribution. In order to account for general unsymmetrical loads, the total force at the three rear attachment points 2, 3, and 4 must be computed.

$$R_r = \sqrt{(R_{2z} + R_{3z})^2 + R_{4y}^2}$$

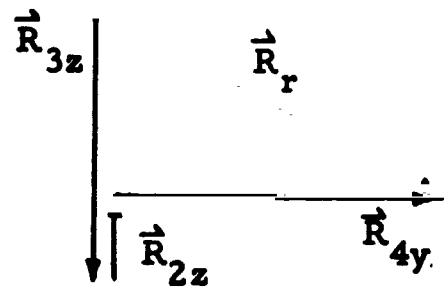

Peak values of R_r can then be used to determine the booster's H_2-tank weight. Th mass sensitivity of the booster H_2-tank for changes in interface load R_r is then found to be

$$\frac{\Delta W_{H_2\,Tank}}{\Delta R_r} = 0.0104 \text{ Kg/N},$$

which can be expressed in a payload penalty ΔP according to Ref.

$$\frac{\partial P}{\partial R_r} \approx \frac{\Delta P}{\Delta R_r} = \frac{\Delta W_{H_2\,Tank}}{\Delta R_r} \frac{\Delta P}{\Delta W_{Booster}} = 0.0104 * 0.2$$

$$= 0.00208 \frac{Kg}{N}$$

Since the tank center of gravity is only 0.6 m from the booster center of gravity upon burnout, no additional penalty due to hypersonic trim requirements is necessary.

3.3.2 Engine Gimbal Angle

The major effects of maximum engine gimbal angles on space shuttle payload were determined in a recent study. An increase in engine deflection δ requires a heavier actuator system, larger engine base area with associated increase in drag, structural weight and fuel requirement.

Typical values for the payload penalty $\partial P/\partial \delta$ were found to be of the order

$$\frac{\partial P}{\partial \delta} = 221 \frac{Kg}{deg}$$

This value was also used in the present study for all total gimbal angles $\delta_{Trim} + \delta$ which exceed the nominal design values. Trim gimbal angles for the zero-lift trajectory used in the study (provided by MSFC, Aero-Astrodynamics Laboratory, S&E-AERO-GT) are shown in Fig. 3.3-3.

3.3.3 Impact of Trajectory Deviations on Payload

Vehicle insertion weight variations from nominal, produced by vehicle state perturbations existing at the start of active closed-loop guidance, were assumed to be at $t_g = 100$ sec into ascent when atmospheric disturbances have virtually died out. These trajectory related penalty functions were computed using a trajectory computation program incorporating a quasi-optimal guidance concept. Insertion weight deviations were computed for each parameter of the vehicle state taken singly. The insertion weight was initially expressed by a quadratic function of the form

$$\Delta W_{ins} = \sum_{m=1}^{3} \left[\frac{\partial W}{\partial x_m} x_m(t_g) + \frac{\partial W}{\partial v_m} v_m(t_g) + \frac{\partial W}{\partial x_m^2} x_m^2(t_g) + \frac{\partial W}{\partial v_m^2} v_m^2(t_g) \right] .$$

Coupling terms had earlier been found to be not significant for this particular reference zero lift trajectory provided by MSFC's Flight Mechanics Branch and were therefore neglected together with the quadratic terms which were two or more orders of magnitude smaller than the linear terms. The following payload penalty coefficients were calculated in second stage burn time and converted to payload penalty for use in the performance criterion.

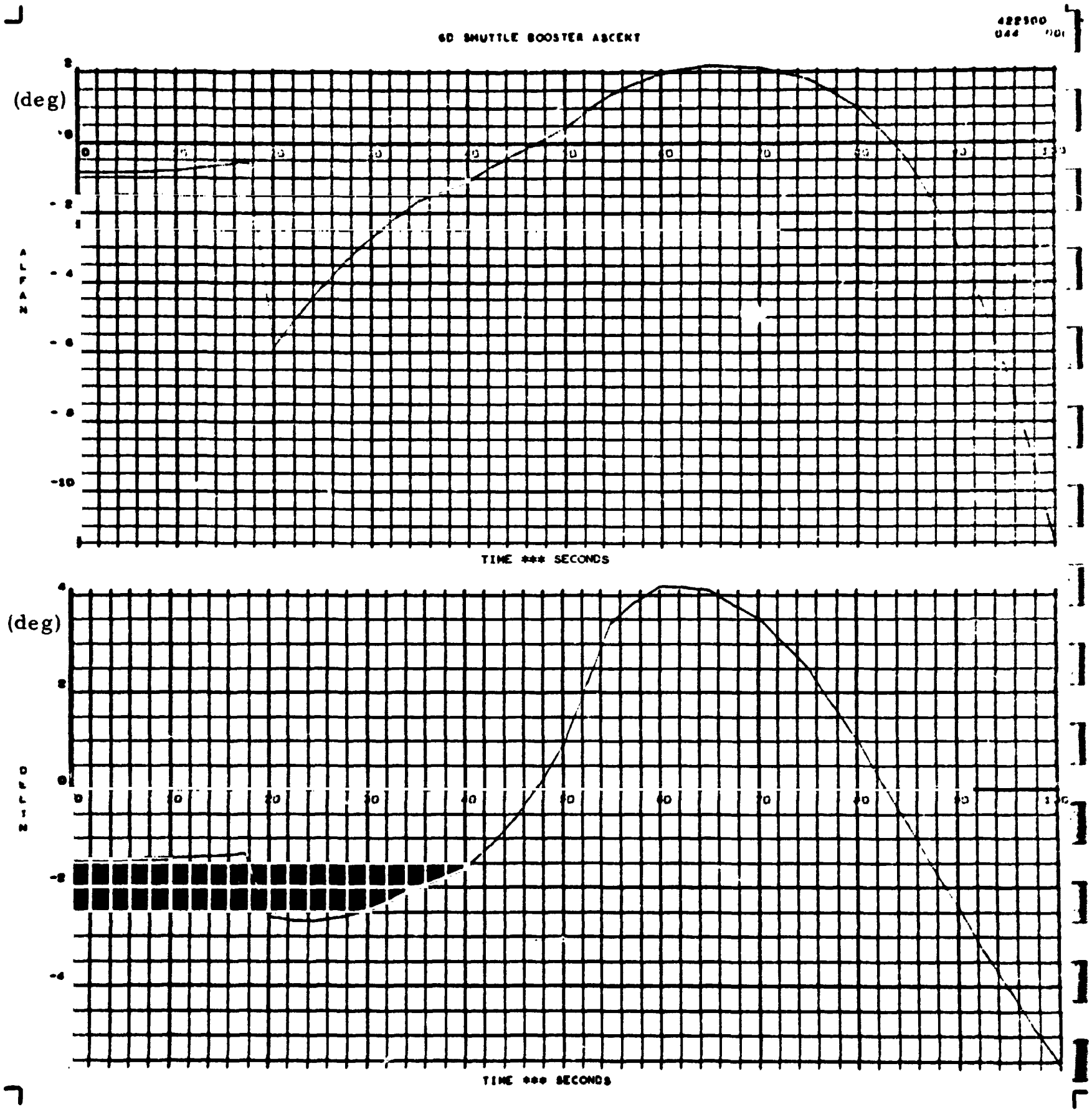

Fig. 3.3-3 - Trim Gimbal Angle $\delta\theta_o$ and Angle of Attack α_o Computed by Simultaneous Solution of Trim EOM from Zero-Lift Trajectory Data Provided by MSFC, Aero-Astrodynamics Laboratory, for MDAC Configuration 20

$$\frac{\partial P}{x(100\ \text{sec})} = -0.061\ \frac{\text{kg}}{\text{m}}\ ; \qquad \frac{\partial P}{|y(100\ \text{sec})|} = 0.027\ \frac{\text{kg}}{\text{m}}\ ;$$

$$\frac{\partial P}{z(100\ \text{sec})} = 0.035\ \frac{\text{kg}}{\text{m}}\ ; \qquad \frac{\partial P}{\dot{x}(100\ \text{sec})} = -6.8\ \frac{\text{kg}}{\text{m/sec}}\ ;$$

$$\frac{\partial P}{|\dot{y}(100\ \text{sec})|} = 0.43\ \frac{\text{kg}}{\text{m/sec}}\ ; \qquad \frac{\partial P}{\dot{z}(100\ \text{sec})} = 4.0\ \frac{\text{kg}}{\text{m/sec}}$$

Section 4
FORMULATION OF REENTRY STUDY

4.1 VEHICLE EQUATIONS OF MOTION

The motion of a booster or an orbiter in reentry flight is determined by the propulsive forces supplied by the auxiliary propulsion system, the force of gravity, the inertial characteristics of vehicle and the aerodynamic forces. To derive the equations of the motion of the vehicle, it is necessary to equate forces and moments acting on the vehicle to the vehicle reactions, according to Newton's law. The theory of small perturbations is introduced into the derivation to arrive at linear equations about a reference trajectory. The controls considered are elevon, ailerons, rudder, and auxiliary control propulsion system.

The mathematical model, which is used to derive the perturbation equations of motion for shuttle reentry studies, is formulated with the following basic assumptions and approximations.

1. The vehicle is a rigid body airframe with negligible variation in mass during the reentry phase of the flight.
2. The vehicle is symmetric with respect to the x_b-z_b plane in the body axis system.
3. Disturbances from the reference flight condition are small.
4. The disturbance in flight path velocity is negligibly small.
5. The reference flight condition has a negligibly small sideslip angle.

The form of six-degree-of-freedom (three translational, three rotational) equations of motion of a reentry vehicle such as a booster or an orbiter flying in the atmosphere is rigidly prescribed. However, there is freedom to select axis systems and variables. The efficient use of analog computer requires that care be exercised in selecting computer variables, since the accuracy of the result is greatly affected by scaling. The best choice of axis systems

in which to write the equation depends on the predominant effect of the aerodynamic forces and moments. The use of flight-path axes (often called wind axes) as opposed to body axes for solving the translational equations can be shown to make much lower demands on computer accuracy and bandwidth.

Figure 4.1-1 shows the interrelationships of the various axis systems. The body axes, x_b, y_b and z_b, are a right-hand orthogonal set rigidly attached to the airframe. The stability axes x_s, y_s and z_s differ from the body axes only by the angle of attack α. Aerodynamic force and moment data are often presented in terms of components along stability axes. The flight-path axes, x_w, y_w and z_w, differ from the stability axes by the angle of sideslip β. The x_w wind axis is aligned, by definition, in the direction of flight.

By using the flight-path axes to write the translational equations of motion, $\hat{V}$, $\hat{\alpha}$, and $\hat{\beta}$ become the velocity state variables, all of which are directly needed for aerodynamic claculations. Let the external force components along the wind axes be denoted by the symbols $\hat{F}_{xw}$, $\hat{F}_{yw}$, and $\hat{F}_{zw}$. These forces generally include contributions from gravity, propulsive and aerodynamic forces. If the action and reaction forces are summed along each wind axes, the following three equations can be obtained:

$$\dot{\hat{V}} = \hat{F}_{xw}/m \tag{4.1-1}$$

$$\dot{\hat{\beta}} = -(\hat{R}\cos\hat{\alpha} - \hat{P}\sin\hat{\alpha}) + \hat{F}_{yw}/m\hat{V} \tag{4.1-2}$$

$$\dot{\hat{\alpha}}\cos\beta = \hat{Q}\cos\beta - (\hat{R}\sin\hat{\alpha} + \hat{P}\cos\hat{\alpha})\sin\beta + \hat{F}_{zw}/m\hat{V} \tag{4.1-3}$$

where m is the mass of the vehicle. Equation (4.1-1) simply states that the product of the mass and the time rate of change of the total vehicle velocity is equal to the force along the flight path direction. Equation (4.1-2) states that $\dot{\beta}$, the time rate of change of sideslip angle, is equal to flight-path yaw rate, $\hat{F}_{yw}/m\hat{V}$, minus the body axis angular rate along z_w. Finally, for $\hat{\beta}$ equal to zero, Eq. (4.1-3) states that $\dot{\hat{\alpha}}$, the time rate of change of angle of attack, is equal to the body axis pitch rate $\hat{Q}$, minus the flight-path axis pitch rate, $-\hat{F}_{zw}/m\hat{V}$.

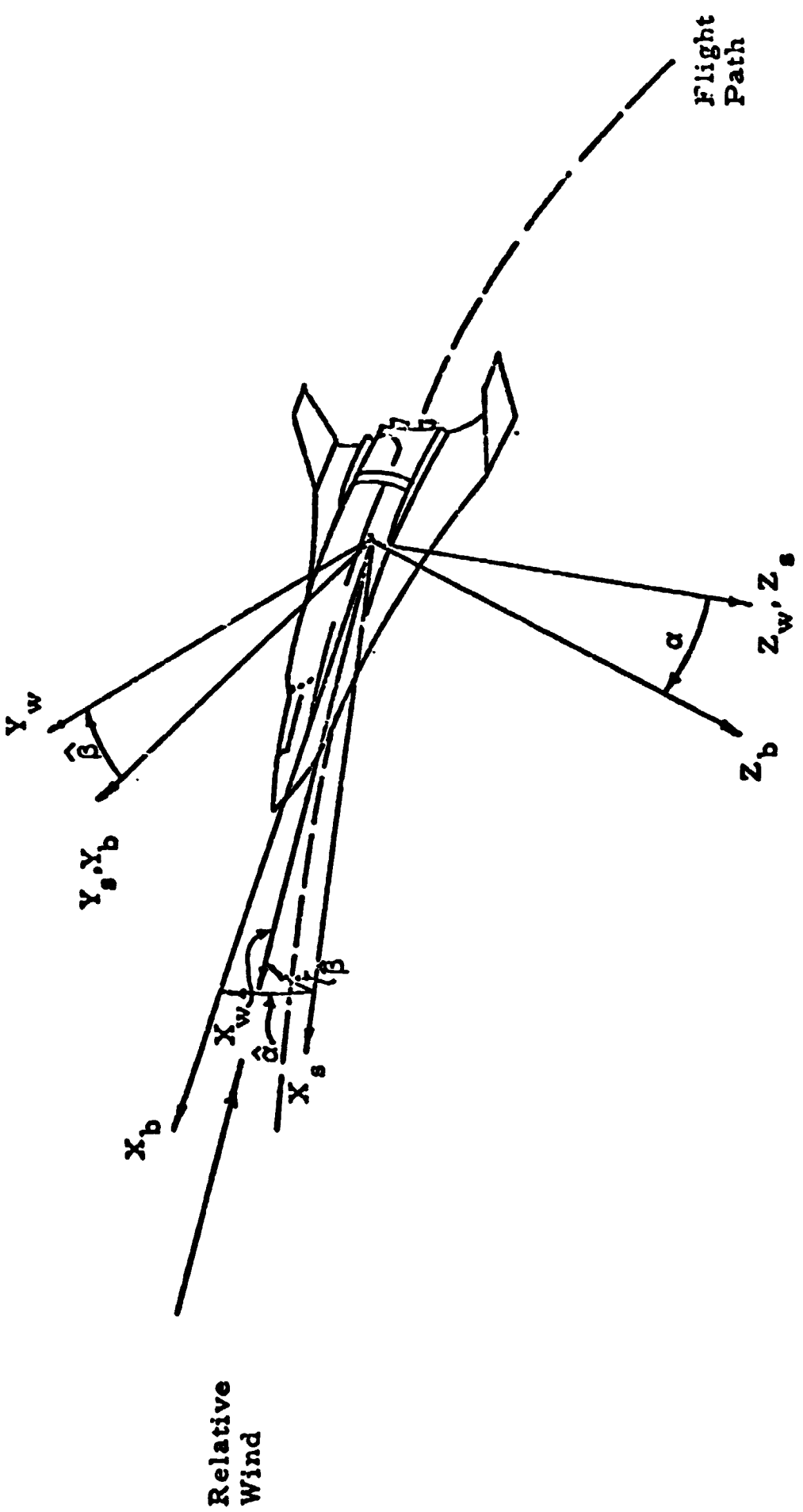

Fig. 4.1-1 - Coordinate Systems

The rotational equations of motion for vehicles symmetric with respect to X_b-Z_b plane, and with constant moment and produce moment of inertia can be written in the body axis system as

$$\dot{\hat{P}} = \left[\frac{I_z(I_y - I_z) - I_{xz}^2}{I_x I_z - I_{xz}^2}\right]\hat{Q}\,\hat{R} + \left[\frac{I_{xz}(I_x - I_y - I_z)}{I_x I_z - I_{xz}^2}\right]\hat{P}\,\hat{Q} + \left[\frac{I_z \hat{L} + I_{xz}\hat{N}}{I_x I_z - I_{xz}^2}\right] \quad (4.1\text{-}4)$$

$$\dot{\hat{Q}} = \left[\frac{I_z - I_x}{I_y}\right]\hat{P}\,\hat{R} + \left[\frac{I_{xz}}{I_y}\right](\hat{R}^2 - \hat{P}^2) + \left[\frac{M}{I_y}\right] \quad (4.1\text{-}5)$$

$$\dot{\hat{R}} = \left[\frac{I_x(I_x - I_y) + I_{xz}^2}{I_x I_z - I_{xz}^2}\right]\hat{P}\,\hat{Q} + \left[\frac{I_{xz}(-I_x + I_y - I_z)}{I_x I_z - I_{xz}^2}\right]\hat{Q}\,\hat{R} + \left[\frac{I_{xz}\hat{L} + I_x\hat{N}}{I_x I_z - I_{xz}^2}\right] \quad (4.1\text{-}6)$$

where I_x, I_y and I_z are the moments of inertial about X_b, Y_b and Z_b axis, respectively, and I_{xz} is the product moment of inertia; $\hat{L}$, $\hat{M}$ and $\hat{N}$ are the X_b, Y_b and Z_b components of external moment acting on the vehicle.

Equations (4.1-1) through (4.1-6) are nonlinear since they contain products of the dependent variables and also because the dependent variables appear as transcendential functions. For the purpose of stability and control analysis, these nonlinear equations are frequently linearized by assuming that the motion of the reentry vehicle can be written as the sum of the state variable component during the reference flight condition and a change in state variable component caused by disturbance.

$$\hat{V} = V_o + v, \quad \hat{\alpha} = \alpha_o + \alpha, \quad \hat{\beta} = \beta_o + \beta, \quad \hat{P} = P_o + p, \quad \hat{Q} = Q_o + q, \quad \hat{R} = R_o + r$$

$$\hat{F}_{xw} = F_{xwo} + f_{xw}, \quad \hat{F}_{yw} = F_{ywo} + f_{yw}, \quad \hat{F}_{zw} = F_{zwo} + f_{xw};$$

$$\hat{L} = L_o + M_x, \qquad \hat{M} = M_o + M_y, \qquad \hat{N} = N_o + M_z$$

The zero subscripts indicate the reference flight conditions, and the lower case arabic and Greek letters represent the changes in the state variables caused by disturbance. f_{xw}, f_{yw} and f_{zw} represent perturbation forces along the wind axes, whereas M_x, M_y, M_z represent the perturbation moments along the body axes. All the disturbance quantities and their derivatives are assumed to be small so that their squares and products are negligible compared to first-order quantities. If only the first-order terms in disturbance quantities are kept, then a set of linear equations can be obtained. The resulting translational perturbation equations of motion can be expressed as

$$\dot{v} = f_{xw}/m \tag{4.1-7}$$

$$\dot{\beta} = \left[P_o \cos\alpha_o + R_o \sin\alpha_o\right]\alpha + \left[\sin\alpha_o\right]p + \left[-\cos\alpha_o\right]r + \left[\frac{1}{mV_o}\right]f_{yw} + \left[-\frac{F_{ywo}}{mV_o^2}\right]v \tag{4.1-8}$$

$$\alpha = \left[-(P_o \cos\alpha_o + R_o \sin\alpha_o)\frac{1}{\cos^2\beta_o}\right]\beta + \left[-(-P_o \sin\alpha_o + R_o \cos\alpha_o)\tan\beta_o\right]\alpha + q + \left[-\cos\alpha_o \tan\beta_o\right]p + \left[-\sin\alpha_o \tan\beta_o\right]r + \left[\frac{F_{zw}\tan\beta_o}{mV_o\cos\beta_o}\right]\beta + \left[\frac{1}{mV_o\cos\beta_o}\right]f_{zw} + \left[-\frac{F_{zw}}{mV_o^2\cos\beta_o}\right]V \tag{4.1-9}$$

In most flight conditions, it can be assumed that $\beta_o = 0$, $v = 0$, then the above equations are reduced to:

$$f_{xw} = 0 \tag{4.1-10}$$

$$\dot{\beta} = \left[P_o \cos\alpha_o + R_o \sin\alpha_o\right]\alpha + \left[\sin\alpha_o\right]p + \left[-\cos\alpha_o\right]r + \left[\frac{1}{mV_o}\right]f_{yw} \tag{4.1-11}$$

$$\dot{\alpha} = \left[-(P_o \cos\alpha_o + R_o \sin\alpha_o)\right]\beta + q + \left[\frac{}{mV_o}\right]f_{zw} \tag{4.1-12}$$

The resulting rotational perturbation equations of motion can be written as

$$\dot{p} = \left[\frac{I_{xz}(I_x - I_y - I_z)}{I_x I_z - I_{xz}^2} Q_o\right]p + \left[\frac{I_{xz}(I_x - I_y + I_z)P_o + (I_z(I_y - I_z) - I_{xz}^2)R_o}{I_x I_z - I_{xz}^2}\right]q$$

$$+ \left[\frac{(I_z(I_y - I_z) - I_{xz}^2)Q_o}{I_x I_z - I_{xz}^2}\right]r + \frac{I_z M_x + I_{xz} M_z}{I_x I_z - I_{xz}^2} \tag{4.1-13}$$

$$\dot{q} = \left[\frac{(I_z - I_x)R_o - 2I_{xz}P_o}{I_y}\right]p + \left[\frac{(I_z - I_x)P_o + 2I_{xz}R_o}{I_y}\right]r + \frac{M_y}{I_y} \tag{4.1-14}$$

$$\dot{r} = \left[\frac{(I_x(I_x - I_y) + I_{xz}^2)Q_o}{I_x I_z - I_{xz}^2}\right]p + \left[\frac{(I_x(I_x - I_y) + I_{xz}^2)P_o + I_{xz}(-I_x + I_y - I_z)R_o}{I_x I_z - I_{xz}^2}\right]q$$

$$+ \left[\frac{I_{xz}(-I_x + I_y - I_z)Q_o}{I_x I_z - I_{xz}^2}\right]r + \frac{I_{xz} M_x + I_x M_z}{I_x I_z - I_{xz}^2} \tag{4.1-15}$$

The perturbation forces and moments can be expressed in any convenient coordinate system, then resolve into appropriate components in the wind axes and body axes, respectively. The perturbation equations of motion used in this study can be written as:

$$\dot{\alpha} = K_1\beta + K_2\alpha + K_3 q + K_4\phi + K_5\delta_e + K_6 f_{x(p)} + K_7 f_{z(p)} \quad (4.1\text{-}16)$$

$$\dot{\beta} = K_8\beta + K_9\alpha + K_{10}p + K_{11}q + K_{12}r + K_{13}\phi + K_{14}\delta_a + K_{15}\delta_e + K_{16}\delta_r + K_{17}f_{x(p)} + K_{18}f_{y(p)} + K_{19}f_{z(p)} \quad (4.1\text{-}17)$$

$$\dot{p} = K_{20}\beta + K_{21}\dot{\beta} + K_{22}\delta_a + K_{23}\delta_r + K_{24}p + K_{25}q + K_{26}r + K_{27}M_{x(p)} + K_{28}M_{z(p)} \quad (4.1\text{-}18)$$

$$\dot{q} = K_{29}\alpha + K_{30}\dot{\alpha} + K_{31}\delta_e + K_{32}q + K_{33}p + K_{34}r + K_{35}M_{y(p)} \quad (4.1\text{-}19)$$

$$\dot{r} = K_{36}\beta + K_{37}\dot{\beta} + K_{38}\delta_a + K_{39}\delta_r + K_{40}p + K_{41}q + K_{42}r + K_{28}M_{x(p)} + K_{43}M_{z(p)} \quad (4.1\text{-}20)$$

where K_i is time-varying coefficient. The detail derivation of shuttle reentry perturbation equations of motion and the detail expressions for K_i are given in Appendix A. These time-varying coefficients are computed by the digital computer program "DATA PREPROCESSOR" from the given raw trajectory, vehicle configuration and environment data. Some plots for input data and a complete set of the plots for output time-varying coefficients are given in Appendix C for the GDC-B-9U reentry vehicle.

For the purpose of verification, the above set of perturbation equations of motion is reduced to the conventional aircraft perturbation equations of motion and is given in Appendix B.

4.2 CONTROL AND BLENDING LAW SELECTION

One of the most challenging of reentry study problems is the determination of a control law for reentry shuttle vehicles. The problem is particularly difficult because of the tremendous range of many of the variables, such as flight velocity and because of the violent maneuvers. These are the results of the fact that the flight environment changes from a very high altitude to sea level conditions. The shuttle vehicle requires both an aerodynamic surface controller, as well as an auxiliary propulsion system (APS) for reentry control and guidance. The effectiveness of each system varies with the environment and the vehicle dynamic state. In general, an APS is the only effective controller for the initial phase of reentry. As the dynamic pressure increases, the aerodynamic surface controller becomes more effective. However, all three aerodynamic controllers (elevon, rudder and aileron) may not become effective simultaneously because of the vehicle configuration and vehicle attitude. These additional characteristics add complexity but offer tradeoff solutions for blending the two systems in an optimal manner.

The problems associated with stability and controlability of a shuttle are considerably different from that of an airplane. The reasons for this are mainly as follows:

1. The dynamic reaction varies drastically during the entire shuttle reentry phase of flight but is fairly constant for an airplane in flight.

2. Shuttle reentry flight covers hypersonic, supersonic and transonic phases of flight in a very short time. This is in contrast to the airplane in flight which covers a relatively narrow range of Mach number.

3. The angle of attack for the shuttle reentry flight is very large for a major portion of reentry flight and changes fairly rapidly.

The effort that is devoted in this study to ensuring that a finished shuttle will have adequate reentry flying qualities is made in the direction of mathematical analysis and hybrid computation. They are directed at setting up and

solving the complex equations which describe the behavior of a shuttle in reentry flight. The analysis of the disturbed motion of shuttle reentry rests upon the general perturbation equations of motion of the shuttle and its control system.

The perturbation equations of motion of the shuttle are given in Appendix A. The reentry control system controls angle of attack and bank angle in response to guidance commands occurring during various reentry phases. The APS utilizes thrusters, which are hard mounted to the airframe, to generate control moments. The basic feedback control laws used in the following analysis are

$$E_{xc} = \left[K_{1x}(\phi_x - \phi_c \cos\alpha_o) + K_{2x} p\right] + K_{3x}\beta \qquad (4.2\text{-}1)$$

$$E_{yc} = \left[K_{1y}(\alpha - \alpha_c) + K_{2y} q\right] \qquad (4.2\text{-}2)$$

$$E_{zc} = \left[K_{1z}(\phi_z - \phi_o \sin\alpha_o) + K_{2z} r\right] + K_{3z}\beta \qquad (4.2\text{-}3)$$

where $K_{1x}, \ldots, K_{3z}$ are the APS feedback gains; α_c and ϕ_c are the angle of attack and bank angle commands, respectively; and E_{xc}, E_{yc} and E_{zc} are the roll, pitch and yaw thruster command signals. These command signals command the respective thruster to fire in either a bang-bang switching manner or a digitized switching manner, as shown in Fig. 4.2-1. The aerodynamic control is accomplished by the ailerons, rudders and elevons. The basic longitudinal and lateral-directional feedback control laws used throughout the hypersonic and transition flight regime are the following:

$$\delta_{ac} = K_{VIA}\beta - K_{DA}(\phi_x - \phi_c \cos\alpha_o) - K_{RA} p \qquad (4.2\text{-}4)$$

$$\delta_{ec} = -K_{\alpha}(\alpha - \alpha_c) - K_q q \qquad (4.2\text{-}5)$$

$$\delta_{rc} = K_{VIR}\beta - K_{DR}(\phi_z - \phi_c \sin\alpha_o) - K_{RR} r \qquad (4.2\text{-}6)$$

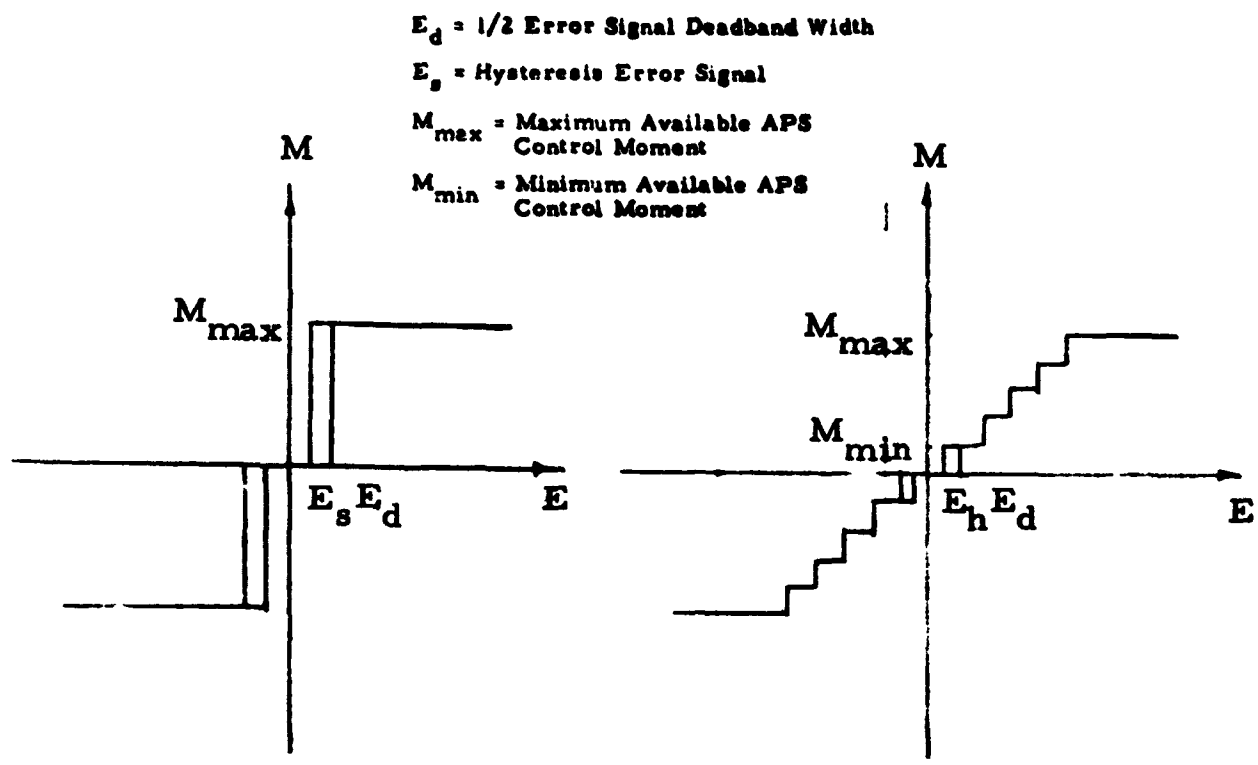

(a) Bang-Bang Control (b) Digitized APS Control

Fig. 4.2-1 - APS Control Switching Lines

where δ_{ac}, δ_{ec} and δ_{rc} are the aileron, elevon and rudder deflection commands; and K_{VIA}, K_{DA}, K_{RA}; K_{α}, K_q; K_{VIR}, K_{DR}, K_{RR} are the aerodynamic control feedback gains. These feedback gains can initially stabilize the shuttle reentry flight. Additional feedbacks can be made to further improve the stability and controlability of the shuttle; however, the basic method used in analytical and hybrid computer analyses remains unchanged. The dynamics of the control surfaces and the hydraulic actuators can be expressed as:

$$\dot{\delta}_a = K_{\delta_{av}}(\delta_{ac} - \delta_a) \tag{4.2-7}$$

$$\dot{\delta}_e = K_{\delta_{ev}}(\delta_{ec} - \delta_e) \tag{4.2-8}$$

$$\dot{\delta}_r = K_{\delta_{rv}}(\delta_{rc} - \delta_r) \tag{4.2-9}$$

where $K_{\delta av}$, $K_{\delta ev}$, and $K_{\delta rv}$ are the actuator time constants. All the aerodynamic control surface feedback gains in the above equations can be determined by mathematical analysis or hybrid simulation and optimization. A detailed discussion of feedback gain synthesis for aerodynamic control which can yield desired closed-loop vehicle characteristics will be given in Section 4.3. It uses a simplified form of the shuttle equations of motion (Eqs. (4.1-16) through (4.1-20)) and the aerodynamic control laws given in Eqs. (4.2-4), (4.2-5), and (4.2-6).

A block diagram of a digitized APS controller is shown in Fig. 4.2-2a. If the digitized switching line is approximated by a linear switching line with an appropriate slope as shown in Fig. 4.2-2b and a random noise, then the original block diagram can be redrawn as shown in Fig. 4.2-2c. This approximation enables the nonlinear digitized APS controller to be analyzed by linear techniques. The mean-square value of the linearization error is approximately one-twelfth the square of a step. The random noise may be treated as uniformly districuted noise. The random noise effect on the system is ignored in the analytical study but can be easily investigated through the high-speed hybrid simulation.

To facilitate the linearized APS analysis, and the blending study of aerodynamic surface control and APS control, all the time-varying coefficients and control signals related to the APS are redefined as:

$$K^*_{22} = K_{27} \frac{(M_{x(p)})_{max}}{(\delta_a)_{max}}$$

$$K^*_{23} = K_{28} \frac{(M_{z(p)})_{max}}{(\delta_r)_{max}}$$

$$K^*_{31} = K_{34} \frac{(M_{y(p)})_{max}}{(\delta_e)_{max}}$$

$$K^*_{38} = K_{28} \frac{(M_{x(p)})_{max}}{(\delta_a)_{max}}$$

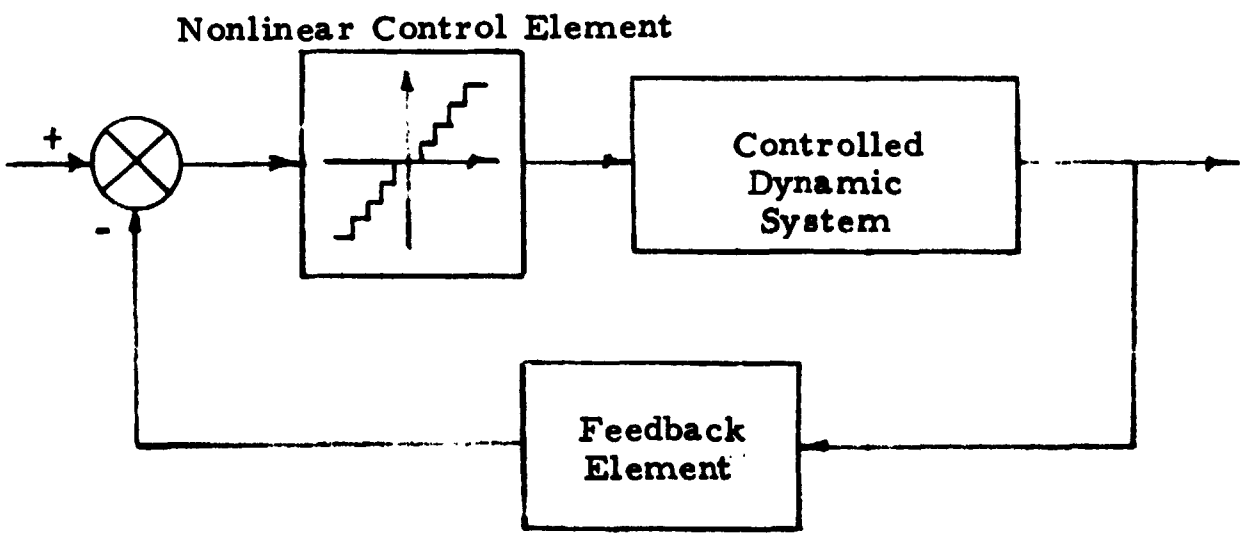

(b) Block Diagram of the Original System

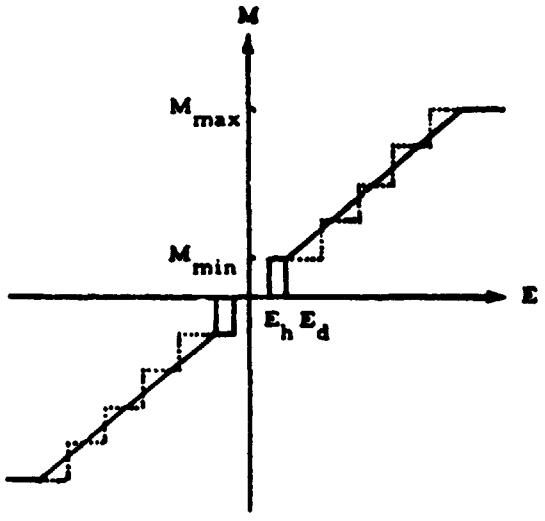

E_d = 1/2 Error Signal Deadband Width

E_s = Hysteresis Error Signal

M_{max} = Maximum Available APS Control Moment

M_{min} = Minimum Available APS Control Moment

The staircase switching line is approximated by straight lines in the simulation.

(b) Linearized Digitized Switching Lines

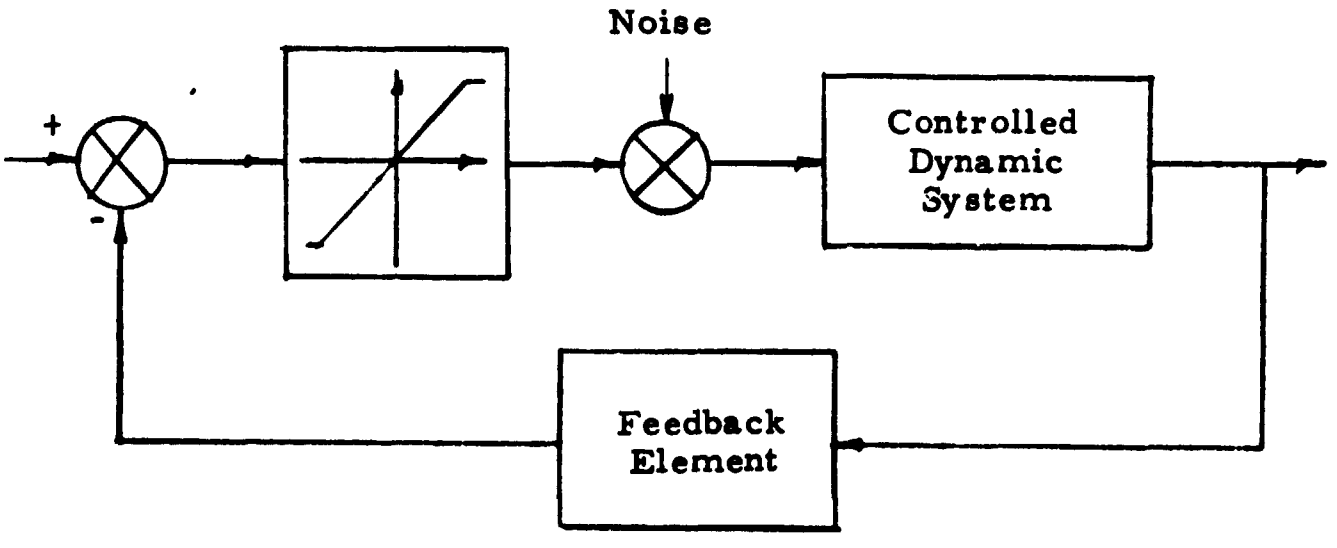

(c) Block Diagram of the Linearized System

Fig. 4.2-2 - Approximation of a Digitized APS Control System to a Linearized APS Controlled System

$$K^*_{39} = K_{43} \frac{(M_{z(p)})_{max}}{(\delta_r)_{max}}$$

$$\delta^*_{ac} = E_{xc} \frac{(\delta_a)_{max}}{(M_{x(p)})_{max}}$$

$$\delta^*_{ec} = E_{yc} \frac{(\delta_e)_{max}}{(M_{y(p)})_{max}}$$

$$\delta^*_{rc} = E_{zc} \frac{(\delta_r)_{max}}{(M_{z(p)})_{max}}$$

where $(M_{x(p)})_{max}, \ldots, (\delta_r)_{max}$ are the maximum values of $M_{x(p)}, \ldots,$ δ_r, respectively. Equations (4.1-16) through (4.1-20) can be rewritten as:

$$\dot{\alpha} = K_1\beta + K_2\alpha + K_3 q + K_4\phi + \left[K_5\delta_e\right] \tag{4.2-10}$$

$$\dot{\beta} = K_8\beta + K_9\alpha + K_{10}P + K_{11}q + K_{12}r + K_{13}\phi + \left[K_{14}\delta_a + K_{15}\delta_e + K_{16}\delta_r\right] \tag{4.2-11}$$

$$\dot{p} = K_{20}\beta + K_{21}\dot{\beta} + K_{24}p + K_{25}q + K_{26}r + \left[K_{22}\delta_a + K^*_{22}\delta^*_a + K_{23}\delta_r + K^*_{23}\delta^*_r\right] \tag{4.2-12}$$

$$\dot{q} = K_{29}\alpha + K_{30}\dot{\alpha} + K_{32}q + K_{33}p + K_{34}r + \left[K_{31}\delta_e + K^*_{31}\delta^*_e\right] \tag{4.2-13}$$

$$\dot{r} = K_{36}\beta + K_{37}\dot{\beta} + K_{40}p + K_{41}q + K_{42}r + \left[K_{38}\delta_a + K^*_{38}\delta^*_a + K_{39}\delta_r + K^*_{39}\delta^*_r\right] \tag{4.2-14}$$

where δ^*_{ac} , $\delta^*_{ec} = \delta^*_e$, $\delta^*_{rc} = \delta^*_r$ are used (i.e., idealized APS control dynamics). Since $K_6 f_{x(p)}$, $K_7 f_{z(p)}$; and $K_{17} f_{x(p)}$, $K_{18} f_{y(p)}$ and $K_{19} f_{z(p)}$ are of higher order of magnitude in comparison with the rest of terms in Eqs. (4.1-16) and (4.1-17), respectively, they are omitted to simplify the investigation. The APS control laws given in Eqs. (4.2-1), (4.2-2), and (4.2-3) can be written as

$$\delta^*_{ac} = K^*_{VIA}\beta - K^*_{DA}(\phi_x - \phi_c \cos\alpha_o) - K^*_{RA} p \qquad (4.2\text{-}15)$$

$$\delta^*_{ec} = -K^*_{\alpha}(\alpha - \alpha_c) - K^*_q q \qquad (4.2\text{-}16)$$

$$\delta^*_{rc} = K^*_{VIR}\beta - K^*_{DR}(\phi_z - \phi_c \sin\alpha_o) - K^*_{RR} p \qquad (4.2\text{-}17)$$

where

$$K^*_{VIA} = K_{3x}\frac{(\delta_a)_{max}}{(M_{x(p)})_{max}}, \quad K^*_{DA} = -K_{1x}\frac{(\delta_a)_{max}}{(M_{x(p)})_{max}}, \quad K^*_{RA} = -K_{2x}\frac{(\delta_a)_{max}}{(M_{x(p)})_{max}};$$

$$K^*_{\alpha} = -K_{1y}\frac{(\delta_e)_{max}}{(M_{y(p)})_{max}}, \quad -K^*_q = -K_{2y}\frac{(\delta_e)_{max}}{(M_{y(p)})_{max}};$$

$$K^*_{VIR} = K_{3z}\frac{(\delta_r)_{max}}{(M_{z(p)})_{max}}, \quad K^*_{DR} = -K_{1z}\frac{(\delta_r)_{max}}{(M_{y(p)})_{max}}, \quad K^*_{RR} = -K_{\cdot}\frac{(\delta_r)_{max}}{(M_{z(p)})_{max}}$$

Clearly, Eqs. (4.2-10) through (4.2-14) are the linearized perturbation equations of motion for shuttle reentry with linear controllers. The aerodynamic control laws are the same as those ginve by Eqs. (4.2-4), (4.2-5), and (4.2-6). The APS control laws are given by Eqs. (4.2-15), (4.2-16), and (4.2-17). The technique develoned for synthesizing aerodynamic control surface feedback gains can be adapted to the determination of linearized APS control feedback gains. In the aerodynamic control gain synthesis, δ^*_a, δ^*_e and δ^*_r are assumed to be zero; whereas in the APS control gain synthesis, δ_a, δ_e and δ_r are assumed to be zero. From the definition of δ^*_a, δ^*_e and δ^*_r, it can be seen that they have the same maxima as δ_a, δ_e and δ_r. Therefore, K_{22} and

K^*_{22} can be considered as the measure of control effectiveness of the aileron and roll APS thrusters on roll, respectively. Similar relationships hold for K_{31} and K^*_{31} on pitch, and K_{39} and K^*_{39} on yaw. K_{23} and K^*_{23} can be considered as the measure of the cross coupling effect of the rudder and yaw APS thrusters on roll, respectively. A similar relationship holds for K_{38} and K^*_{38} on yaw. An order of magnitude analysis is performed on all the time-varying control effectiveness coefficients of GDC-B9U booster for the entire reentry flight. Two regimes of control effectiveness can, in general, be found for each axis: APS control dominant regime, and transition regime (both APS and aerodynamic control effective).

Since aerodynamic effects are very small in the APS control dominant regime, the terms involving aerodynamic effects can be omitted from the control analysis. The resulting equations of motion are so simple that a phase plane design of the APS controller can be easily performed. (A more detailed design analysis will be given in Appendix E.) The rotational equations of motion reduce to

$$\dot{\hat{P}} = \frac{\hat{L}}{I_x}, \qquad \dot{\hat{Q}} = \frac{\hat{M}}{I_y}, \qquad \dot{\hat{R}} = \frac{\hat{N}}{I_z} \tag{4.2-18}$$

All three equations are similar in form. Therefore, only one of the equations must be analyzed. Let $\hat{P} = \theta$ and θ_c = constant angular displacement command; then the errror (ϵ_1) and the error rate (ϵ_2) in angle can be written as

$$\epsilon_1 = \theta_c - \theta, \qquad \theta_2 = -\dot{\theta} \tag{4.2-19}$$

The rotational equations of motion for the x-body axis can be rewritten as

$$\dot{\epsilon}_1 = \epsilon_2 \qquad \dot{\epsilon}_2 = \pm \left| \frac{L}{I_x} \right| \tag{4.2-20}$$

The $\epsilon_1 - \epsilon_2$ phase plane trajectory for const $\frac{I_x}{L}$ is

$$\epsilon_1 = \pm \left|\frac{I_x}{L}\right| \frac{\epsilon_2^2}{2} + \epsilon_1(0) = \left|\frac{I_x}{L}\right| \frac{\epsilon_2^2(0)}{2} \qquad (4.2\text{-}21)$$

where $\epsilon_1(0)$ and $\epsilon_2(0)$ are the initial conditions in error and error rate. The trajectories for various $\left|I_x/I\right|$ are given in Fig. 4.2-3. A sketch of the switching curves are shown in Fig. 4.2-4. The optimum switch curves for minimum control torque level based on minimum time criterion are two segments of the parabola given by

$$\epsilon_1 = \pm \left|\frac{I_x}{2L_1}\right| \epsilon_2^2 \quad \text{and} \quad \left|\epsilon_2\right| \leq \sqrt{\left|\frac{L_1}{I_x}\left\langle\epsilon_1(0)\right\rangle_1\right|} \qquad (4.2\text{-}22)$$

The size of this minimum torque level, L_1, controlled region is dictated by the tolerable time for an error of $\langle\epsilon_1(0)\rangle_1$ to be reduced to zero. Similarly, the tolerable time for error $\langle\epsilon_1(0)\rangle_2$ to be reduced to zero determines the size of the L_2 controlled region, etc. The optimum switching curves are determined by the trajectory passing through

$$\left(\frac{1}{2}\left\langle\epsilon_1(0)\right\rangle_1, \quad -\sqrt{\left|\frac{L_1}{I_x}\left\langle\epsilon_1(0)\right\rangle_1\right|}\right)$$

controlled by torque L_2, and trajectory passing through

$$\left(-\frac{1}{2}\left[\epsilon_1(0)\right]_1, \quad \sqrt{\left|\frac{L_1}{I_x}\left\langle\epsilon_1(0)\right\rangle_1\right|}\right)$$

controlled by torque $-L_2$. These two segments of switching curves are defined by

$$\epsilon_1 = \pm\left\{\left|\frac{I_x}{2L_2}\right| \epsilon_2^2 + \frac{1}{2}\left[\left\langle\epsilon_1(0)\right\rangle_1 - \left|\frac{L_1 L_2}{I_x^2}\left\langle\epsilon_1(0)\right\rangle_1\right|\right]\right\} \qquad (4.2\text{-}23a)$$

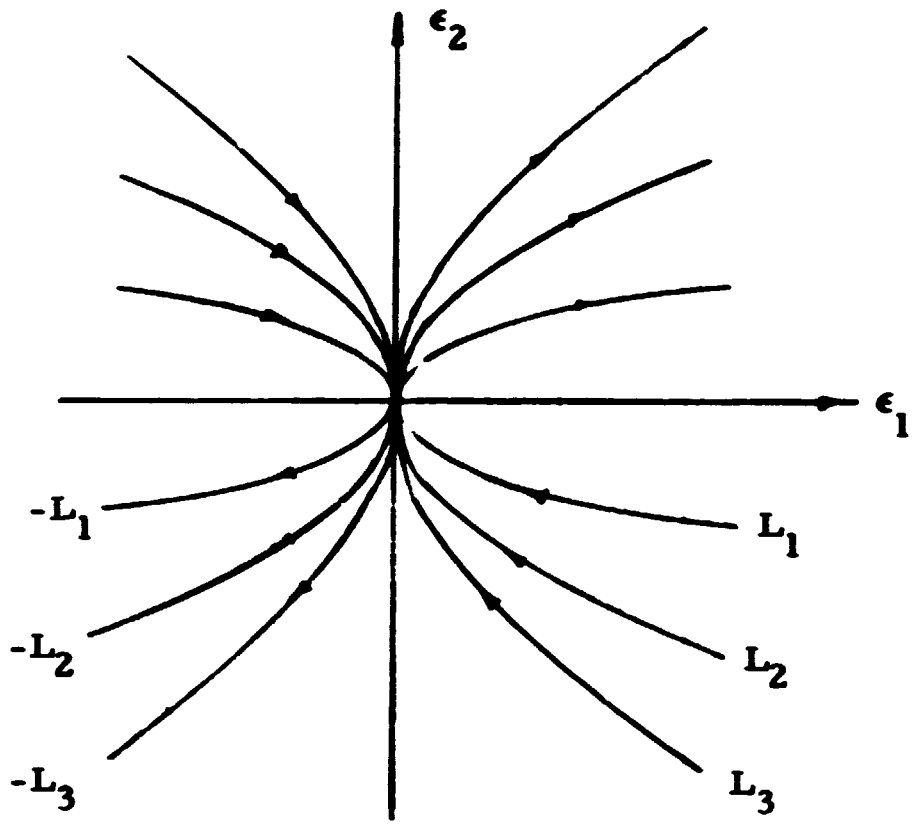

Fig. 4.2-3 - Phase Plane Trajectory for Various $|L_x/L|$

$L_1 < L_2 < L_3$

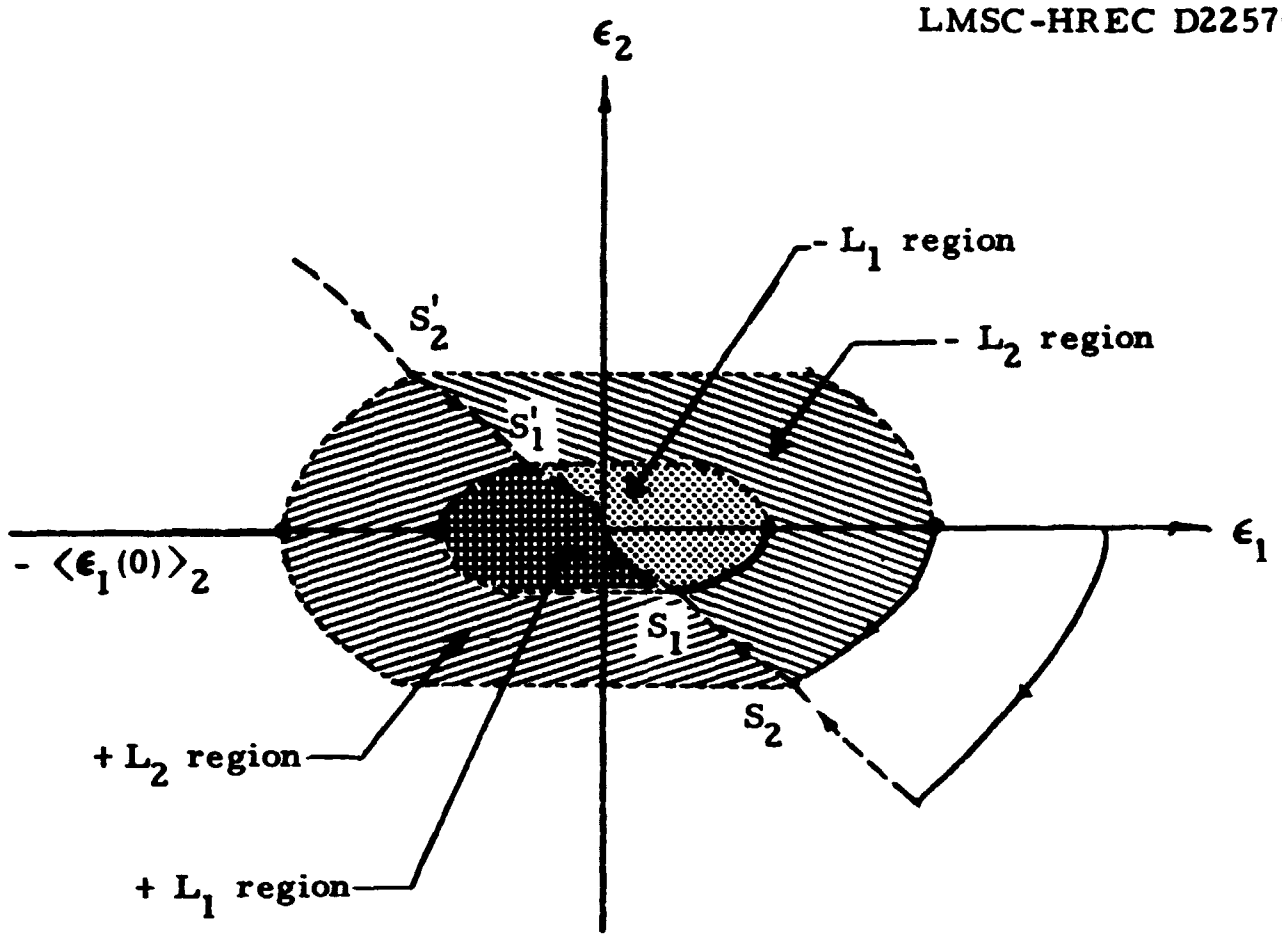

$$L_1 < L_2 < L_3$$

Fig. 4.2-4 - Switching Zones for a Digitized APS Controller

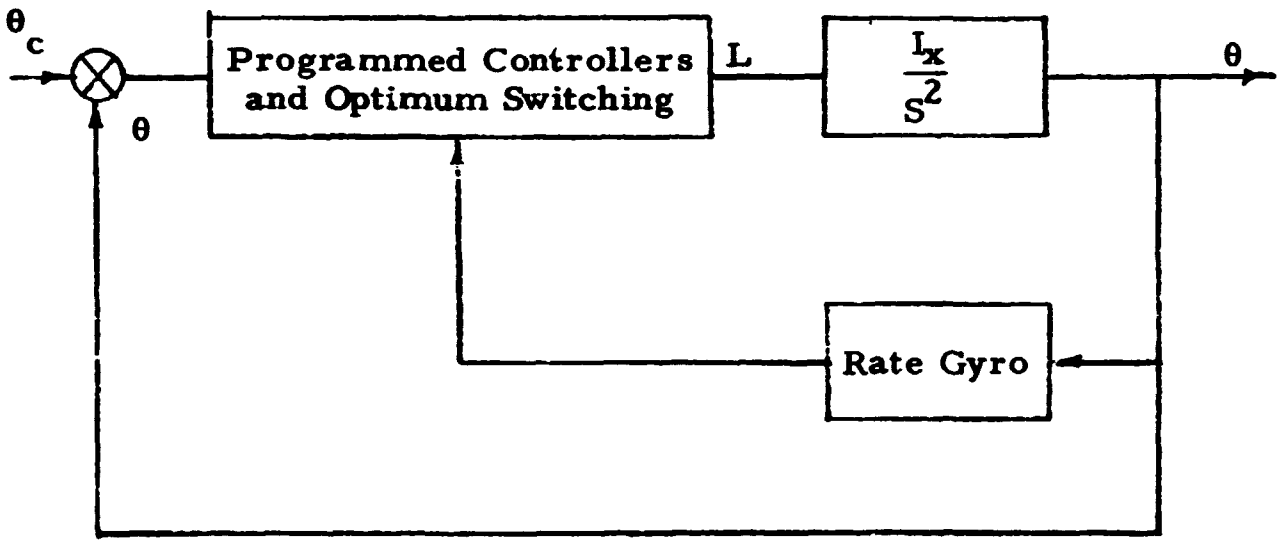

Fig. 4.2-5 - Block Diagram of the Digitized Roll Controller

and

$$\frac{L_1}{I_x}\left|\left\langle \epsilon_1(0)\right\rangle_1\right| \leq \left|\epsilon_2\right| \leq \left|\sqrt{\frac{L_2}{I_x}\left(\left\langle \epsilon_1(0)\right\rangle_2 - \left\langle \epsilon_1(0)\right\rangle_1\right)}\right| \qquad (4.2\text{-}23b)$$

The same approach can be applied to the determination of the segments of the switching curves with higher control torque levels. The resulting programmed controllers are neither time optimum nor fuel optimum but can be considered as a compromise between the two. The effect of a time delay on a single torque level APS controlled system is analyzed in detail in Appendix E. The optimum switching curves for a system with time delay are also derived in the same Appendix E. A block diagram of the digitized roll controller is shown in Fig. 4.2-5.

The linearized APS approach provides feedback gain schedules, whereas the phase plane approach gives optimum switching curves. Both approaches can be easily implemented; however, the linearized APS approach provides a method to tailor the system for the desired closed-loop characteristics, and is capable of producing "in phase" operation with the linear aerodynamic surface control system.

A block diagram of the preliminary longitudinal and lateral-directional flight control system is shown in Fig. 4.2-6. Two blending logic schemes (single control system operation logic and mixed systems operation logic) are investigated in the region where both APS and aerodynamic control are effective. The single control system operation logic uses input command, disturbance, and feedbacks to select a system for control. The total control effort, M_c, for each axis can be expressed as the sum of aerodynamic and APS control efforts

$$M_c = K\delta + K^*\delta^* \qquad (4.2\text{-}24)$$

and

$$(M_c)_{max} = (M_{c(a)})_{max} + (M_{c(p)})_{max}$$

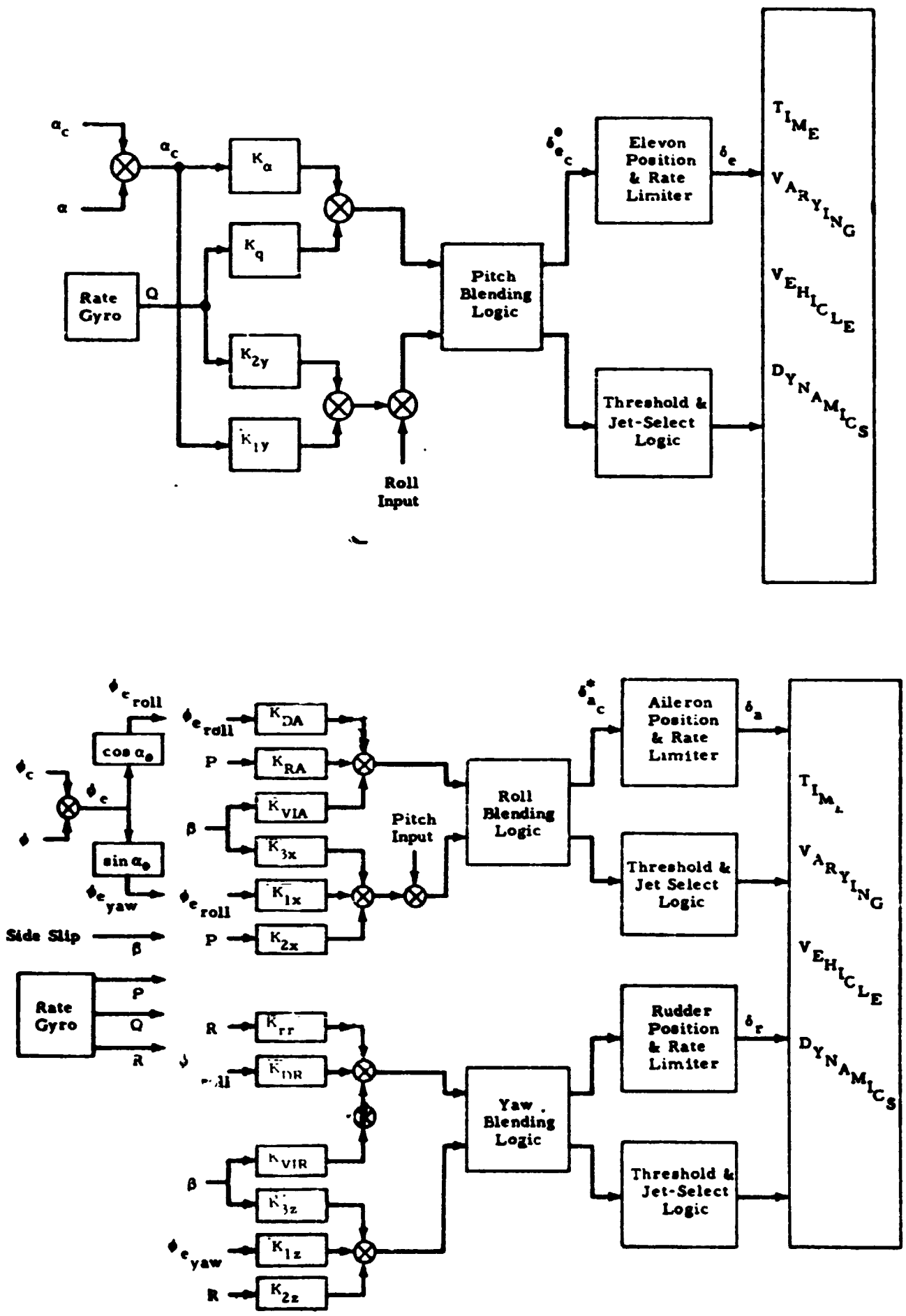

Fig. 4.2-6 - Longitudinal and Lateral Directional Flight Control Systems

where

$$K = K_{22},\ K_{31},\ K_{39}; \qquad K^* = K^*_{22},\ K^*_{31},\ K^*_{39};$$

$$\delta = \delta_a,\ \delta_e,\ \delta_r; \qquad \delta^* = \delta^*_a,\ \delta^*_e,\ \delta^*_r$$

for roll, pitch, and yaw, respectively; $(M_{c(a)})_{max}$ and $(M_{c(p)})_{max}$ are the maximum aerodynamic and APS control efforts, respectively. If the computed aerodynamic control surface command δ_c is smaller than the deflection limit, δ_{max}, then aerodynamic control is used

$$M_c = K\,\delta_c$$

Otherwise, if $\delta_{c2} > \delta_{max}$, APS control is used

$$M_c = K^*\delta^*_{c2}$$

as shown in Fig. 4.2-7a, where δ^*_{c2} corresponds to the computed APS command with no aerodynamic control. The mixed control systems operation logic uses input command, disturbance and feedbacks to decide whether aerodynamic control effort is sufficient to meet the required performance and to provide appropriate APS firing commands if additional control effort is required for producing the desired performance. For $\delta_{c2} > \delta_{max}$, then

$$M_c = K\,\delta_{max} + K^*\,\frac{K(\delta_{c2} - \delta_{max})}{K^*}$$

$K(\delta_{c2} - \delta_{max})/K^*$ is used to determine firing command. For $\delta_{c1} < \delta_{max}$, then

$$M_c = K\,\delta_{c1}$$

Therefore, in this case, APS control can be viewed as an extension to aerodynamic control as shown in Fig. 4.2-7b. The coupling effect of the APS control efforts are assumed to be the same as for aerodynamic control for

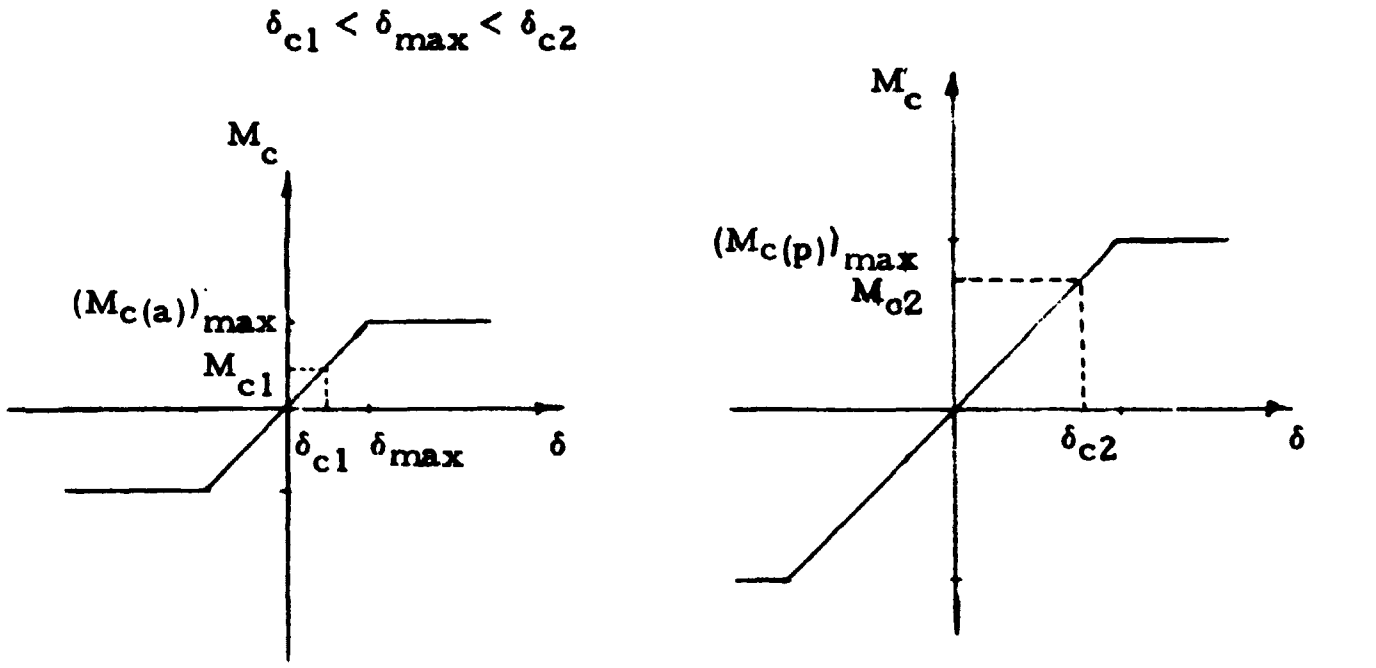

(a) Single Control System Operation Logic

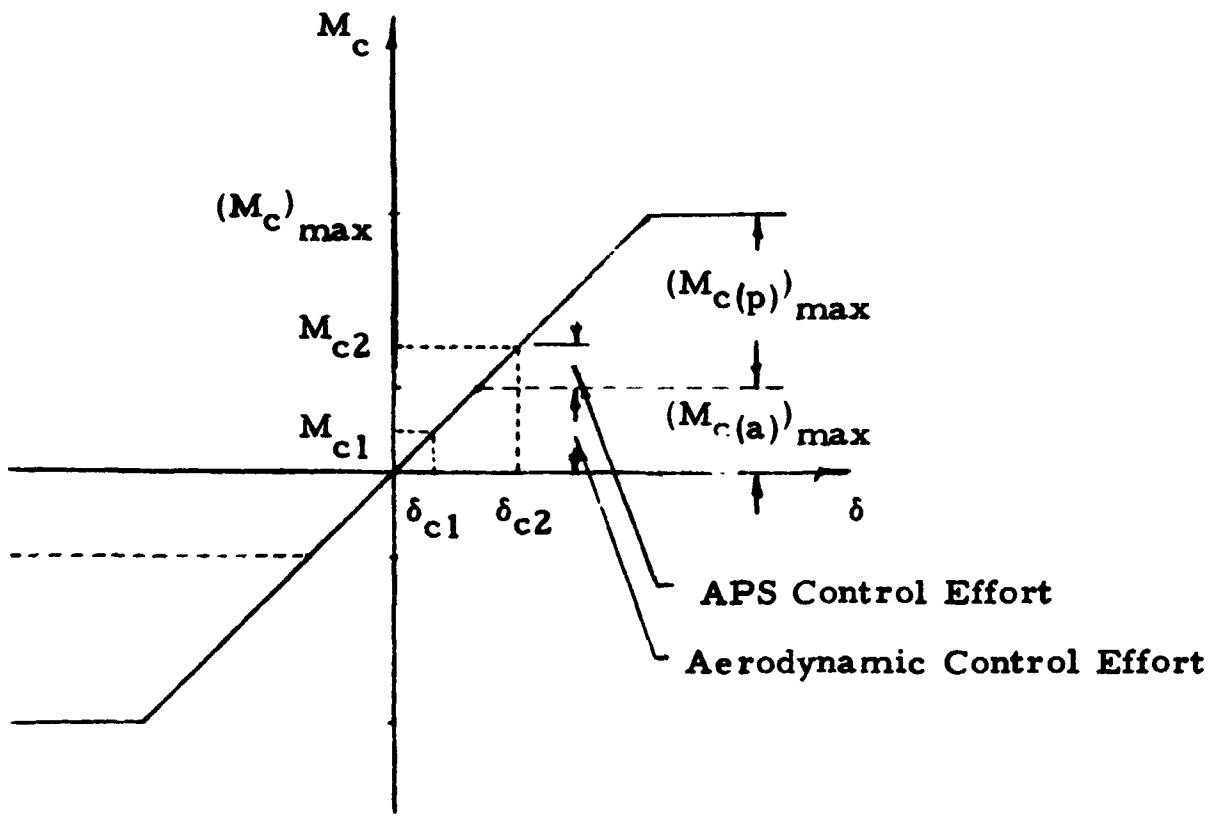

(b) Mixed Control Systems Operation Logic

Fig. 4.2-7 - Two Blending Logic Schemes

simplicity. This mixed control systems operation logic allows the change of δ_{max} and $\dot{\delta}_{max}$ without compromise in performance by increasing the APS control effort, and has a higher controlability and flexibility.

4.3 CONTROL GAIN SYNTHESIS

The determination of stability and control characteristics from vehicle, environment, and wind tunnel data has become an important part of flight study. As the reentry vehicle flies in wide range of Mach and altitude regions, there is the need to determine the various influences on stability characteristics and to predict flight behavior. The analysis and optimization of a reentry vehicle-control system is best accomplished through servo analysis techniques in which the vehicle is considered as a transfer element. In this approach the dynamic properties of the vehicle are defined by a series of transfer functions which relate output quantities (various vehicle motions) to input variables (usually control motions or external disturbances). These transfer functions are readily derived from the linearized and Laplace transformed vehicle equations of motion (Eq. (4.1-16) through (4.1-20)). The coefficients of these transfer functions are composed of combinations of vehicle nominal states, vehicle stability derivatives, inertial, and gravitational parameters. These transfer function forms are widely used in work involving stability and control, handling qualities, automatic flight control, etc. They can be factored into ratios of first and second order polynomial products and gain factors. The gains, poles and zeros thus obtained define the fundamental properties of the dynamic elements. They are essential in most servo analysis and synthesis methods and in response calculations. The factorization required is time consuming since most of the polynomials involved are of third or higher order and include time-varying coefficients. The poles and zeros of these higher order polynomials are difficult to define in terms of the transfer function coefficients or of the stability parameters. These are both related to the response characteristics in a very complex manner.

It is highly desirable to decompose a fairly complete transfer function form by the use of fewer airframe degrees of freedom. This simplification can help in:

1. Developing the insight required for the determination of airframe automatic control combinations which offer possible improvements in overall system complexity.

2. Assuming the effects of variations in stability derivatives upon vehicle responses.

3. Showing the detailed effects of particular stability derivatives upon vehicle responses.

The linearized rigid body equations describing the perturbed lateral and longitudinal airframe motion about the reference trajectory (Eqs. (4.1-16) through (4.1-20)) with zero initial conditions and inputs due only to control surface deflection can be simplified by omitting insignificant terms, and are given in Laplace transform style.

Longitudinal Set

$$(S - K_2)\alpha - K_3 q = K_5 \delta_e \tag{4.3-1}$$

$$(-K_{30}S - K_{29})\alpha + (S - K_{32})q = K_{34}\delta_e \tag{4.3-2}$$

Lateral Set

$$(S - K_8)\beta - (K_{10}S + K_{12})\phi - K_{12}r = K_{14}\delta_a + K_{16}\delta_r \tag{4.3-3}$$

$$-K_{20}\beta + (S^2 - K_{24}S)\phi - K_{26}r = K_{22}\delta_a + K_{23}\delta_r \tag{4.3-4}$$

$$-K_{36}\beta - K_{40}S + (S - K_{42})r = K_{38}\delta_a + K_{39}\delta_r \tag{4.3-5}$$

The longitudinal motions of rigid airframe can be separated into long period and short period categories. The assumption of $v = 0$ used in the derivation of translational perturbation equations of motion has essentially eliminated the long period motion. Equations (4.3-1) and (4.3-2) are known to yield an approximation to the short period motion which is a relatively fast oscillation of angle of attack and pitch angle.

The lateral motions of a rigid airframe can be separated into spiral, roll subsidence and Dutch roll modes. The spiral mode involves at least two-degrees-of-freedom yawing and rolling and results in a very small root of the lateral characteristic equations. The roll subsidence mode is associated primarily with the rolling behavior of the airframe and is a large root of the lateral characteristic equation. The Dutch roll mode is relatively fast oscillation of sideslip angle and yaw angle.

The development of an airframe-control system tailoring procedure is needed in the preliminary design of a stabilization system to make the airframe satisfy the mission and/or performance requirements. A detailed examination of the control loop system shows that the methods of equivalent stability derivatives is very suitable to this type of analytical treatment. In order to force attention upon the airframe rather than the control system, it is assumed in the following analyses that both the actuator and the sensor dynamics are ideal.

In the equivalent stability derivative approach to closed-loop flight control analyses, a controller deflection is made proportional to an airframe output motion dependent variable. This controller deflection imposes a force and/or moment upon the vehicle, which is proportional to airframe motion dependent quantities. The action of the control system in producing an airframe motion dependent force and moment can then be thought of as modifying a vehicle stability derivative. (That is, it augments or creates an effective airframe stability derivative.) Since the airframe transfer function approximation factors are given in terms of airframe stability derivatives having α, β, p, q, r subscripts, the entire effect of gain feedback involving these quantities can be assessed directly from the augmented transfer function. Since the characteristic roots are expressed implicitly in terms of augmented stability derivatives, inertial characteristics, etc., the ties between the gain feedbacks and closed-loop operation can be established.

For longitudinal stability analyses, consider a control system consisting of a rate gyro which is oriented to measure the pitching velocity, and an angular sensor to provide angle of attack information. The servo actuator then moves the elevon in response to the gyro and sensor signals. If servo and sensor dynamics are neglected and the system assumed is linear, the controller transfer function is

$$\delta_{e_c} = -K_\alpha(\alpha-\alpha_c) - K_q q \qquad (4.3\text{-}6)$$

With no command or controller disturbance inputs, this becomes

$$\delta_e = -K_\alpha \alpha - K_q q$$

and Eqs. (4.3-1) and (4.3-3) can be rewritten as

$$(S - K_2) + (K_3 - K_\alpha)\alpha + (-K_3 + K_5 - K_q)q = 0 \qquad (4.3\text{-}7)$$

$$(-K_{30}S - K_{29} + K_{39}K_\alpha)\alpha + (S - K_{32} + K_{31}K_q)q = 0 \qquad (4.3\text{-}8)$$

Clearly, the action of the control loop in this case augments all the longitudinal stability derivatives. By considering the controller operation in the above manner, one can determine gain feedbacks for desired closed-loop roots. Let the desired longitudinal short period characteristics be defined by:

$$S^2 + 2\xi_{sp}\omega_{sp}S^1 + \omega_{sp}^2 S^0 = 0 \qquad (4.3\text{-}9)$$

where ξ_{sp} and ω_{sp} are the desired short period damping and frequency, respectively. The longitudinal characteristic equation can be obtained from Eqs. (4.3-7) and (4.3-8) as

$$S^2 + \left[a_1K_\alpha + a_2K_q + a_3\right]S^1 + \left[b_1K_\alpha + b_2K_q + b_3\right]S^0 = 0 \qquad (4.3\text{-}10)$$

where

$$a_1 = K_5$$

$$a_2 = K_{31} + K_{40} K_5$$

$$a_3 = -(K_2 + K_{32} + K_3 K_{30})$$

$$b_1 = (-K_5 K_{32} + K_3 K_{31})$$

$$b_2 = (-K_2 K_{31} + K_{29} K_5)$$

$$b_3 = (K_2 K_{32} - K_3 K_{29})$$

Equating coefficients of S^1 and S^0 terms in Eqs. (4.3-9) and (4.3-10), respectively, there results

$$a_1 K_\alpha + a_2 K_q + a_3 = 2 \xi_{sp} \omega_{sp} \qquad (4.3\text{-}11)$$

$$b_1 K_\alpha + b_2 K_q + b_3 = \omega_{sp}^2 \qquad (4.3\text{-}12)$$

Therefore K_α and K_q can be obtained from Eqs. (4.3-11) and (4.3-12) in terms of the coefficients of the longitudinal set of equations of motion and the desired longitudinal short period mode characteristics.

$$K_\alpha = \frac{b_2(2 \xi_{sp} \omega_{sp} - a_3) - a_2(\omega_{sp}^2 - b_3)}{(a_1 b_2 - a_2 b_1)} \qquad (4.3\text{-}13)$$

$$K_q = \frac{a_1(\omega_{sp}^2 - b_3) - b_1(2 \xi_{sp} \omega_{sp} - a_3)}{(a_1 b_2 - a_2 b_1)} \qquad (4.3\text{-}14)$$

The gains schedules $K_\alpha(t), K_q(t)$ can be easily computed by a digital computer from the known value of time-varying coefficients of longitudinal equations of motion with fixed ω_{sp} and ξ_{sp}.

If the lateral controller transfer functions are given as

$$\delta_{a_c} = K_{VIA}\beta - K_{DA}(\phi_x - \phi_c \cos\alpha_o) - K_{RA}p \qquad (4.3\text{-}15)$$

$$\delta_{r_c} = K_{VIR}\beta - K_{DR}(\phi_z - \phi_c \sin\alpha) - K_{RR}r \qquad (4.3\text{-}16)$$

With no command or controller disturbance inputs, then

$$\delta_a = K_{VIA}\beta - K_{DA}\phi_x - K_{RA}p \qquad (4.3\text{-}17)$$

$$\delta_r = K_{VIR}\beta - K_{DR}\phi_z - K_{RR}r \qquad (4.3\text{-}18)$$

and Eqs. (4.3-3), (4.3-4), and (4.3-5) can be rewritten as

$$\left[S - K_8 - K_{14}K_{VIA} - K_{15}K_{VIR}\right]\beta + \left[(-K_{10} + K_{14}K_{RA})S + (-K_{14} + K_{15} - K_{DA})\right]\phi_x + \left[(-K_{12} + K_{15}K_{RR})S + (K_{15}K_{DR})\right]\phi_z = 0 \qquad (4.3\text{-}19)$$

$$\left[-K_{20} - K_{22}K_{VIA} - K_{23}K_{VIR}\right]\beta + \left[(S^2 + (-K_{24} + K_{22}K_{RA})S + (K_{22}K_{DA})\right]\phi_x + \left[(-K_{26} + K_{23}K_{RR})S + (K_{23}K_{DR})\right]\phi_z = 0 \qquad (4.3\text{-}20)$$

$$\left[-K_{35} - K_{38}K_{VIA} - K_{39}K_{VIR}\right]\beta + \left[(-K_{20} + K_{38}K_{RA})S + (K_{38}K_{DA})\right]\phi_x + \left[S^2 + (-K_{42} + K_{39}K_{RR})S + (K_{39}K_{DR})\right]\phi_z = 0 \qquad (4.3\text{-}21)$$

where $\dot{\phi}_x \cong p$, $\dot{\phi}_z \cong r$ are used.

The action of the lateral control loop in this case augments all the lateral stability derivatives. In principle, one can follow the same procedure as for determination of longitudinal gain feedbacks to obtain gain feedbacks from the above set of equations for desired closed-loop characteristics.

However, the algebra involved may be quite complex. Let the desired lateral characteristics be defined by

$$(S^2 + 2\xi_{dr}\omega_{dr}S + \omega_{dr}^2)(S + \frac{1}{T_s})(S + \frac{1}{T_r}) = 0 \qquad (4.3\text{-}22)$$

or

$$S^4 + \left[2\xi_{dr}\omega_{dr} + \frac{1}{T_s} + \frac{1}{T_r}\right]S^3 + \left[\omega_{dr}^2 + \frac{1}{T_sT_r} + 2\omega_{dr}\xi_{dr}(\frac{1}{T_s} + \frac{1}{T_r})\right]S^2$$

$$+ \left[\omega_{dr}^2(\frac{1}{T_s} + \frac{1}{T_r}) + \frac{2\xi_{dr}\omega_{dr}}{T_sT_r}\right]S^1 + \left[\frac{\omega_{dr}^2}{T_sT_r}\right]S^0 = 0$$

where ξ_{dr} and ω_{dr} are the damping and frequency of the desired Dutch roll mode, and T_s and T_r are the desired time lags of the spiral and the roll subsidence modes, respectively. The lateral characteristic equation can be obtained from Eqs. (4.3-19) through (4.3-21) as:

$$S^4 + A_3S^3 + A_2S^2 + A_1S^1 + A_0S^0 = 0 \qquad (4.3\text{-}23)$$

where $\beta \cong \sin\alpha_o\phi_x - \cos\alpha_o\phi_z$ is used in the derivation for simplicity.

Equations (4.3-16) and (4.3-17) indicate that there are six gain feedbacks to be determined. However, by equating coefficients of same order in Eqs. (4.3-22) and (4.3-23), there are only four algebraic equations. Two additional conditions must be supplied. For this case, these conditions are so chosen that the effect of the nominal angle of attach, α_o, can be eliminated from the computation of the gain feedbacks:

$$K_{37}K_{VIA} + K_{38}K_{VIR} + K_{35} = 0 \qquad (4.3\text{-}24)$$

$$K_{21}K_{VIR} + K_{22}K_{VIR} + K_{19} = 0 \qquad (4.3\text{-}25)$$

or

$$K_{VIR} = \frac{(K_{22}K_{36} - K_{20}K_{38})}{(K_{33}K_{38} - K_{22}K_{38})} \tag{4.3-26}$$

$$K_{VIA} = -\frac{K_{36}}{K_{38}} - \frac{K_{39}}{K_{38}}\left[\frac{K_{22}K_{35} - K_{20}K_{38}}{K_{33}K_{38} - K_{22}K_{39}}\right] \tag{4.3-27}$$

The coefficients of Eq. (4.3-23) can be expressed as

$$A_3 = \left[K_{22}K_{RA} - K_{24} + K_{38}K_{RR} - K_{42}\right] \tag{4.3-28}$$

$$\begin{aligned} A_2 = \Big[&K_{39}K_{DR} + K_{22}K_{DA} + K_{39}K_{RR}K_{22}K_{RA} + K_{42}K_{24} - K_{42}K_{22}K_{RA} \\ &- K_{24}K_{39}K_{RR} - K_{40}K_{25} - K_{38}K_{RA}K_{23}K_{RR} \\ &+ K_{40}K_{23}K_{RR} + K_{26}K_{38}K_{RA}\Big] \end{aligned} \tag{4.3-29}$$

$$\begin{aligned} A_1 = \Big[&K_{39}K_{DR}K_{22}K_{DA} - K_{42}K_{22}K_{DA} + K_{22}K_{RA}K_{39}K_{DR} - K_{29}K_{39}K_{DR} \\ &+ K_{40}K_{23}K_{DR} - K_{38}K_{RA}K_{23}K_{DR} + K_{38}K_{DA}K_{26} \\ &- K_{38}K_{DA}K_{23}K_{RR}\Big] \end{aligned} \tag{4.3-30}$$

$$A_0 = \left[K_{39}K_{DR}K_{22}K_{DA} - K_{38}K_{DA}K_{23}K_{DR}\right] \tag{4.3-31}$$

Evidently, the gain feedbacks for the desired lateral characteristics can be obtained from Eqs. (4.3-28) through (4.3-31) if

$$A_3 = 2\xi_{dr}\omega_{dr} + \frac{1}{T_s} + \frac{1}{T_r} \tag{4.3-32}$$

$$A_2 = \omega_{dr}^2 + \frac{1}{T_s T_r} \quad 2\omega_{dr}\xi_{dr}\left(\frac{1}{T_s} + \frac{1}{T_r}\right) \tag{4.3-33}$$

$$A_1 = \omega_{dr}^2 \left(\frac{1}{T_s} + \frac{1}{T_r}\right) + \frac{2\,\omega_{dr}}{T_s T_r} \tag{4.3-34}$$

$$A_0 = \frac{\omega_{dr}^2}{T_s T_r} \tag{4.3-35}$$

After much algebraic manipulation, the above equations can be reduced to:

$$B_6 K_{DR}^6 + D_5 K_{DR}^5 + B_4 K_{DR}^4 + B_3 K_{DR}^3 + B_2 K_{DR}^2 + B_1 K_{DR} + B_0 = 0 \tag{4.3-36}$$

$$K_{RR} = \left[C_2 K_{DR}^2 + C_1 K_{DR} + C_0\right] / \left[D_2 K_{DR}^2 + D_0\right] \tag{4.3-37}$$

$$K_{DA} = A_0 / \left[K_{22} K_{39} K_{DR} - K_{38} K_{23} K_{DR}\right] \tag{4.3-38}$$

$$K_{RA} = \left[A_0 + K_{24} + K_{42} - K_{39} K_{RR}\right] / K_{22} \tag{4.3-39}$$

where $B_0, \ldots, B_6$; $C_0, \ldots, C_2$; D_0, D_2 are complex functions of the coefficients of Eqs. (4.3-3) through (4.3-5) as well as A_0, A_1 and A_3 obtained from Eqs. (4.3-35), (4.3-34) and (4.3-32), respectively. A digital computer must be employed to solve the above set of equations and to compute numerical values for the gain feedbacks.

Equation (4.3-36) has six roots. It is known that only real roots are the realizable gain feedbacks, and all the complex roots are eliminated. Furthermore, since Eqs. (4.3-29) and (4.3-33) have not been used in the above algebraic manipulation, they are used to determine the best set of gain feedbacks. The simplest logic is to substitute each set of gain feedbacks into right-hand side of Eq. (4.3-29). Then the set which has numerical results closest to the computed value of Eq. (4.3-33) is chosen as the best set of gain feedbacks.

A digital computer "Synthesis" program is written to compute all the gain feedbacks used in Eqs. (4.3-6), (4.3-15) and (4.3-16). A complete set of the plots of all the resulting synthesized gain schedules for the GDC-B-9U reentry is given in Appendix E.

4.4 REENTRY CONTROL RELATED PENALTIES AND SENSITIVITY ANALYSIS

A major element in the determination of space shuttle APS and aerodynamic blending logic is the minimization of control system related weight. It can be obtained by direct optimization of penalty functions which are formulated by the coordinated efforts of many disciplines such as aerodynamics, thermodynamics, structures and control. The sensitivity of the penalties are determined by each discipline by relating weight to factors associated with performance penalties such as trajectory deviations, dynamic response, APS and aerodynamic control effectiveness.

4.4.1 Thermal Protection System

Both the auxiliary propulsion system (APS) and the aerodynamic control system disturb the local flow about the surface of the reentry vehicle which leads to substantial increases in the heating near the locations of the APS engines or aerodynamic control surfaces. To withstand this added heating, additional structure weight is required. Two variables are of prime importance in the determination of this increase in weight. These are, the magnitude of the increase in heating rate and the associated heating duration. Peak heating rate determines the heat shield structural configuration which must become heavier as the heating rate becomes more severe. As seen in Fig. 4.4-1 there is an increase associated with material changes at discrete temperatures as well as that expected from additional thickness requirements due to property degradation as the structural temperature increases. By summing all the heat pulses, the insulation weights necessary to protect the inner structure of the vehicle may be determined. The effect of the total heat absorbed into the surface on the insulation thickness are shown on Fig. 4.4-2. Two studies have been performed which provide inputs to the overall blending study concerning the increase in thermal protection system weight. These studies cover the firing of the APS engines and elevon deflection for the GPC-B9-U booster.

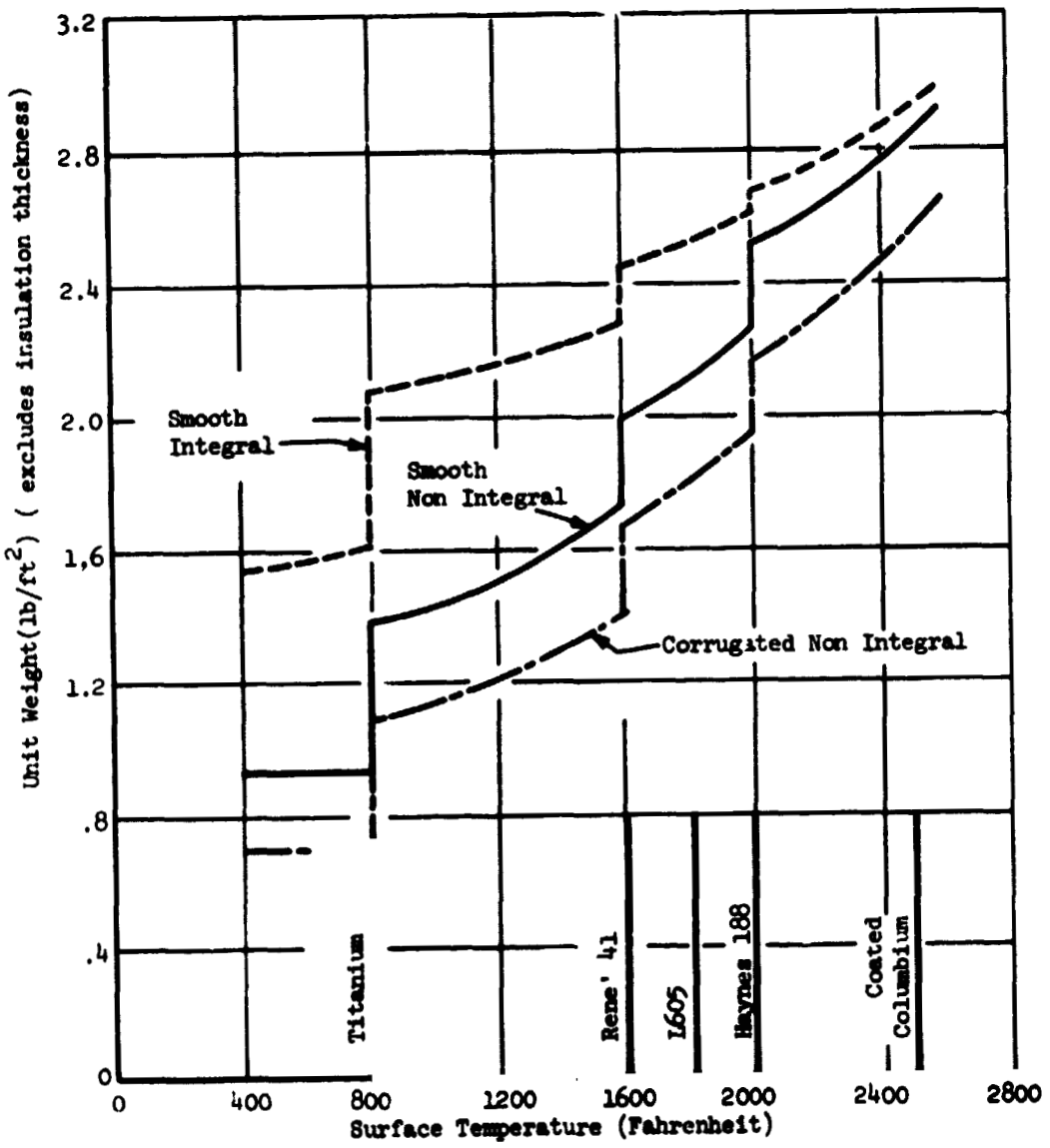

Fig. 4.4-1 - Undisturbed TPS Weights for Typical Construction on Space Shuttle Vehicles

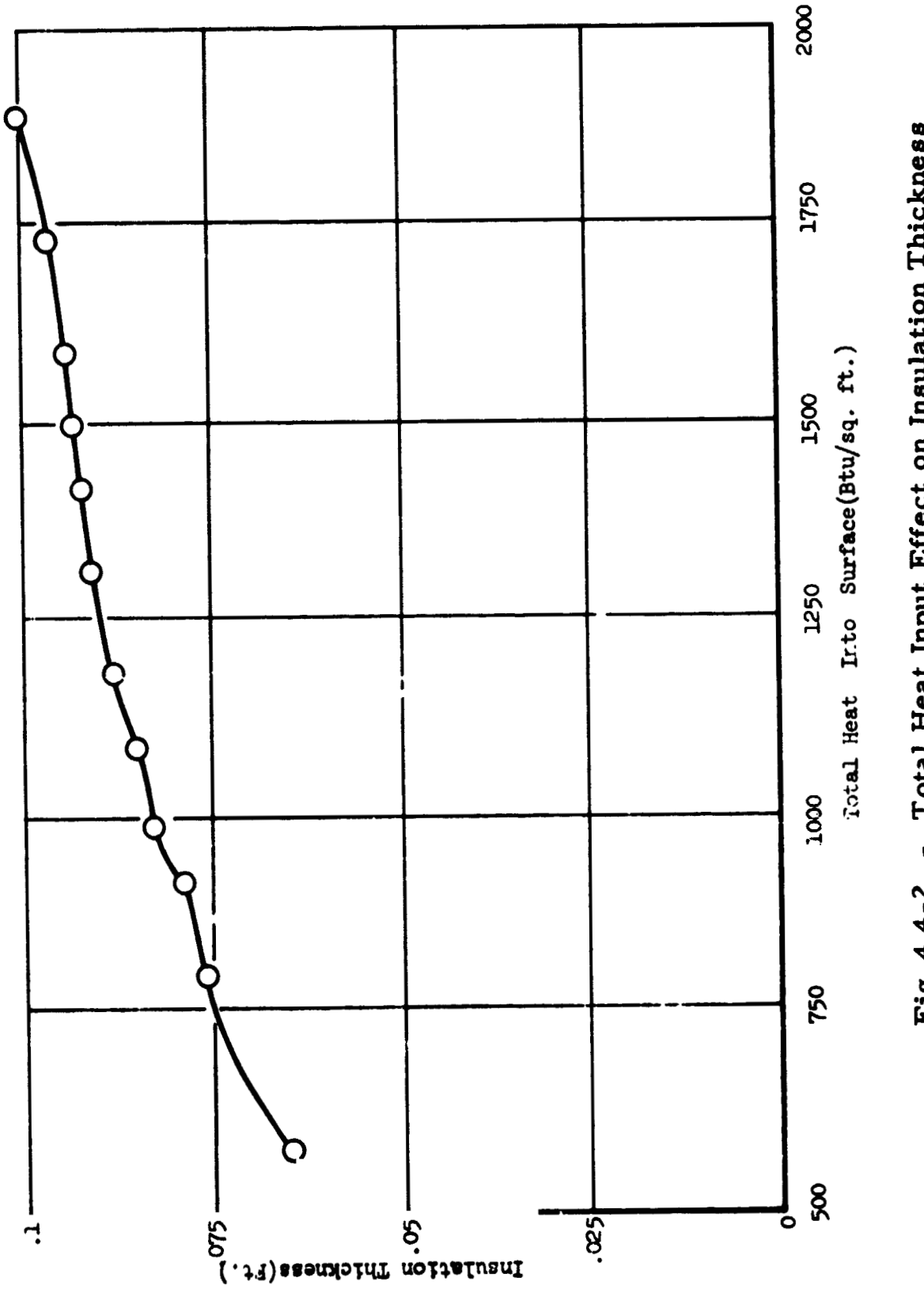

Fig. 4.4-2 - Total Heat Input Effect on Insulation

APS Related Heating

The existence of APS engines disturbs the environment and creates additional heating of the vehicle in both the firing and cutoff modes. Figure 4.4-3 shows the associated flow fields and heating distributions which are functions of nozzle chamber pressure and nozzle exit size for the firing case, and nozzle exit size only for the nonfiring case. A detailed investigation of the interference heating near the APS engines indicates that little or no increase in heating rate occurs for the case in which an engine is located on the leeward side. When an engine is located on the windward side, two different conditions may occur: (1) if the engine is firing, there is a separation region in front and back of the nozzle exit and a shock impingement region on each side of the exit sweeping backward along the surface; (2) in the cutoff mode no influence of the nozzle is felt upstream but inside the nozzle and immediately downstream of the nozzle an increase in heating rate can be observed. Figure 4.4-4 shows three regions of interest for an interference heating study of a thruster firing out the side of a plate into a supersonic freestream. All of these regions require different types of analysis, and test data are relied on heavily to provide engineering estimates of the interference heating. (1) Region 1, an area of increased heating behind the thruster, is due to the reattached boundary layer. The average heating rate in this region is about 30% higher than the undisturbed heating rate. (2) Region 2, an area just ahead of nozzle exit, is normally subjected to separated flow when the engine is firing. Since the chamber pressure is high in comparison with the freestream total pressure, the heating in this region is very high just ahead of the nozzle exit and the average heating is about twice the undisturbed value. (3) Region 3, an area in the shape of a "V" extending behind the APS nozzle, is subjected to an average heating of about 60% higher than the undisturbed value.

The average heating rates for clean body, $\dot{q}_{(clean)}$, near the yaw thrusters can be defined for a reference trajectory and is given in Fig. 4.4-5 as a function of time. The heating rates for firing and cutoff modes can be approximated by

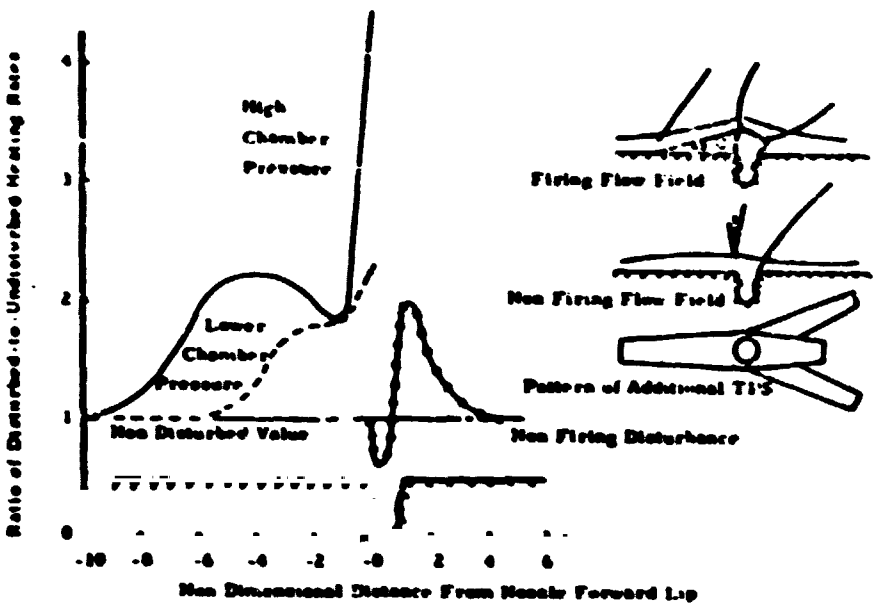

Fig. 4.4-3 - Influence of Firing and Nonfiring APS Engine on Local Surface Heating Rate

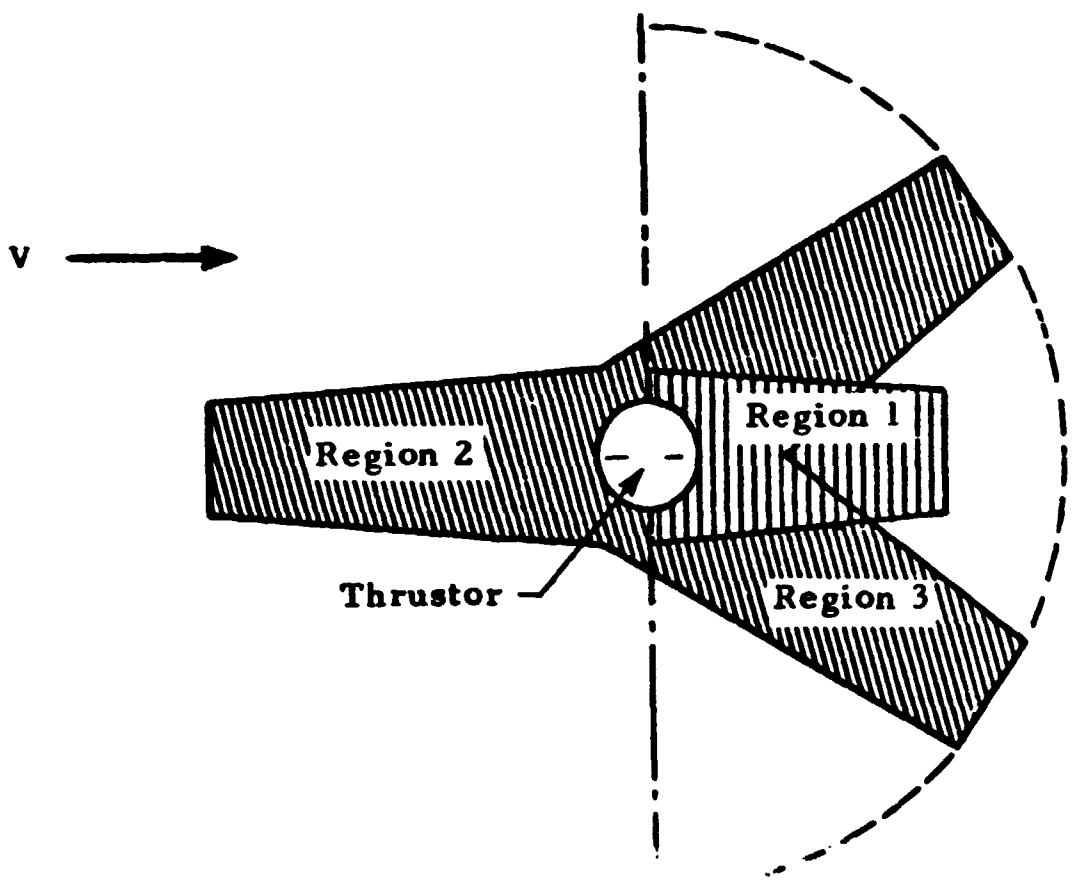

Fig. 4.4-4 - Three Regions of Interference Heating Studies

$$\dot{q}_{(firing)} \cong 1.7\, \dot{q}_{(clean)} \tag{4.4-1}$$

$$\dot{q}_{(nonfiring)} \cong 1.3\, \dot{q}_{(clean)} \tag{4.4-2}$$

The affected areas on each side of yaw thrusters are 300 ft^2 for firing mode and 20 ft^2 for cutoff mode, respectively. The equilibrium wall temperature can be computed from

$$T_{eq.\,wall} = (\dot{q})^{1/4}/(\sigma\epsilon)^{1/4} \tag{4.4-3}$$

where $\sigma = 0.476 \times 10^{-12}$ Btu/ft^2 - $^oR^4$ and $\epsilon = 0.8$. Then

$$T_{eq.\,wall(clean)} = 1275\, \dot{q}^{1/4}_{(clean)}$$

$$T_{eq.\,wall(nonfiring)} = 1360\, \dot{q}^{1/4}_{(clean)}$$

$$T_{eq.\,wall(firing)} = 1430\, \dot{q}^{1/4}_{(clean)}$$

The equivalent wall temperature is then used to determine the unit shingle (or skin) weight, w_s, as given in Fig. 4.4-1. Since the total shingle weight required can be expressed as

$$\overline{W}_s \cong A_{firing}\left[W_{s(firing)} - W_{s(clean)}\right] + A_{nonfiring}\left[W_{s(nonfiring)} - W_{s(clean)}\right] \tag{4.4-4}$$

it can be computed for the entire reentry flight and is shown in Fig. 4.4-6. The TPS shingle weight penalty due to firings can be expressed as

$$\Delta\overline{W}_s \cong \left[\overline{W}_s(t)\ \delta\ (t_f - t)\right]_{max} - \left[\overline{W}_s(t)\right]_{min} \qquad (4.4\text{-}5)$$

where t_f is the time firing is actually taking place and

$$\delta(t_f - t) = 1 \quad \text{for } t = t_f$$

$$= 0 \quad \text{for } t \neq t_f$$

It can be seen that the maximum weight saving attainable is approximately 80N. Evidently, the shingle weight penalty of TPS is very insensitive to the firing or nonfiring at anytime in the reentry flight.

The increased insulation weight can be obtained from the curve of insulation thickness versus integrated heating rate (Fig. 4.4-2). It is computed for continuous firing for the entire reentry flight and is also shown in Fig. 4.4-6. The TPS insulation weight penalty due to firings can be expressed as

$$\Delta\overline{W}_I \cong \sum_{i=1}^{n} W_I(t) \left[\delta\ (t_{fe}(i) - t) - \delta\ (t_{fs}(i) - t)\right] \qquad (4.4\text{-}6)$$

where $t_{fs}(i)$ is the starting time and $t_{fe}(i)$ is the ending time, both of the i^{th} firing. The total insulation weight for yaw thrusters with continuous firings is approximately 100 N; therefore, the insulation weight penalty is very insensitive to the number and durations of firings.

Control Surface Related Heating

The prediction of aerodynamic heating distributions on a deflected control surface is difficult because of the complex inviscid-viscous flow field interactions coupled with flow separation which may be either laminar, turbulent

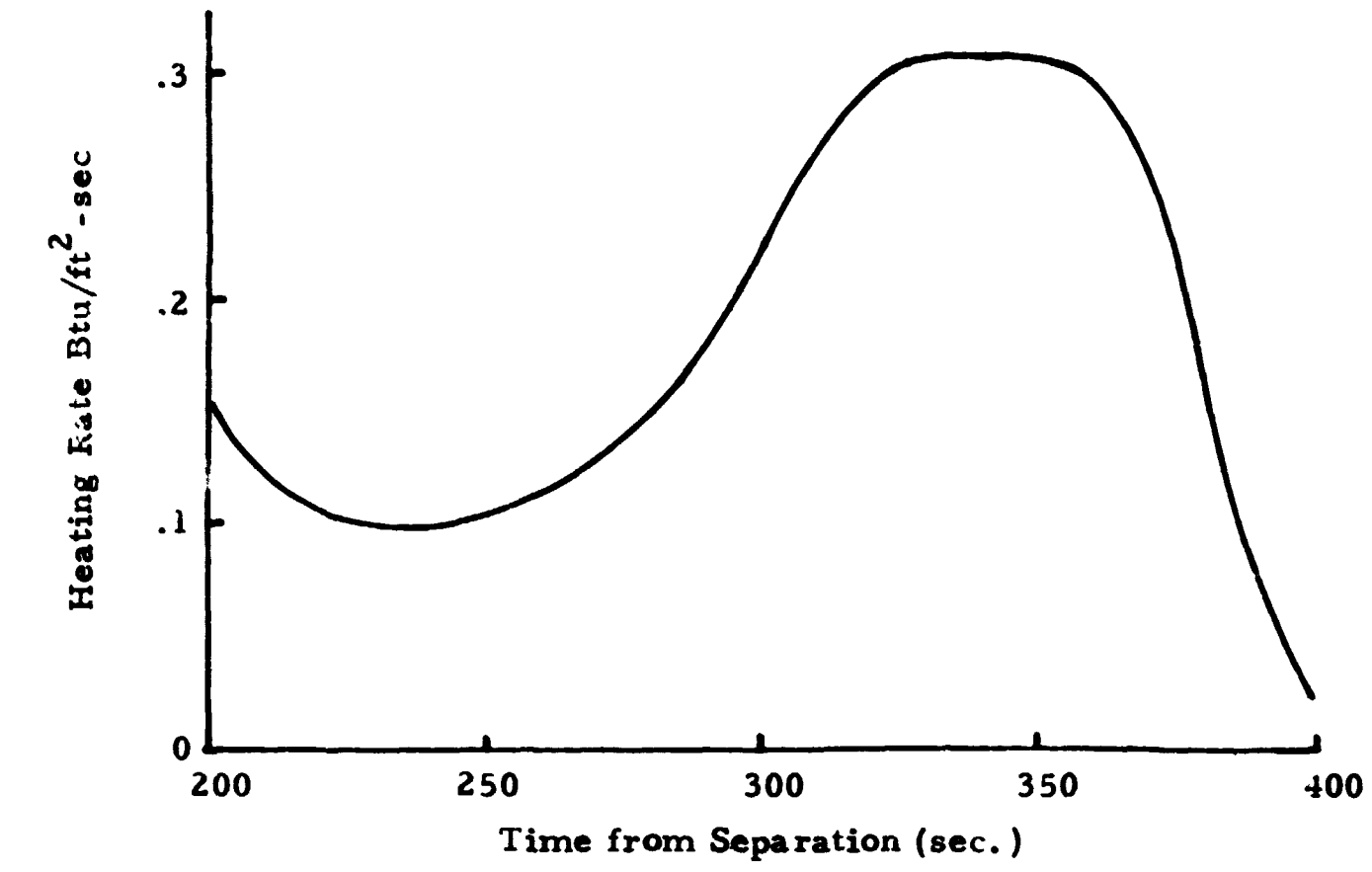

Fig. 4.4-5 - Heating Rates for Clean Body Near Yaw Thrusters

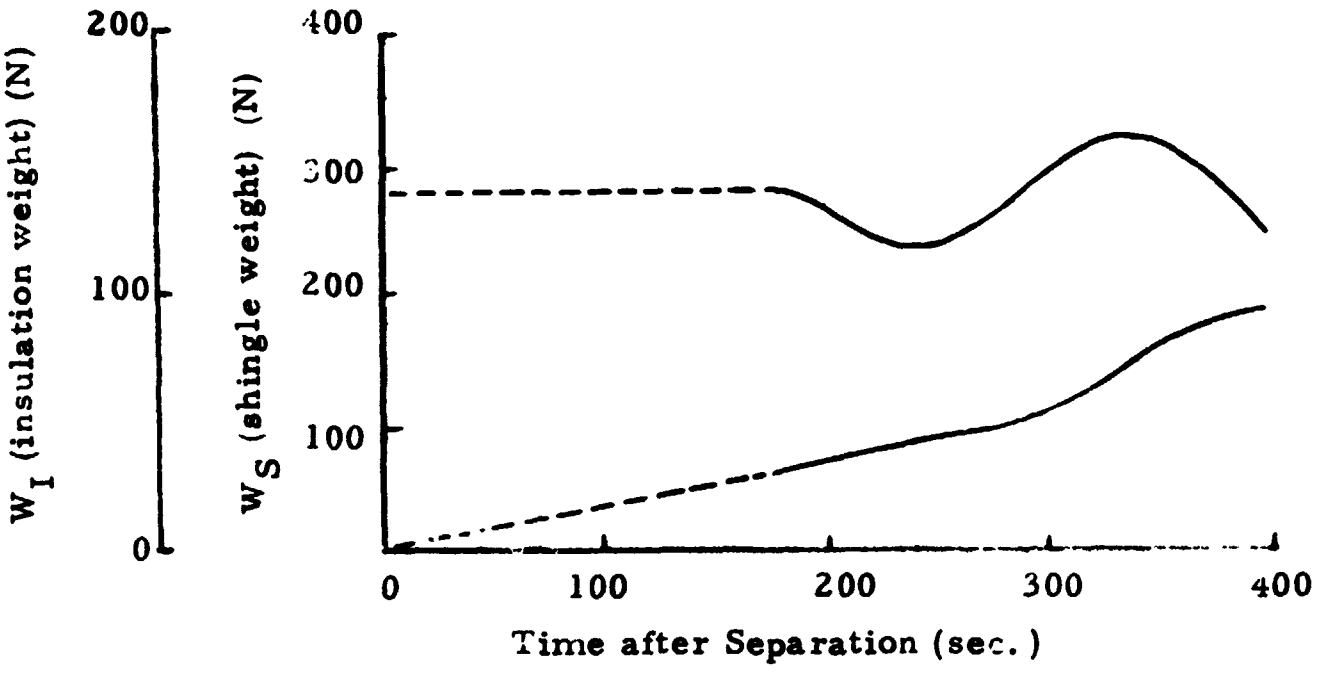

Fig. 4.4-6 - Sensitivities of Yaw Thruster TPS Weight

or transitory. All of these require different types of analyses, and the engineering estimate of the interference heating depends on both theoretical as well as test results. Figure 4.4-7 shows that there are two regions of interest. From the results of Refs. 8 and 9, the heating trends in Region 1 are found to (1) decrease at the beginning of separation, (2) hold nearly constant over most of the separated region, then (3) rise sharply near the compression corner. Though the consistency of the data leaves much to be desired, the net heating in Region 1 appears to average quite close to the undisturbed value. If the length of the flap (Region 2) is large compared to the boundary layer thickness, the heating rate will rise sharply to a peak value then stay fairly constant until the expansion at the back of the flap causes a sharp drop in the heating rate. The average heating in Region 2 was evaluated from a study of a variable span flap at Mach 8 and Mach 15 (Ref. 5). The average heating in Region 2 was found to be about 50% of the peak value. After the average heating rates have been defined for a nominal trajectory, the TPS weight penalty can be evaluated by calculating the equilibrium wall temperature as a function of time.

Figure 4.4-8 shows the heating rate on the elevons as a function of trajectory time and deflection angle. The heating rate for a non-zero elevon deflection angle can approximately be related to the zero deflection angle as follows

$$\dot{q}_{(\delta_e)} = \dot{q}_{(\delta_e=0)} \left[1 + 0.01\, \delta_e + 0.19 \sqrt{\delta_e} \right]$$

where δ_e is the elevon deflection angle. The equivalent wall temperature can be expressed as

$$T_{eq.\,wall} = \left[\frac{\dot{q}_{(\delta)} (T_{aw} - T_{eq.\,wall})}{\left(\frac{T_{aw} - 520}{\sigma \epsilon} \right)} \right]^{1/4} \qquad (4.4\text{-}7)$$

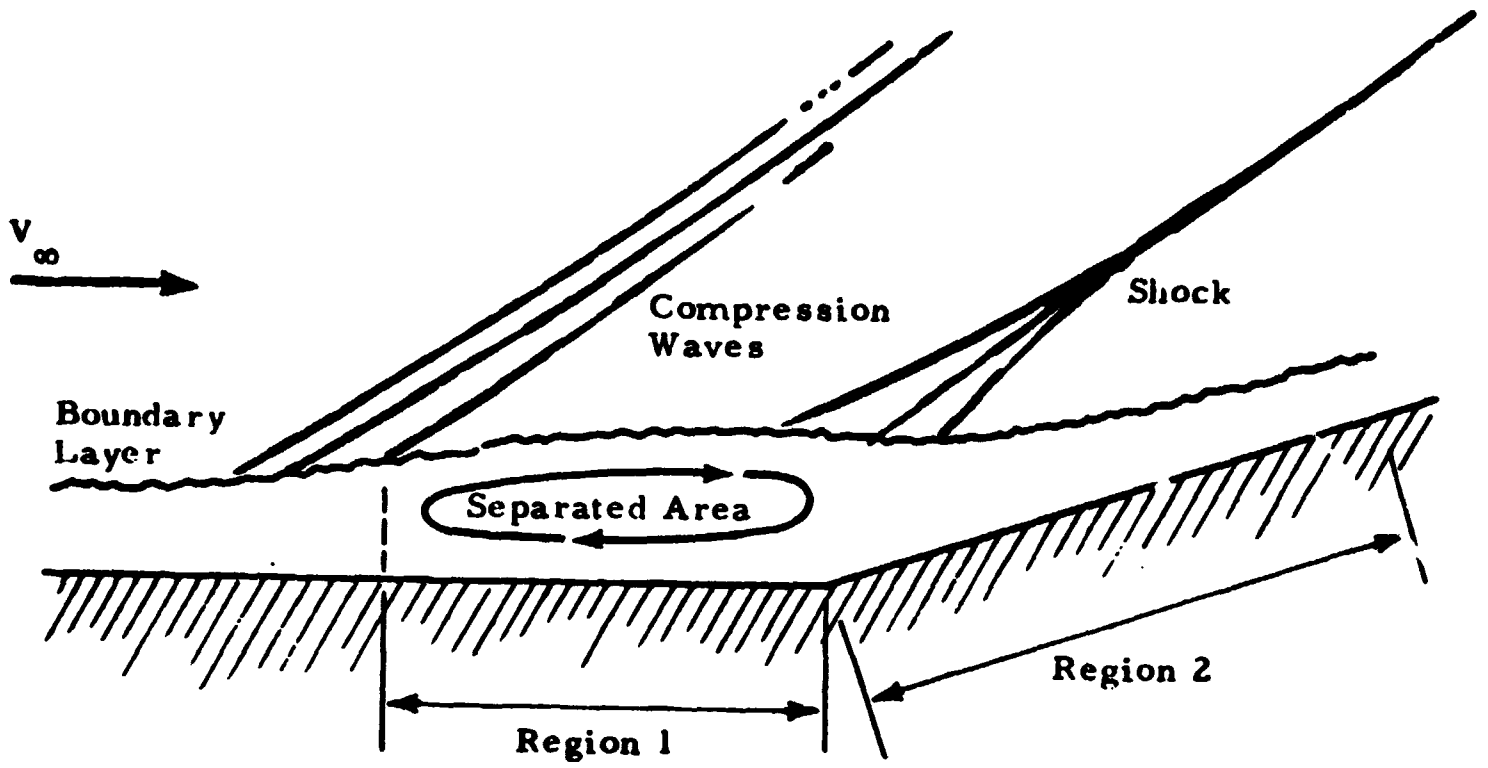

Fig. 4.4-7 - Two Regions Interference Heating Studies for Deflected Flap

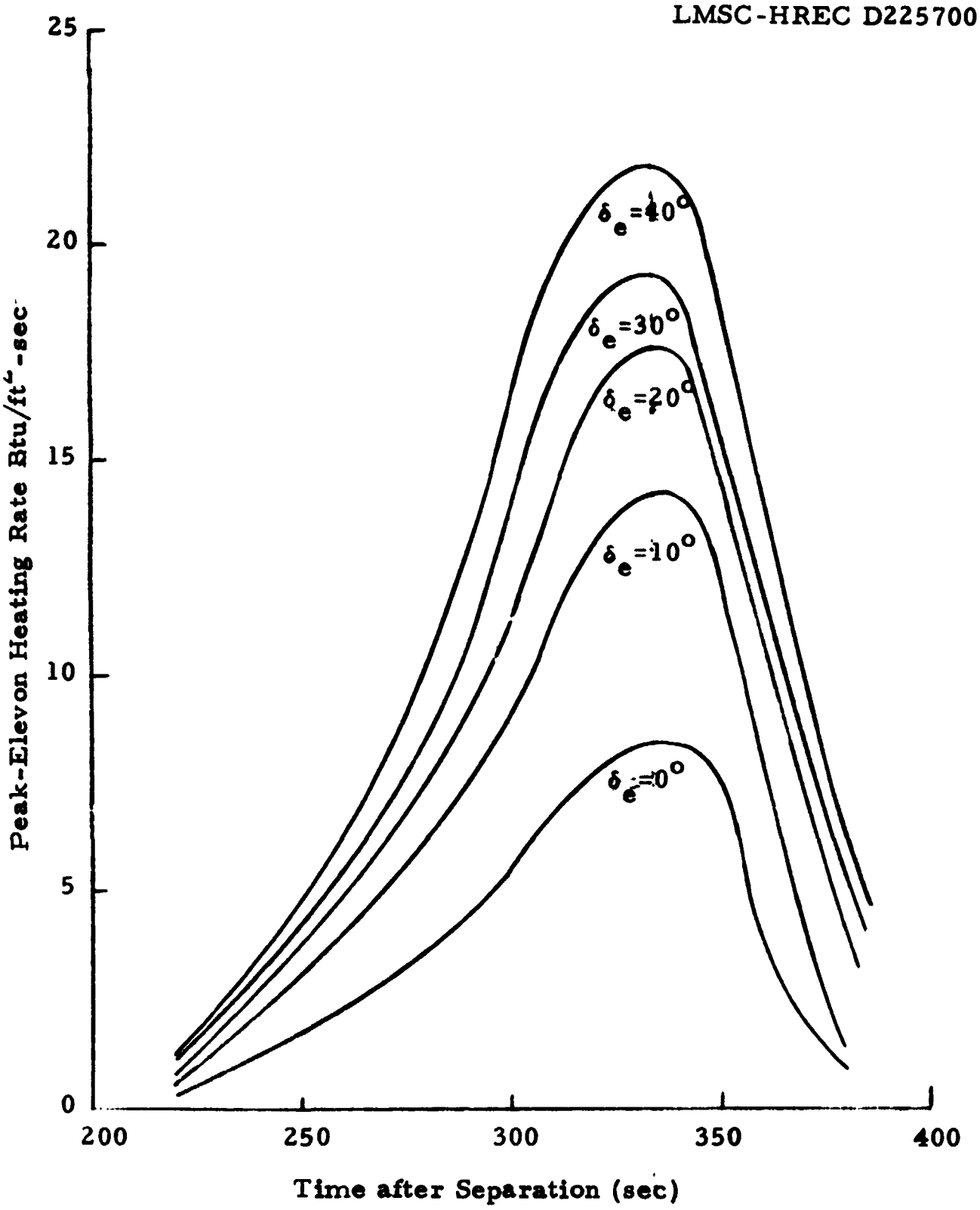

Fig. 4.4-8 - Heating Rates for Elevon at Various Deflection Angles

where T_{aw} is the adiabatic wall temperature which varies somewhat throughout the reentry trajectory. A constant value of 5500°R for the adiabatic wall temperature may be used which is a reasonable value during the high heating rate portion of the reentry. Figure 4.4-9 shows the computed equivalent wall temperature at various heating rates. The shingle weight penalty for elevon deflection can be determined from the equilibrium wall temperature as

$$\overline{W}_s = 2*A_{\delta_e}\left[W_{s(\delta_e)} - W_{s(\delta_e=0)}\right] \qquad (4.4\text{-}8)$$

where $A_{\delta_e} = 478$ ft.^{2} Also $\overline{W}_s$ can be determined from Fig. 4.4-1 for an equivalent wall temperature corresponding to the deflection angle and time of reentry. The sensitivity of the shingle weight penalty at the designed deflection angle can be obtained from the equation.

$$\left(\frac{\partial \overline{W}_s}{\partial \delta_e}\right)_T \doteq 2*A_{\delta_e}\left[W_{s(\delta_e)} - W_{s\,(\delta_{e\,\text{design}})}\right]/\Delta\delta e \qquad (4.4\text{-}9)$$

where $\Delta\delta_e = \delta_e - \delta_{e_{design}}$. This sensitivity is computed for the most important portion of reentry and is shown in Fig. 4.4-10. The insulation weight penalty for elevon deflections can be determined from the insulation thickness which is a function total heating

$$\overline{W_I} = 2*\rho*A_e\left[t_{(\delta_e)} \quad t_{(\delta_e=0)}\right] \qquad (4.4\text{-}10)$$

where $\rho = 3.5$ l^b/ft^3 for Microquartz. Also $t_{(\delta_e)}$ and $t_{(\delta_e=0)}$ are the required insulation thicknesses at δ_e and $\delta_e=0$, respectively, which are determined from Fig. 4.4-2 for the computed total heating corresponding to the deflection angle and time of reentry. The sensitivity of the insulation weight penalty at designed deflection angle can be obtained from

$$\left(\frac{\partial \overline{W_I}}{\partial \delta_e}\right)_T = 2 * \rho * \left[t_{(\delta_e)} - t_{(\delta_{e_{design}})}\right]/\Delta\delta_e \qquad (4.4\text{-}11)$$

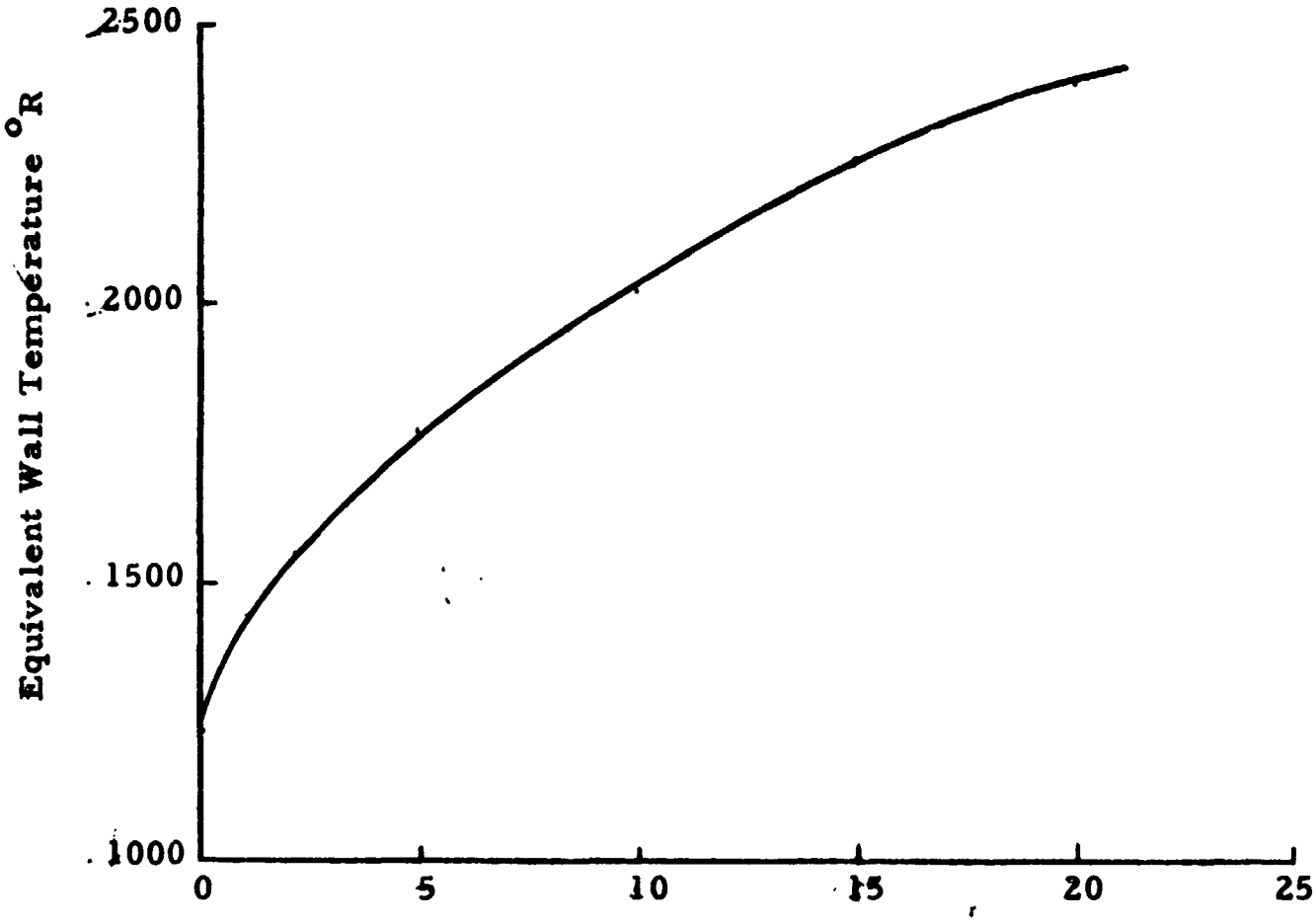

Fig. 4.4-9 Computed Equvalent Wall Temperature at Various Heating Rates

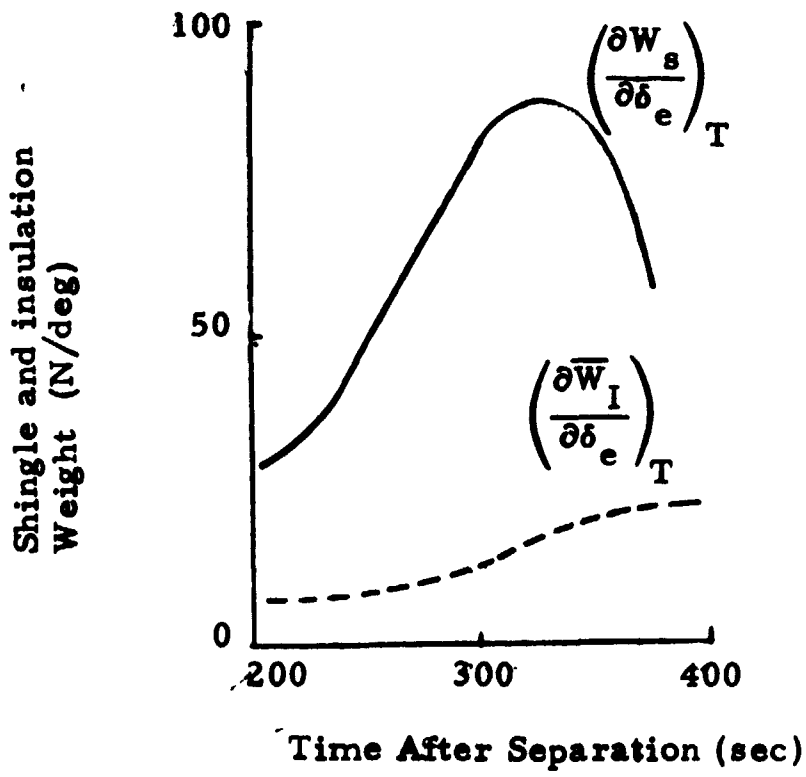

Fig. 4.4-10 Sensitivity of Elevon TPS Weight

This sensitivity is computed for the most important portion of reentry and is also shown in Fig. 4.4-10. This figure shows the TPS related elevon weight penalties are very insensitive to the variation from designed deflection angles. Following the same analysis as shown for elevon, the TPS related rudder weight penalties are found to be very insensitive to the variation from designed deflection angles.

4.4.2 Structural Weight

The general analysis of weight-strength characteristics of metal structures with a large number of design variables, side constraints and failure modes, such as buckling or maximum tensile stress, is not feasible for the purpose of this application. It would require efficient nonlinear computational algorithms. Instead, it is possible to generate design tables for a small number of candidate designs in which just a few design variables are left open. This allows the structural weight to be found instantly for a large variety of loading intensities, although the absolute optimum weight considering all possible design variations may not be reached exactly. Design tables of this kind, however, make it possible to predict weight trends caused by loading from flight control mechanisms. Figure 4.4-11 shows an additional aerodynamic control force near the tip caused by a control surface deflection. This force generates a moment on the hinge between the control surface and the main wing. Wing skin carries the resulting bending moment through tension and compression N_x. The spars carry the shearing force V along. The ribs provide intermediate support for the covers to reduce their buckling length. A finite element model can be constructed which approximates the structure by bars and shear panels. Lockheed-Huntsville's fully stressed design program can be used to determine the relation between the optimum design weight and the aerodynamic load condition.

A finite element model for the Booster B-9U main wing has been constructed and is shown in Fig. 4.4-12. It consists of bars and shear panels. For each bar an initial and a minimum cross section area and an allowable tensile and compressive stress is chosen, and for each shear panel an initial and a minimum thickness and an allowable shearing stress is chosen. Lockheed-Huntsville's fully stressed design program iteratively finds a design in which all elements are fully stressed unless minimum gages constrain the redesign path.

The current model has 158 joints, 516 bars and 143 shear panels, a total of 659 elements. The material properties of titanium are used. In an initial effort the following design loads were chosen:

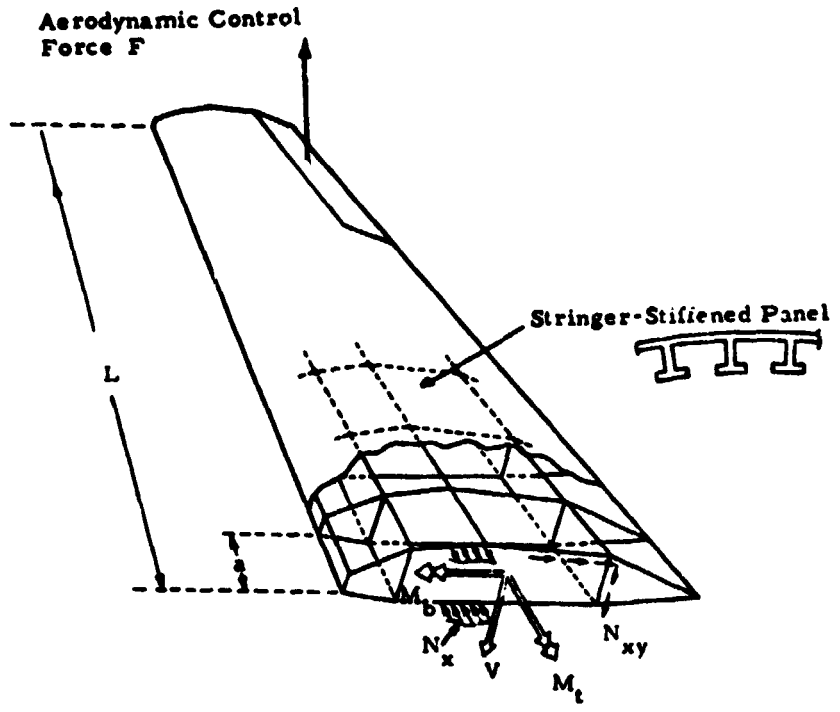

Fig. 4.4-11 - Wing Weight as a Function of Wing Load

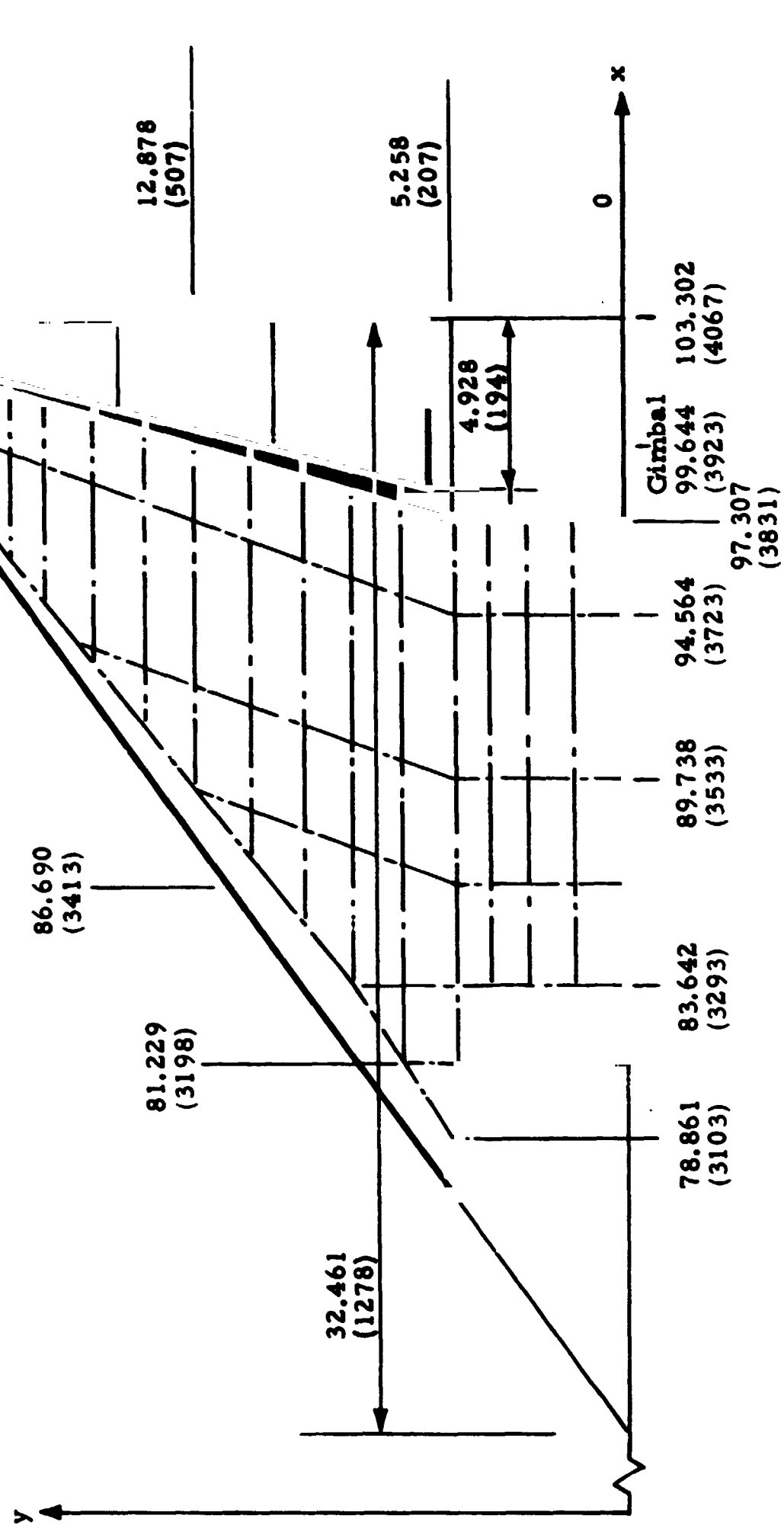

Fig. 4.4-12 - Finite Element Model Boos 'r B-9J Main Wing (Dimensions are in meters. Numbers in parenthesis are dimensions in inches.)

1. Uniform pressure of 16,760 N/m^2 and 23,940 N/m^2 on the wing surface.

2. Hinge moment of 867,700 N-m total (as indicated in report SD 70-403-8, page III-12, by NAR and GP).

The distribution of the hinge moment among ths three elevons was assumed as indicated in the sketch shown in Fig. 4.4-13.

The results for this initial case show that

1. The initial and the minimum gages were very conservative.

2. The structure has enough strength reserve to carry the superimposed hinge moments.

This is expressed in the small slope of the curve in Fig. 4.4-14a for a wing pressure P_o = 16760 N/m^2. The slope is seen to increase slightly in Fig. 4.4-14b for higher wing pressure P_o = 23,940 N/m^2. The computational design details are given in Fig. 4.4-15a, b, c for a uniform pressure P_o = 16,760 N/m^2. Figure 4.4-15a shows the results of a design with zero hinge moment and with a tip deflection of 1.504 m. Figure 4.4-15b shows the results of a design with a nominal hinge moment of 867,720 N-m and a tip deflection of 1.524 m. Figure 4.4-15c shows the results of a design with 1.5 * nominal hinge moment and a tip deflection of 1.532 m. Total computation time for 10 redesign passes is 3.5 min. One design point of the curves requires 21 sec computation time (CPU). Computation can be stopped after four redesign passes due to rapid convergence. Similarly, if it is necessary, the design computation can also be performed for a vertical wing.

Weight penalties for aerodynamic control surface deflections due to variation in hinge moment can be expressed in the following form

$$\Delta W = \frac{\partial W}{\partial H_{m(e)}} \Delta H_{m(e)} + \frac{\partial W}{\partial H_{m(r)}} \Delta H_{m(r)} \qquad (4.4\text{-}12)$$

where $\Delta H_{m(e)} = H_{m(e)} - H_{m(e)_{design}}$,

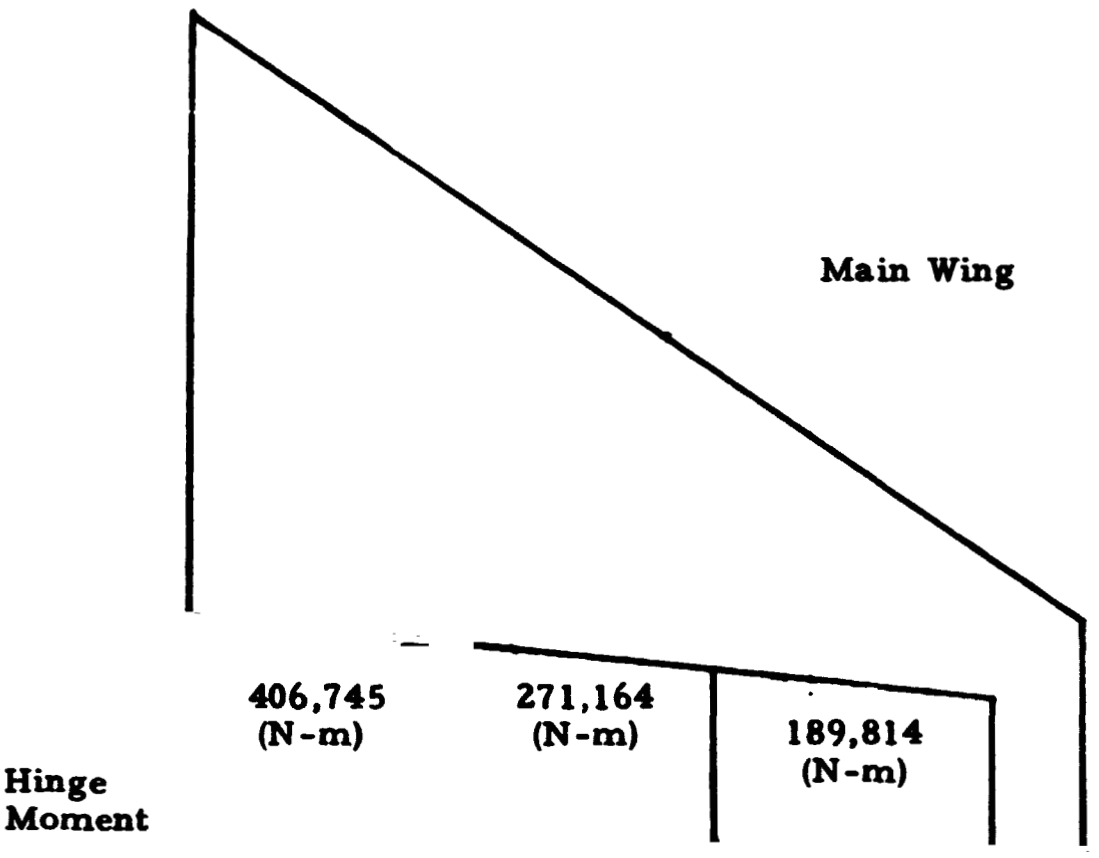

Fig. 4.4-13 - Hinge Moment Distribution Elevon

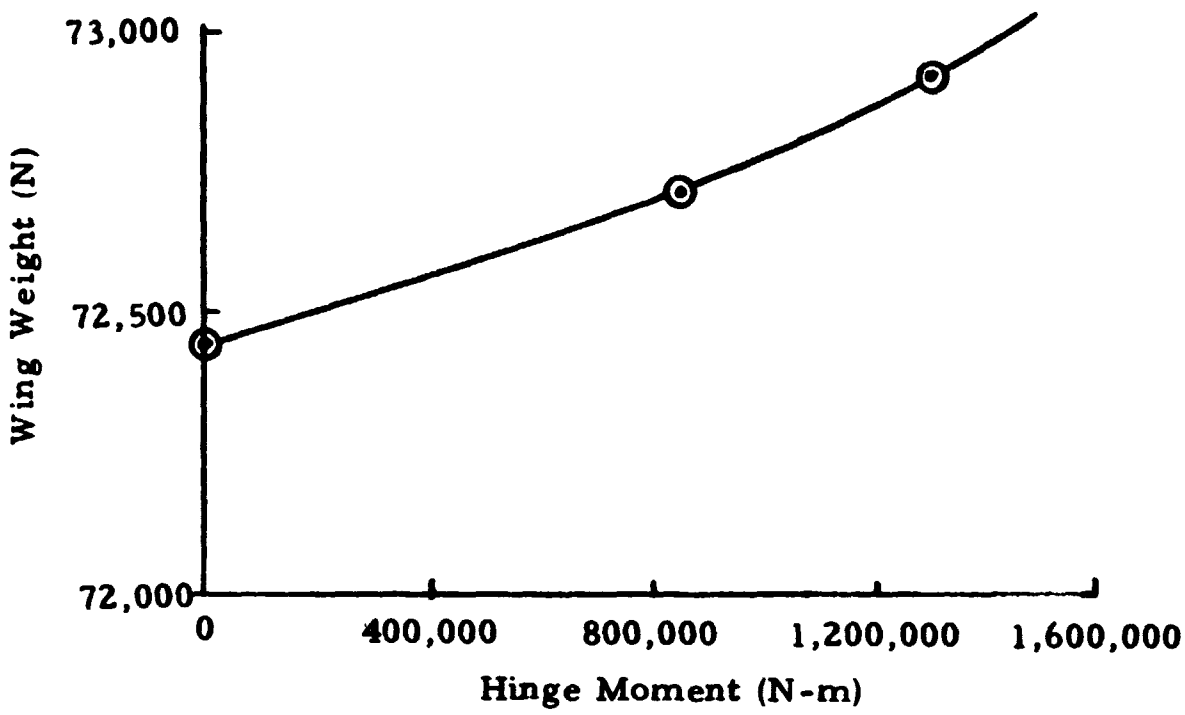

a. Weight Trend for Wing Pressure P_o = 16,700 N/m^2

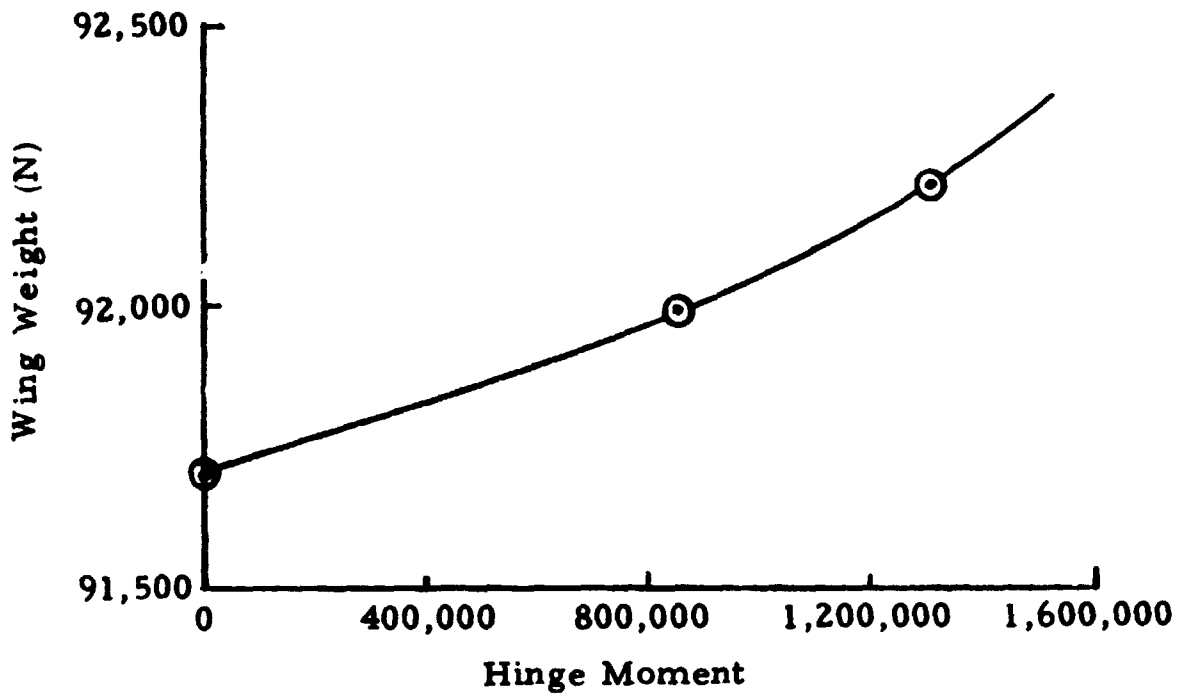

b. Weight Trend for Wing Pressure P_o = 23,940 N/m^2

Fig. 4.4-14 - Weight Trend

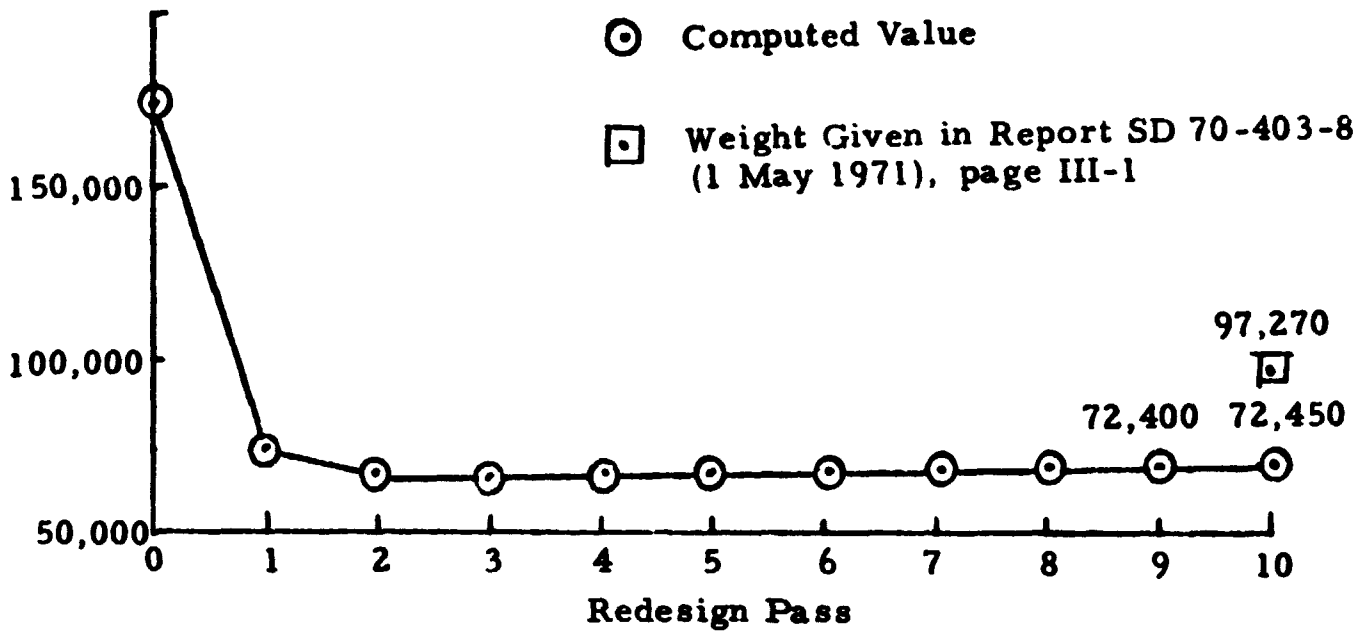

a. Design for Zero Hinge Moment

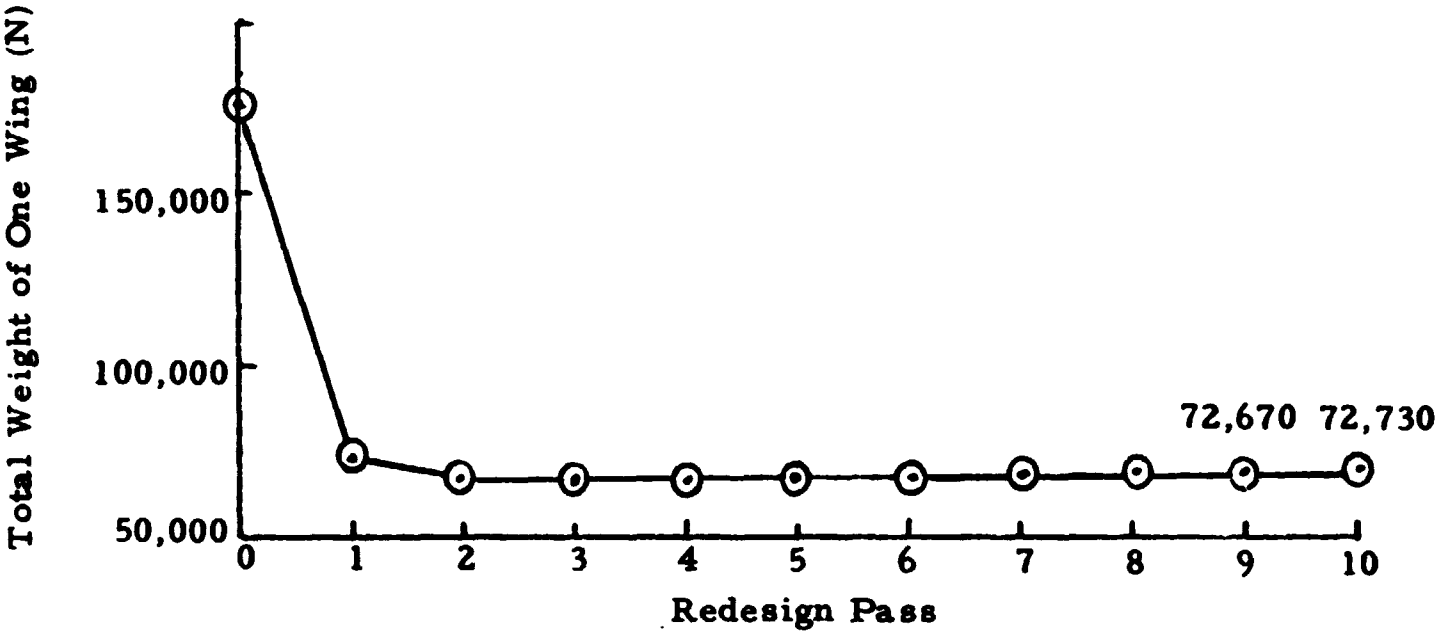

b. Design for Nominal Hinge Moment

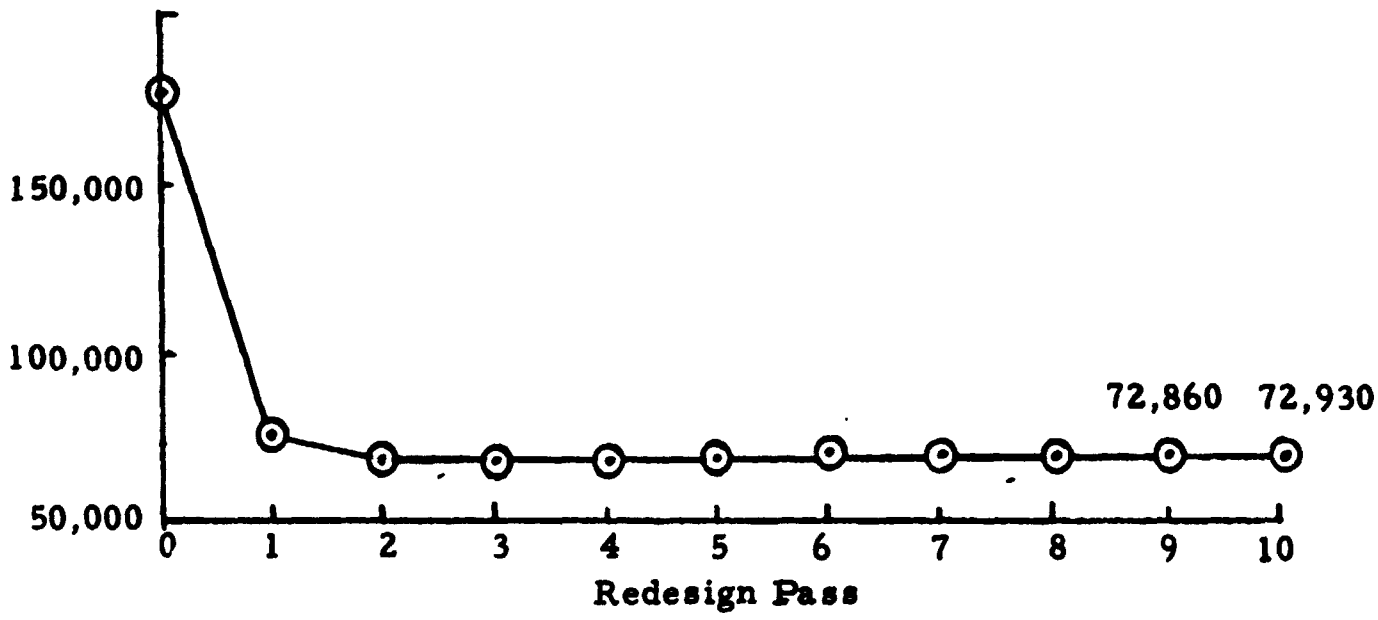

c. Design for 1.5* Nominal Hinge Moment

Fig. 4.4-15 - Computational Details for Fully Stressed Design

$$\Delta H_{m(r)} = H_{m(r)} - H_{m(r)_{design}}$$

for elevons and the rudder, respectively. Equation (4.4-12) can be rewritten as

$$\Delta W = \left[\left(\frac{\partial W}{\partial H_{m(e)}}\right)\left(\frac{\partial H_{m(e)}}{\partial \delta_e}\right)\right]\Delta\delta_e + \left[\left(\frac{\partial W}{\partial H_{m(r)}}\right)\left(\frac{\partial H_{m(r)}}{\partial \delta_r}\right)\right]\Delta\delta_r$$

$$= \left(\frac{\partial W}{\partial \delta_e}\right)_s \Delta\delta_e + \left(\frac{\partial W}{\partial \delta_r}\right)_s \Delta\delta_r \qquad (4.4\text{-}13)$$

The terms in the squared brackets are the structural sensitivities due to variations in control surface deflection from the designed value. $(\partial W/\partial H_{m(e)})$ is the slope of the curves in Fig. 4.4-14 and is a constant equal to 0.000365. $\partial H_{m(e)}/\partial \delta_e$ is a function of time after separation and can be computed from an approximated equation derived in Appendix D. The computed results indicate that

$$\left(\frac{\partial W}{\partial \delta_e}\right)_s \cong 0.025 \left(\frac{\partial W}{\dot{\partial \delta}_e}\right)_h \qquad (4.4\text{-}14)$$

where $(\partial W/\partial \delta_e)_h$ is the hydraulic system weight penalty sensitivity due to variations in control surface deflection rates. It will be evident that structural weight penalty sensitivities due to variations in control surface deflections are very small.

To make the structure more sensitive to superimposed hinge moments, the minimum gage will be reduced. In this case the effect on the overall wing deformation will be checked for excessive tip deflection. When this weight sensitivity has been established, more realistic loading conditions will be formulated. This will require, most importantly, a relation between hinge moment, elevon deflection, Mach number, and angle of attack. Very little of this type of data has become available so far.

4.4.3 Hydraulic System

Weight penalties for aerodynamic control surface deflection rate and deflection angle can be expressed in the following form:

$$\Delta W = \left(\frac{\partial W}{\partial \dot{\delta}}\right)_h \Delta\dot{\delta} + \left(\frac{\partial W}{\partial \delta}\right)_h \Delta\delta$$

where $\Delta\dot{\delta} = \dot{\delta} - \dot{\delta}_{design}$ and $\Delta\delta = \delta - \delta_{design}$. The partials in the above equation are functions of the aerodynamic control surface structural and hydraulic system weight which is determined by the control surface design hinge moment, deflection rate, and deflection angle travel. In order to evaluate these partials, a weight analysis of the GDC/B-9U booster hydraulic system has been performed for a range of hinge moment, deflection rate and deflection angle travel capabilities.

The weights of the various components of the hydraulic system were determined utilizing empirical formulas and data available. A block diagram showing the relationship between the hydraulic system component weights and the system parameters is presented in Fig. 4.4-16.

The bulk of the hydraulic system weight is contained in the actuators, transmission lines, pumps, fluid, and accessory power unit (APU) weights. The remaining weight of valves, filters, switches, and accumulators is a small portion of the total system weight and may be neglected for the determination of aerodynamic surface control related weight penalties.

The design criteria used in determining the various hydraulic system component weights are presented as follows:

1. O_2/H_2 APU is used.
2. Hydraulic system pressure is 3000 psi.
3. The hydraulic system is designed to actuate the control surface at the design hinge moment deflection rate with a load pressure differential of 67% of system total pressure.
4. Elevon and rudder maximum rates are not coincident. Hydraulic maximum power requirements are determined by the elevons.
5. Hydraulic actuators are sized by hinge moment requirements and not stiffness.

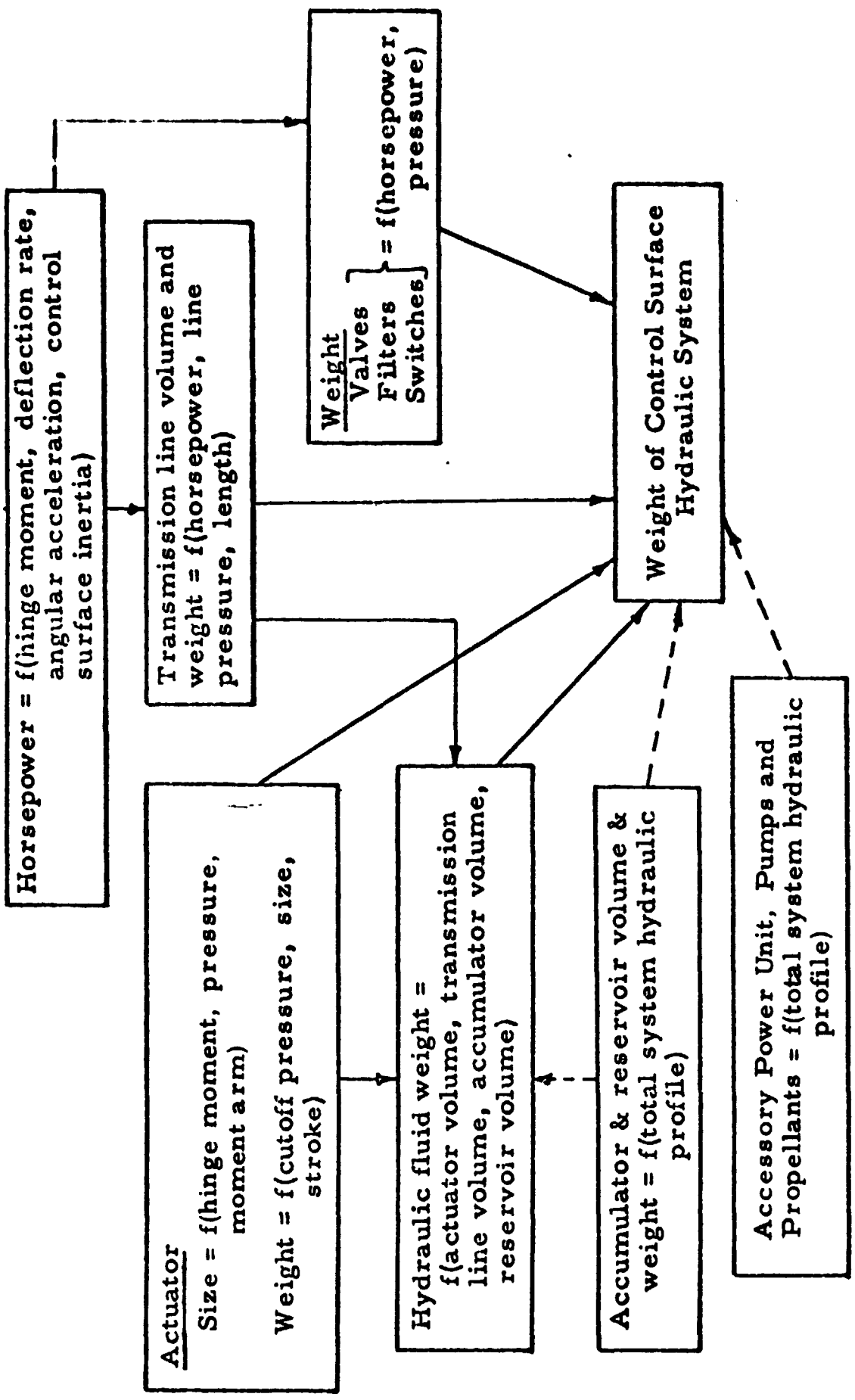

Fig. 4.4-16 - Analysis of Aerodynamic Surface Control Related Weight Penalties

6. APU weights are multiplied by 1.6 to include ducting and installation weights.

7. The servo motor in each servo actuator group requires two horsepower.

8. Typical elevon actuator moment arm of 15 inches and rudder actuator moment arm of 12 inches are assumed.

9. Fuel and oxidizer weights are multiplied by 1.5 to include a hydraulic pump operation at reduced output and reduced efficiencies.

The detailed analysis of hydraulic system component weights is given in Appendix C. As an example, results of this analysis for one hinge moment, deflection rate and deflection angle combination are presented in Table 4.4-1.

Table 4.4-1

AERODYNAMIC CONTROL SURFACE CONTRIBUTION TO HYDRAULIC SYSTEM WEIGHT

Control Surface	Hinge Moment (N-m)	Deflection Rate (deg/sec)	Line Weight (N*)	APU and Pump Wt. (N)	Propellant Weight (N)	Actuator Weight (N)	Total Weight (N)
Elevon	2.03×10^6	20	9960	20,450	5790	24,400	60,600
Rudder	1.08×10^5	30	1342	**	360	1,310	3,012

*Includes weight of fittings, brackets, fluid, and reservoir.
**System APU and pumps are sized by elevons.

The aerodynamic control surface hydraulic system weight penalty partials derived from this weight analysis are presented in Figs. 4.4-17 and 4.4-18.

The payload penalty partials are based on hydraulic system component weights that were determined from the available design information. In

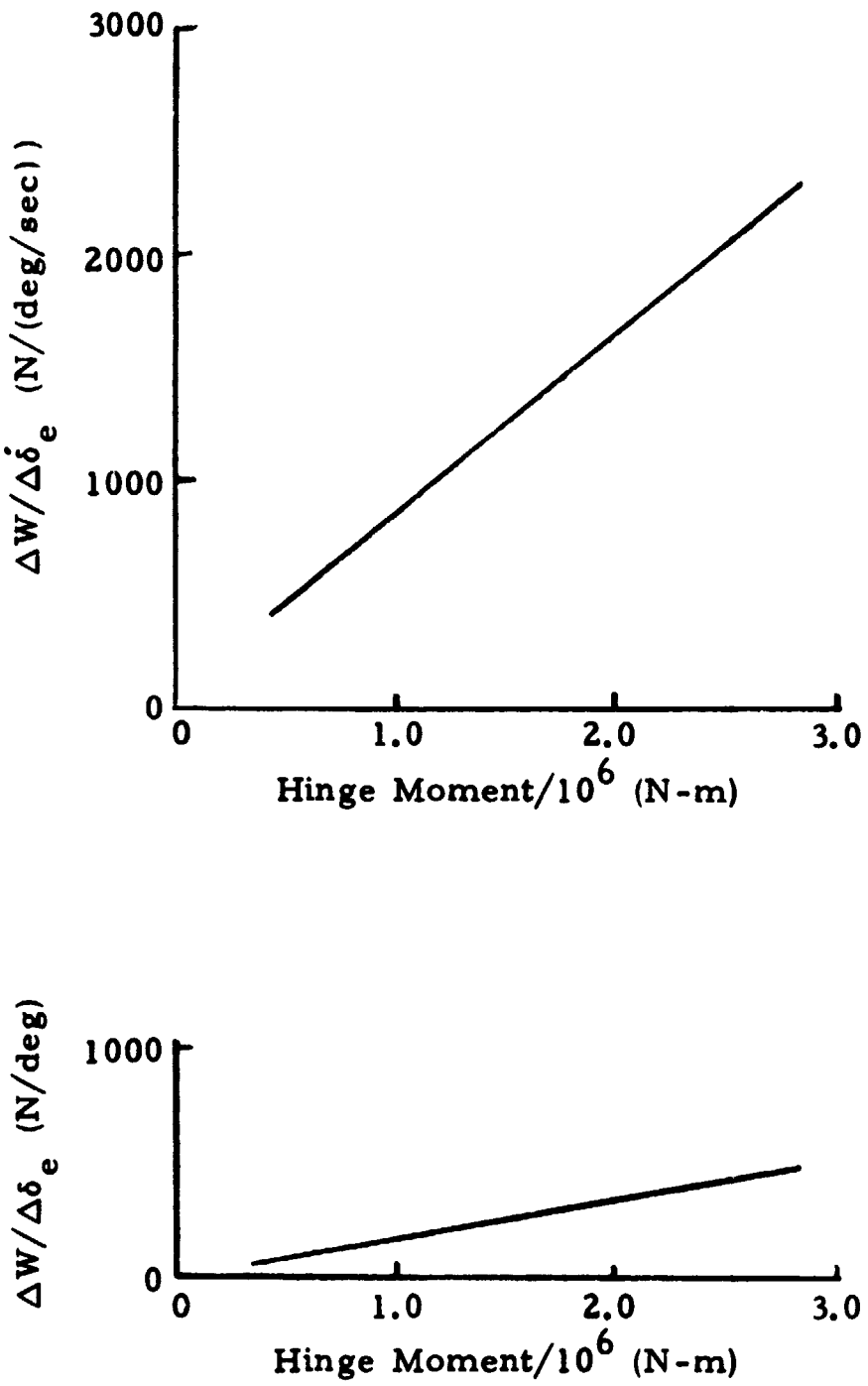

Fig. 4.4-17 - Rate of Change of Control System Weight with Elevon Deflection Rate and Deflection Angle Tra vel

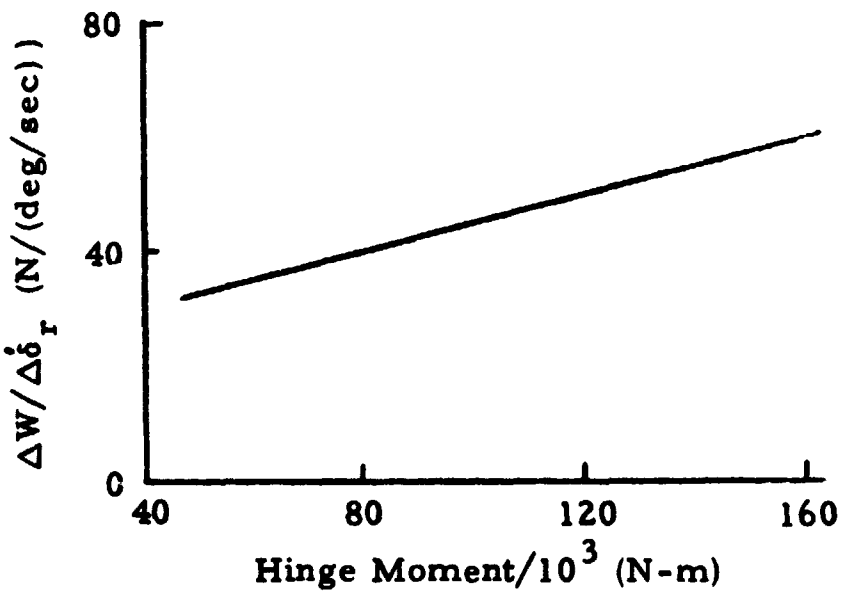

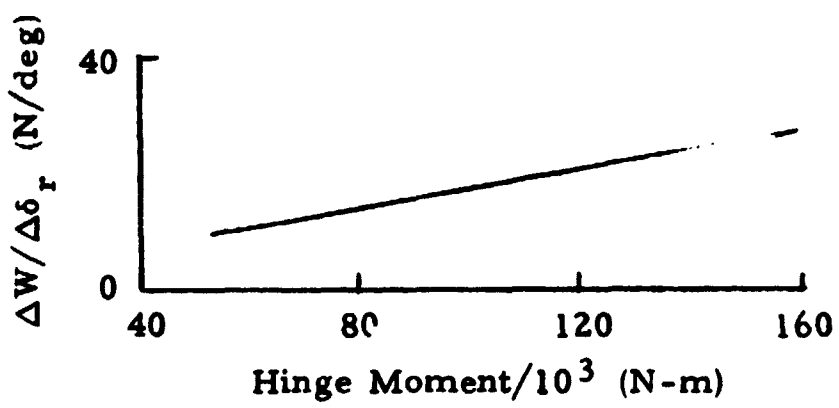

Fig. 4.4-18 - Rate of Change of Control System Weight with Rudder Deflection Rate and Deflection Angle Travel

some instances it was necessary to make weight estimates based on general assumptions and limited information. The payload penalty partials should be reviewed as the space shuttle booster hydraulic system becomes better defined and more design information becomes available.

The elevon and rudder hydraulic system weight penalties, given in Figs. 4.4-17 and 4.4-18, can be expressed in terms of hinge moments as:

$$\Delta W = (100.0 + 7.80 * 10^{-4} H_{m(e)}) \Delta\dot{\delta}_e \qquad (4.4\text{-}15)$$

$$\Delta W = (-10.0 + 1.7 * 10^{-4} H_{m(e)}) \Delta\delta_e \qquad (4.4\text{-}16)$$

$$\Delta W = (20.0 + 2.5 * 10^{-4} H_{m(r)}) \Delta\dot{\delta}_r \qquad (4.4\text{-}17)$$

and

$$\Delta W = (2.4 + 1.6 \times 10^{-4} H_{m(r)}) \Delta\delta_r \qquad (4.4\text{-}18)$$

where ΔW is the variation of hydraulic system weight, $H_{m(e)}$ is the elevon hinge moment, and $H_{m(r)}$ is the rudder hinge moment.

$$\Delta\dot{\delta}_e = \dot{\delta}_e - \dot{\delta}_{e_{design}}, \quad \Delta\delta_e = \delta_e - \delta_{e_{design}}$$

$$\Delta\dot{\delta}_r = \dot{\delta}_r - \dot{\delta}_{r_{design}}, \quad \Delta\delta_r = \delta_r - \delta_{r_{design}}$$

Since the hinge moment coefficients and dynamic pressure along a given reentry trajectory are functions of time, the hinge moments are functions of time and control surface deflection. For a given design control surface deflection and deflection rate, the sensitivities of the hydraulic system weight can be computed from the above equations. However, since the hinge moment coefficient data are not available at present, a method to approximate the hinge moment coefficients by using available aerodynamic force coefficient data is obtained and is given in Appendix C. The completed hydraulic system weight sensitivity data from 200 to 395 sec after separation are shown in Fig. 4.4-19. Evidently the hydraulic system weight is very sensitive to

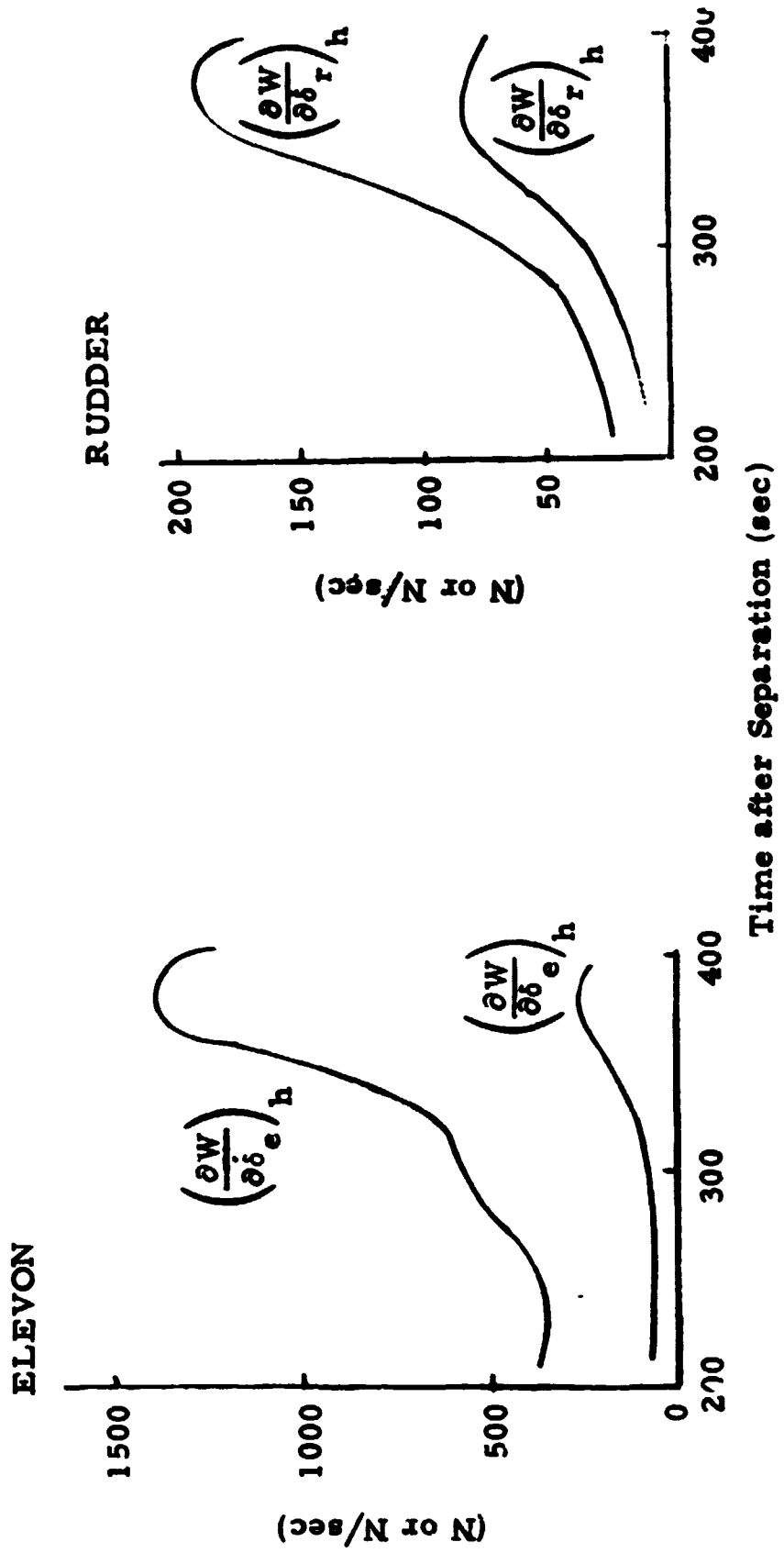

Fig. 4.4-19 - Sensitivity of Elevon and Rudder Weight Penalties Related to Hydraulic System

variations in the elevon deflection rate from 340 to 395 sec after separation (i.e., from Mach 1.3 to Mach 0.75 range of flight). The hydraulic system weight is sensitive to changes in rudder deflection rate and elevon deflection from 340 to 395 sec after separation.

4.4.4 Identification of Control System Weight Penalties

Based on the control system related weight penalties and sensitivity analysis, the following results are obtained:

1. Thermal protection system weight is insensitive to APS firing and nonfiring related weight.

2. Thermal protection system weight is not too sensitive to maximum aerodynamic control surface deflection angle.

3. Structural weight associated with aerodynamic control is not too sensitive to maximum aerodynamic control surface deflection angle.

4. Hydraulic system component weight is very sensitive to maximum deflection rate from Mach 1.3 to 0.75.

5. Hydraulic system component weight is sensitive to maximum deflection angle from Mach 1.3 to 0.75.

From this analysis, then, it can be easily seen that the hydraulic system weight penalties associated with the elevon deflection, deflection rate, and rudder deflection rate are of prime importance. These weight penalties can be incorporated into the control system optimization study by using them as components of a performance index

$$J_{\substack{\text{hydraulic}\\ \text{weight}}} = \left(\frac{\partial W}{\partial \delta_e}\right)_h \Delta\delta_e + \left(\frac{\partial W}{\partial \delta_r}\right)_h \Delta\delta_r + \left(\frac{\partial W}{\partial \delta_e}\right)_h \Delta\delta_e$$

Since $(\partial W/\partial \delta_e)_h$, $(\partial W/\partial \delta_r)_h$, and $(\partial W/\partial \delta_e)_h$ are important only from 340 sec to 395 sec after separation, the computation of this element of performance index can be limited to the above mentioned time interval.

Section 5
HYBRID SIMULATION AND OPTIMIZATION TECHNIQUES

5.1 PROBLEM AREAS IN HYBRID COMPUTATION STUDIES

Several years of analog and hybrid computation at Lockheed's Huntsville Research & Engineering Center have pointed up a number of software prob'em areas that are really cneountered throughout the entire simulation industry. Some of these are:

- Multiple human handling of data.
- High engineering involvement during the programming phase.
- Several single purpose digital programs are developed for each study.
- Setup time is very long.
- Verification of results is usually very difficult.

Several of the computer manufacturers have software packages that help to ease some of these difficulties but none cover all of them. Lockheed has developed a total hybrid softw..e concept (Fig. 5.1-1) under this contract which is "user oriented" to largely eliminate all of them. It is a collection of very general digital programs that "talk to each other" by punched cards or magnetic tape. In this way they automatically process data for equations of motion and prepare the hybrid computer for production simulation runs. Raw data are input to a set of preprocessor programs (see Fig. 5.1-1) which manipulates it and produces a "run tape" which permits very rapid setup and checkout of a hybrid problem. A digital simulation is employed in the pre-processing to estimate parameter ranges and to produce a dynamic check case. It is later used to verify the ultimate results of the hybrid simulation.

All off-line programs are modularized and written in Fortran V for ease of modification and understanding by an engineer. On-line programs

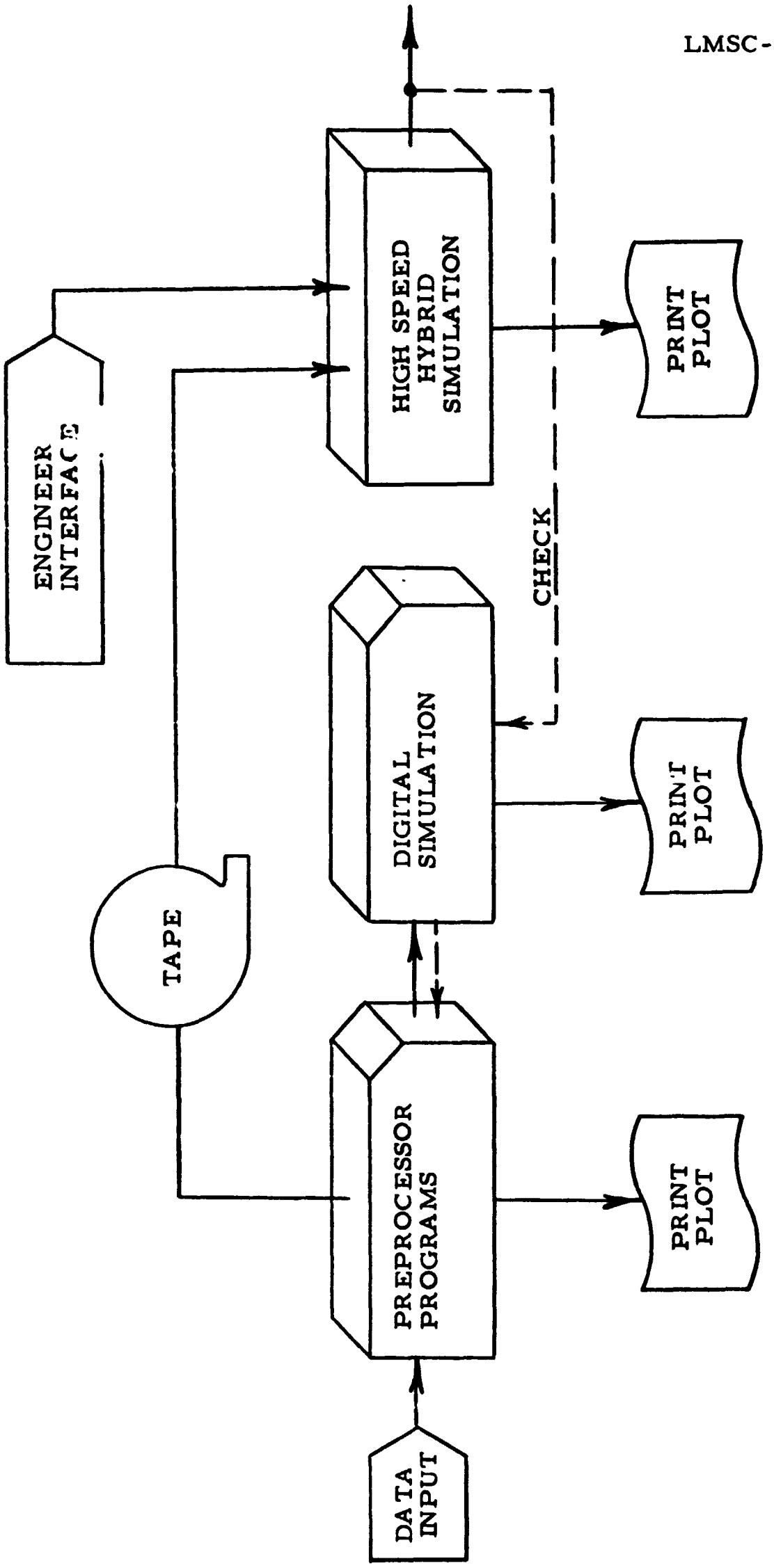

Fig. 5.1-1 - Total Hybrid Software Concept

are written in Assembly language to save computer core space and to assure the shortest possible digital cycle time.

5.2 STABILITY STUDIES AND PARAMETER RANGE ESTIMATION

The initial "guesses" for the control system gains were synthesized by the program described in Appendix G. These time varying gains were fed into the digital simulation program (Appendix H) along with a forcing function to generate the expected ranges of the program parameters. A diagram of this portion of the software is given in Fig. 5.2-1.

5.3 RUN TAPE GENERATION

The single most important item that permits very rapid and automated digital and analog setup and checkout as well as rapid changeover from one vehicle or trajectory to another is the Run Tape. A diagram of the run tape generation is given in Fig. 5.3-1. The data preprocessor (see Appendix E) reduces the raw data and produces a set of punched cards which contain tables of the time varying coefficients of the equations of motion. These coefficients, the expected parameter ranges and other miscellaneous data are then input to the scaling and table setup program. It should be noted that the programmer must produce his own wiring diagrams. Then, one set of data that must be input is a list of amplifier and integrator gains, both input and feedback. Using these data, all the parameters are scaled in magnitude. All inputs to integrators are from pots. This fact, plus an input time scale, are used then to further scale the equations in time. By this method the problem may be time scaled over a continuous range from less than real time to approximately 1000 times real time.

After scaling the equations, each coefficient is scanned for its maximum magnitude. Then these values are scaled to reflect the magnitude and time scaling. The equations of motion are then printed out with these values. At this time the wiring may be changed to increase or decrease amplifier or integrator gains to properly size the coefficients. It is a simple matter

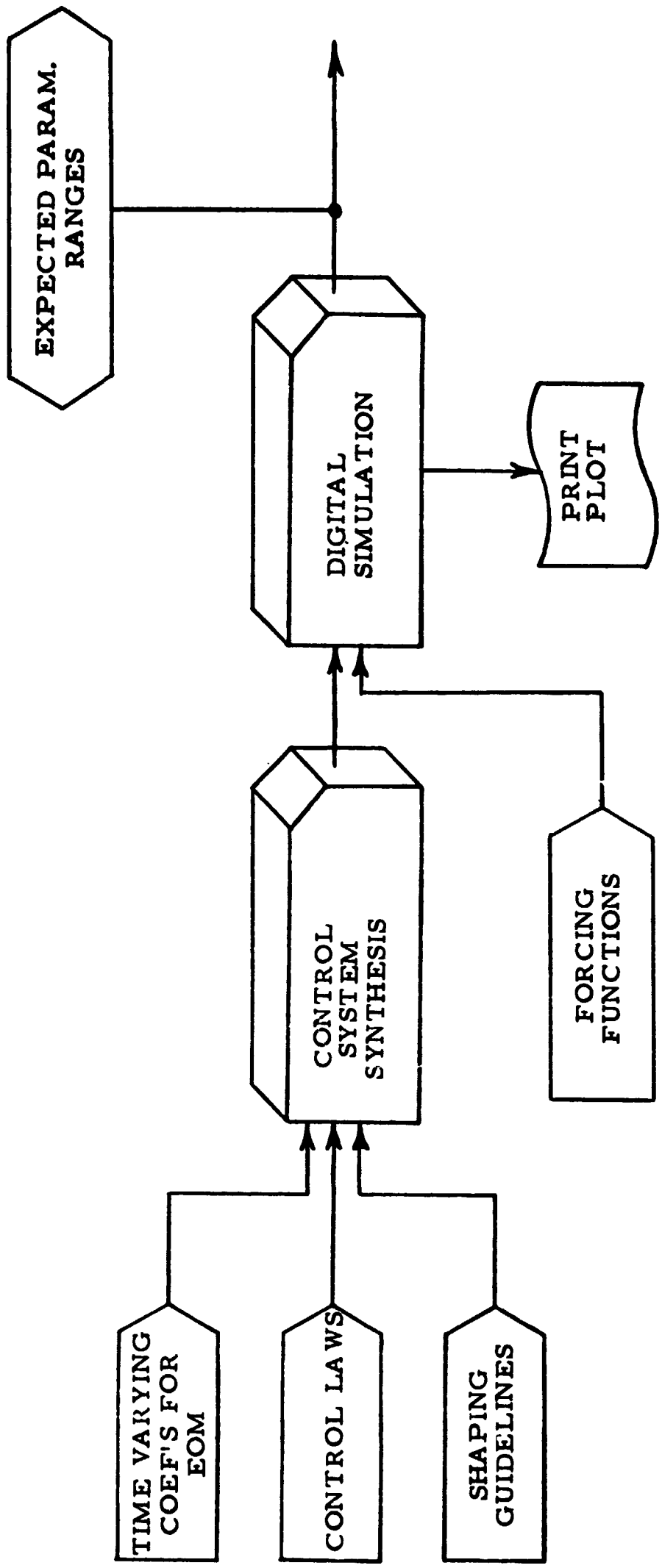

Fig. 5.2-1 - Stability Studies and Parameter Range Estimation

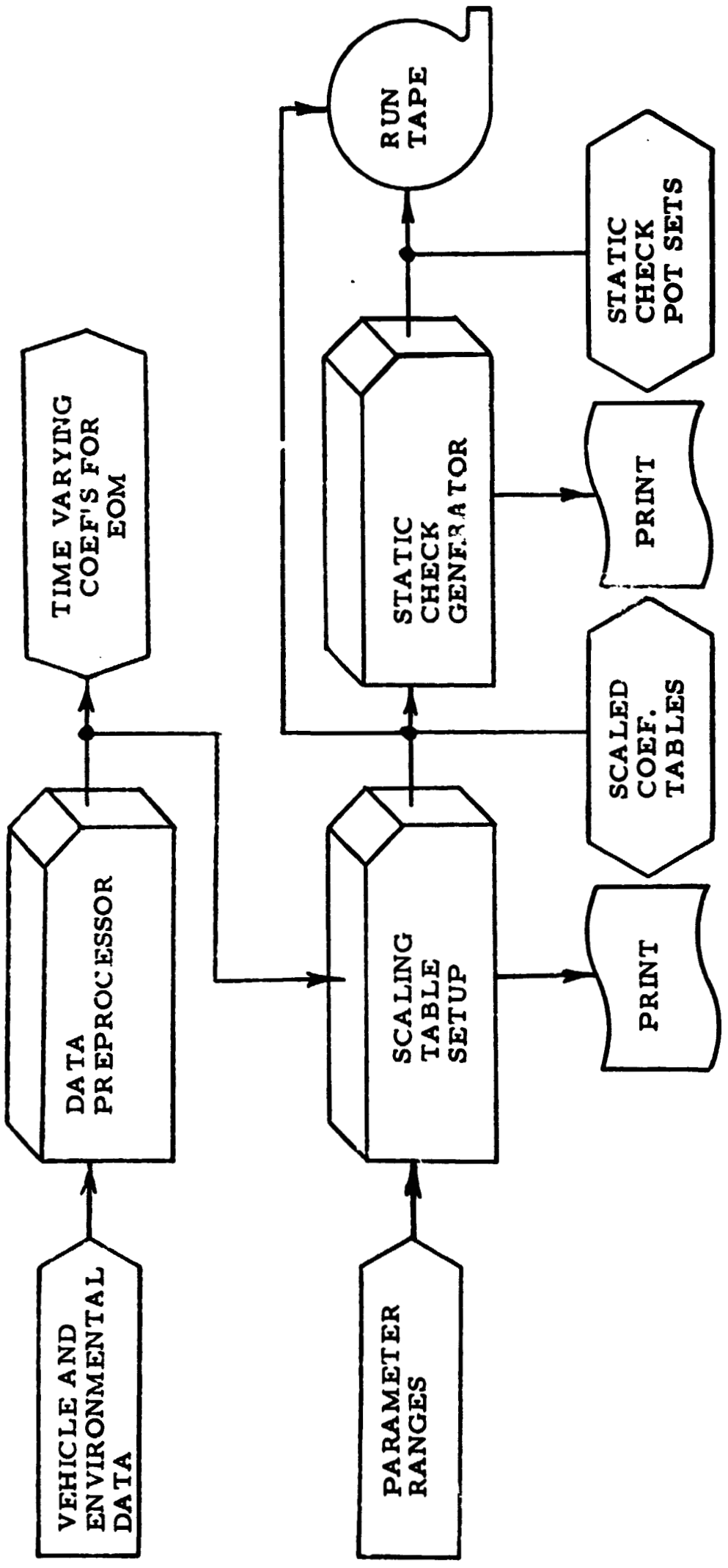

Fig. 5.3-1 - Run Tape Generation

to change a few gains on the circuit board and these can be reflected by data input card to the scaling and table setup deck. After any needed gain changes are incorporated, the process of magnitude and time scaling is repeated, the coefficients scanned for maximum magnitudes again, etc. If the printout indicates the problem is scaled reasonably, then the total tables for all coefficients are scaled. New tables are produced for these coefficients using straight line interpolation, if necessary, to produce a value of each coefficient for each "data update point." These tables are then output to the run tape.

The term "data update point" mentioned in the last paragraph brings up the subject of Lockheed's "Fast Data Transfer" method. This fast data transfer is one of the most significant feature of this software concept and is largely responsible for the rapid setup and checkout of the hybrid computer. Figure 5.3-2 illustrates this operation. The time varying coefficient K_{21}, the aileron control effectiveness coefficient described in Section 4.1, is shown as it is produced by the data preprocessor. Below it is a plot of this same coefficient as it is used by the analog side of the hybrid simulation. Instead of using diode function generators (DFG) to provide time varying coefficients, tables are stored for each coefficient in the digital memory and these data are periodically transferred to the analog computer by the digital-to-analog converters (DAC).

The coefficients, as utilized in the simulation then, are held constant over an update interval and changed by step input at the interrupt time points as shown in the blowup in Fig. 5.3-2.

The frequency with which these data are brought over must be selected so that the dynamics of the system are not excited by the induced noise from the stairstep form of the coefficients. The shape of the time varying coefficient curves also must be faithfully reproduced. For the incident study a one-second (real time) update interval was selected. The simulation was carried out at 1000 times real time so that the updates were made every millisecond. The digital cycle time was short enough that the real time

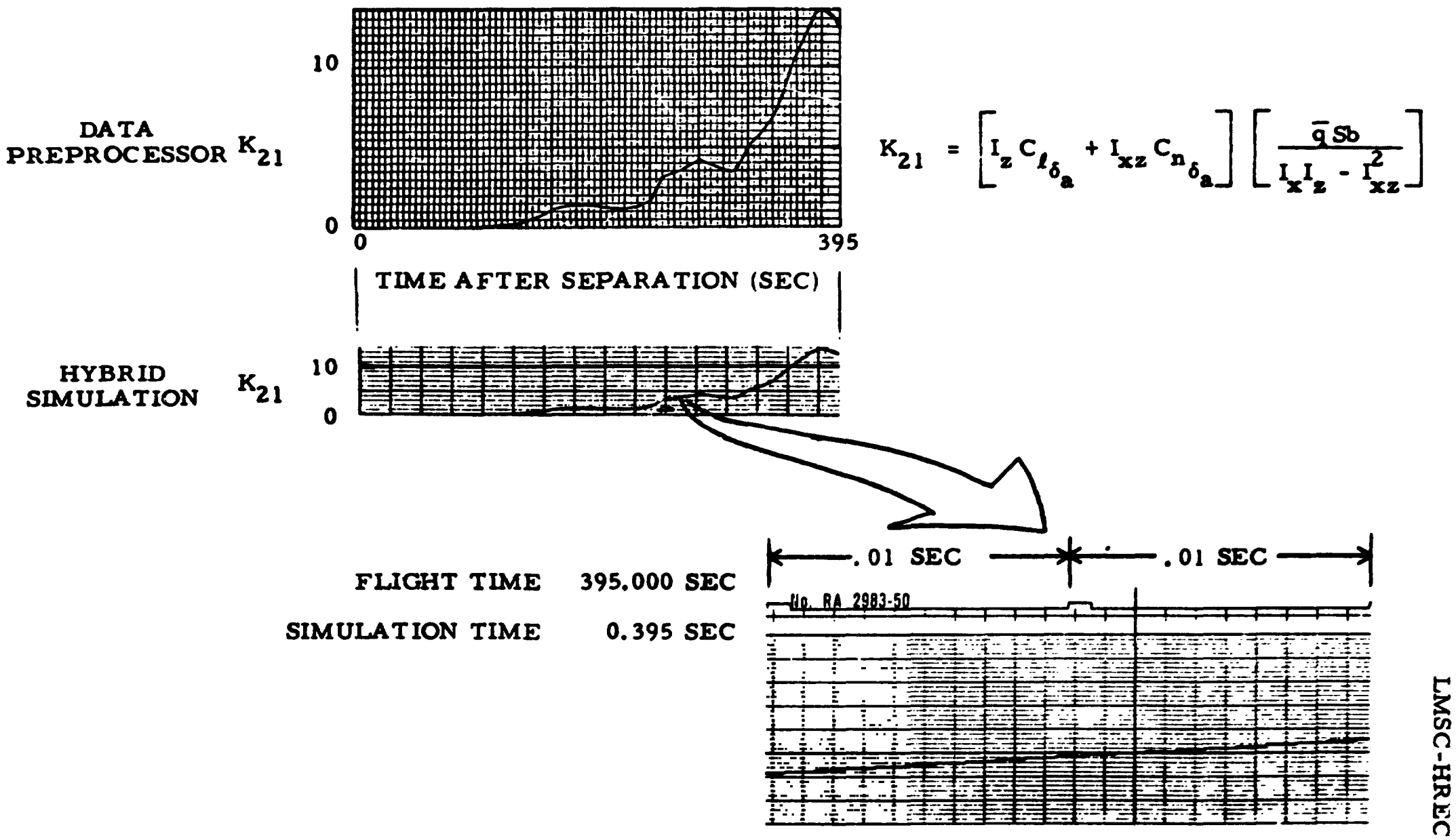

Fig. 5.3-2 - Fast Data Transfer Comparison

tasks could be completed in less than one millisecond so that all coefficients could be brought over to the analog in parallel without putting the analog into "hold." As shown in Fig. 5.3-2, the total 395 second trajectory was simulated in 0.355 seconds of computation time.

A foolproof priority interrupt system is built into the digital side of the hybrid program so that if digital cycle time exceeds the update interval, the problem is put into hold and the computer operator is notified by the on-line printer. At this point the problem may be scaled down in time by whatever increment required to allow the digital cycle time to again be less than the update interval simulation period.

Referring again to Fig. 5.3-1, the static check preprocessor deck sets up and prints out a complete list of the analog pot settings. At this point any wiring changes may be made to bring all pots to a reasonable setting, if required. The pot settings are then recalculated and printed out. Following this a complete static check is generated based on the gains, pot settings and initial conditions (IC) that have been determined. The output of all printout components are listed for possible overloads or other undesirable conditions and the IC's may here be altered to regenerate a more reasonable static check. The pot settings and the static check are then both output to the run tape.

At this point the user has in one piece of equipment all he needs to completely setup and checkout his analog boards in a very rapid and efficient manner. Assuming no wiring changes are required, several run tapes may be generated for various vehicles and trajectories, each available for rapid setup and checkout interchangeability.

5.4 HYBRID COMPUTER SETUP

Assumming no hardware malfunctions, the hybrid computer may be setup and checked out within five minutes, using the run tape as input. Figure 5.4-1 illustrates this process. The digital computer is first loaded

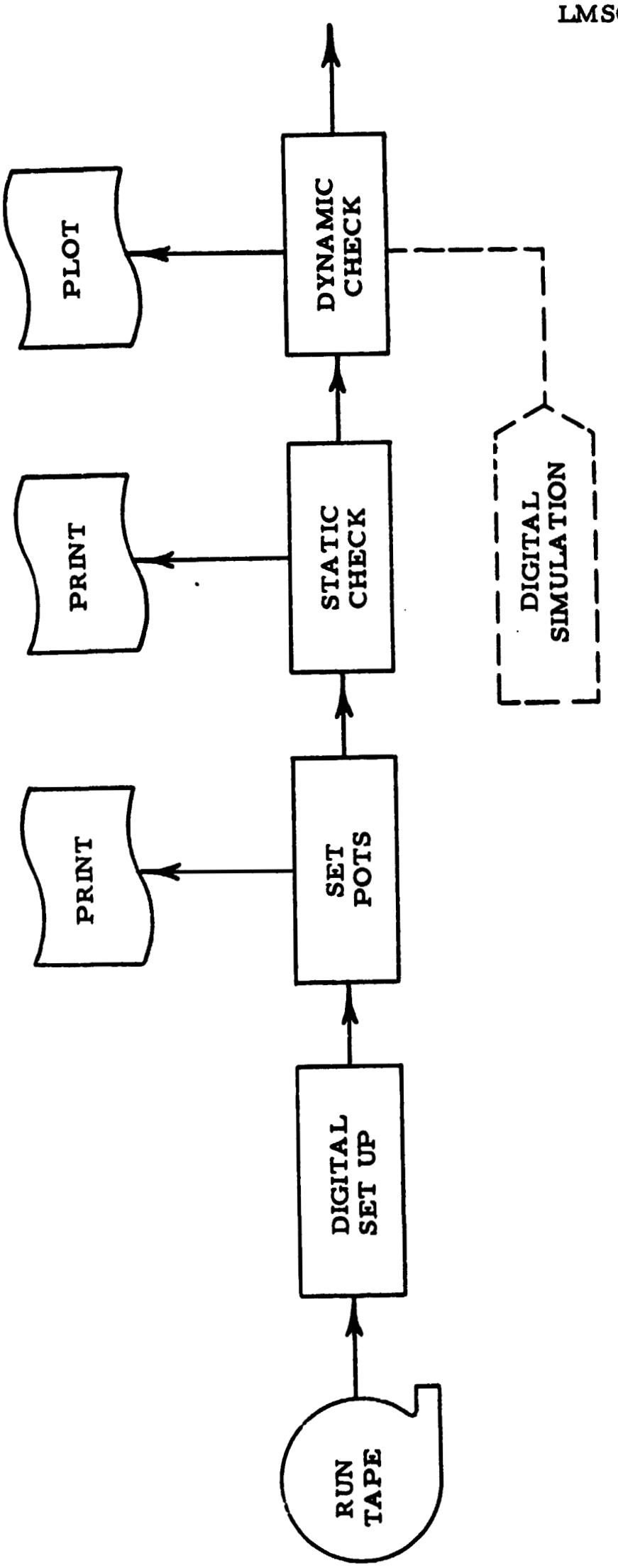

Fig. 5.4-1 - Hybrid Computer Setup

with the data tables, static and dynamic check instructions, and the digital program for the real time process. The pots are automatically set and a list of their settings is printed out. All pots out of a prespecified tolerance are flagged on the printout so that they may be corrected. A static check follows automatically, again with a printout flagging out of tolerance analog components to simplify troubleshooting. Initial conditions are then set and a dynamic check run is made. This dynamic check should match a plot of the digital simulation output. The computer, both analog and digital sides, are now ready for engineering simulation studies.

5.5 HYBRID SIMULATION AND VERIFICATION

Figure 5.5-1 illustrates the hybrid simulation and verification process. An engineer has several parameters that will enable him to "engineer" his desired solution. Several trajectories may be simulated very rapidly. Then one or several parameters or parameter ranges may be changed by card input as judged by the engineer and the runs repeated.

When the ultimate design or designs are produced, the conditions producing them (disturbances, gains, etc.) are input to the digital dynamic simulation (Appendix H) and the resulting output is used for verifying the hybrid results. Very close correlation between the two programs has been experienced for all simulations that have been compared.

5.6 SUMMARY OF TOTAL HYBRID SOFTWARE CONCEPT FEATURES

Considerable effort has been expended under this contract in the development of the very general set of programs comprising the total hybrid software package. This unusual amount of work was performed at this time to allow future studies to be much more efficiently handled to save manhours and computer time. A list of the salient feature of this set of programs is as follows:

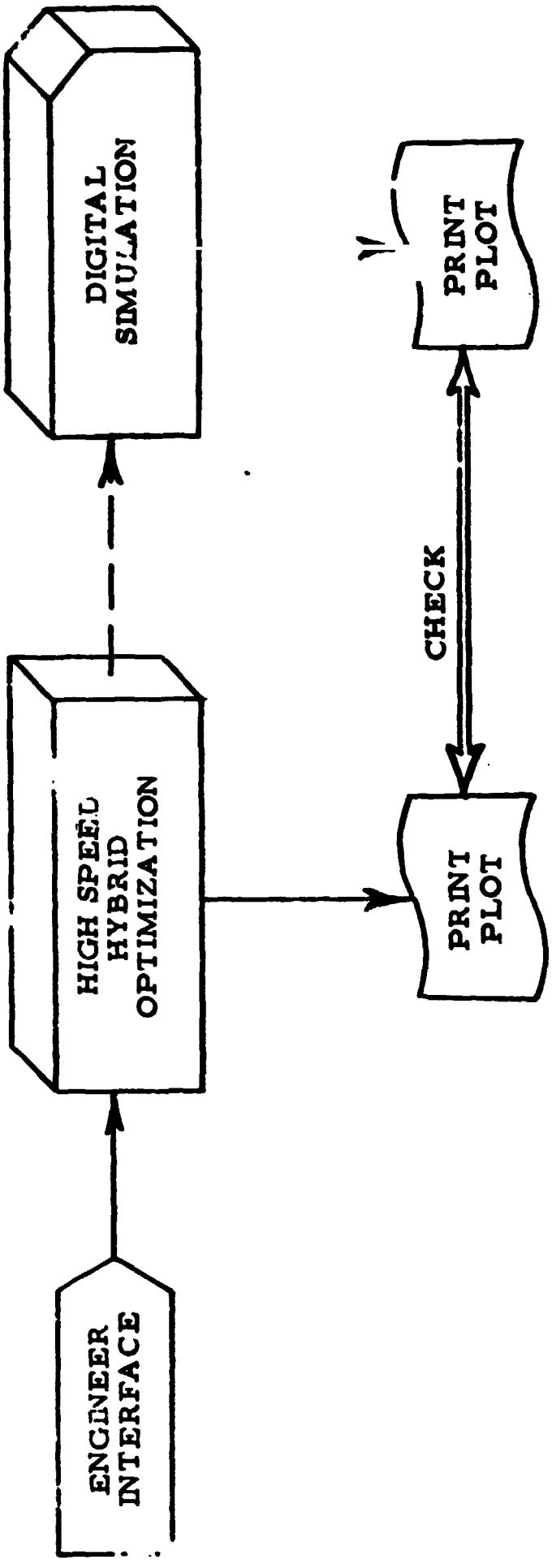

Fig. 5.5-1 - Hybrid Simulation and Verification

- Rapid, automated problem and computer setup
- Flexible on-line engineering interface
- Minimum human off-line involvement
- Independence of vehicle configuration and trajectory
- High speed operation
- Verification capability
- Maximum flexibility for modification

It is felt that this unusual effort has already paid off in efficiency and will become of even greater importance in future studies.

Section 6
OPTIMIZATION RESULTS

This section presents the results obtained during the optimization of blending ratios for both the Ascent and Reentry Phases of the shuttle.

6.1 ASCENT

The objective during this study was to maximize payload injected into orbit by optimizing the blending ratios of the aerodynamic control surfaces of the shuttle subject to the possible occurrence of two adverse winds during ascent. The blending ratios k_e, k_r, k_a, k_c were to be optimal time-varying schedules which blend the optimal schedules of $a_{0\theta}$, $a_{1\theta}$, $a_{0\psi}$, $a_{1\psi}$, $b_{0\psi}$, $a_{0\phi}$, $a_{1\phi}$ obtained from Contract NAS8-25578.

To achieve the above objective it was necessary to formulate performance criteria which are functions of all control-related payload penalties. Reference 1 details the formulation of the payload sensitivities associated with peak structural loads, peak engine gimbal angles, peak hinge moments and peak trajectory errors. These formulations combined with the virtually free choice of selecting performance criteria, the realism of rapid analog dynamic simulations and the powerful gradient minimization technique assure an ideal design tool to achieve the above objective.

The following performance index comprises the major payload penalties which depend upon flight control system performance:

$$J' = \sum_{i=1}^{6} \frac{\partial P}{\partial R_i} \left| R_{i_{max}} - R_{i_o} \right| + \sum_{j=1}^{3} \frac{\partial P}{\partial \delta_j} \left| \delta_{j_{max}} - \delta_{j_o} \right|$$

$$+ \sum_{m=1}^{3} \left[\frac{\partial P}{\partial x_m} x_{m_{max}} + \frac{\partial P}{\partial v_m} v_{m_{max}} \right]$$

$$+ \frac{\partial P}{\partial H_M} \left| H_{M_{max}} \right|$$

where

P = payload penalty or decrease

R_i = forces at the booster-orbiter interface

δ_i = main booster engine gimbal angles for roll, pitch, yaw control including δ_{trim}

x_m = deviations from reference trajectory in x, y, z direction

v_m = velocity errors with respect to reference trajectory in x, y, z direction

H_M = hinge moment due to aerodynamic surface deflection

The subscript "o" denotes design values corresponding to the nominal payload capability.

The design goal of maximum payload can then be achieved by minimization of this payload penalty functional J'.

In order to avoid excessive angular rates by the vehicle in response to gust-type wind disturbances, an additional cost functional was formulated:

$$J'' = \frac{1}{T} \int_{t}^{t+T} \left[\left| \frac{\dot{\phi}}{\dot{\phi}_{ME}} \right| + q_{\dot{\theta}} \left| \frac{\dot{\theta}}{\dot{\theta}_{ME}} \right| + q_{\dot{\psi}} \left| \frac{\dot{\psi}}{\dot{\psi}_{ME}} \right| \right] dt$$

where $\dot{\phi}$, $\dot{\theta}$, $\dot{\psi}$, are the roll, pitch, and yaw rates, respectively, and the subscript "ME" denotes maximum expected values. $q_{\dot{\theta}}$ and $q_{\dot{\psi}}$ are weighting coefficients reflecting the design constraints imposed on the various vehicle rates. J" should be kept small to assure smooth flying qualities. The criteria (J) and (J") can be readily combined into a single performance criterion

$$J = J' + q\,J'' \longrightarrow \min.$$

which makes possible the minimization of all payload penalties while a weighted flying quality criterion qJ" is simultaneously satisfied.

All three weighting factors (q, $q_{\dot{\theta}}$, $q_{\dot{\psi}}$) are directly related to well-established design guidelines concerning admissible angular rates and therefore easy to adjust after a small number of trial optimizations.

This is a major advantage over quadratic form J functionals, where a large number of weighting factors with little or no physical meaning must be selected by trial and error.

Figure 6.1-1 shows pitch plane results for α_{w_A} where this J function for maximizing payload was implemented. The structural loads at the booster/orbiter rear attachment points were found to have the strongest impact on structural weight requirements and associated payload penalties. The dynamic simulation generates time histories of all major terms in this payload-related performance measure. Peak values $R_{i_{max}}$, $\delta_{j_{max}}$, . . . , are sampled during simulation and trajsferred to the performance analyzer at the end of each run. The interface geometry and notations are shown in Fig. 3.3-1. The major payload penalty term

$$\frac{\partial P}{\partial R_r}\left(R_{r_{max}} - R_{r_o}\right) \triangleq \Delta P_R$$

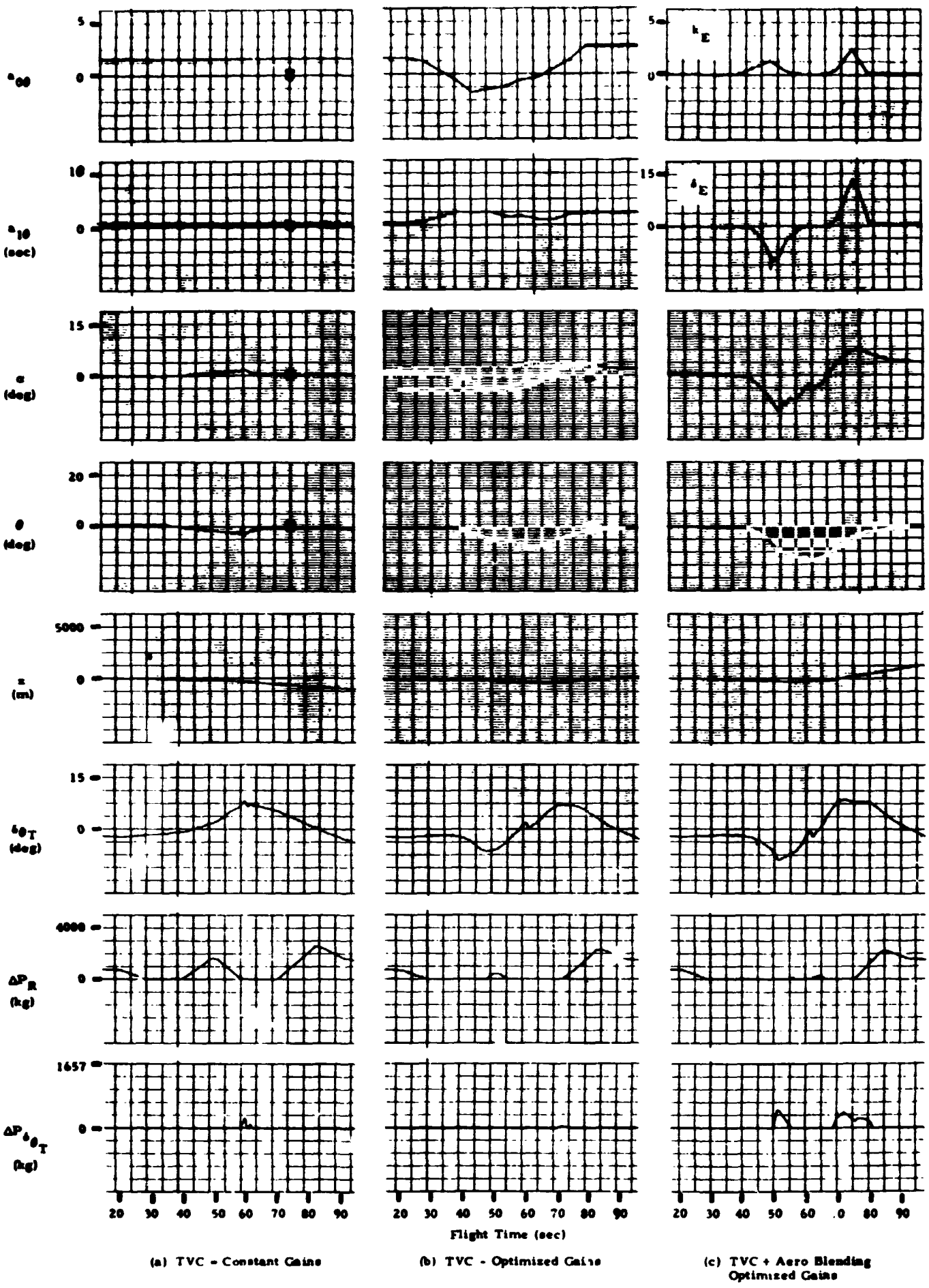

Fig. [illegible] Shuttle Ascent (MDAC-20) Pitch Plane Response to α_{w_A} (headwind) for (a) Constant TVC Gain Controller, (b) Optimized TVC Gain [illegible] and (c) Optimized Blending of Optimal TVC Gain [illegible]

is associated with the resultant force R_r,

$$R_r = \sqrt{(R_{2z} + R_{3z})^2 + R_{4y}^2}$$

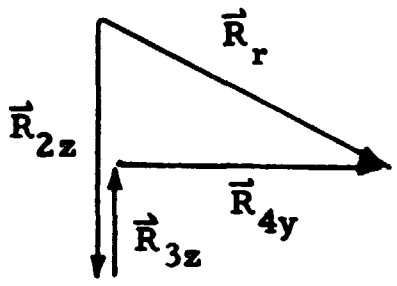

which is the vector sum of $\vec{R}_{2z}$, $\vec{R}_{3z}$ and $\vec{R}_{4y}$. In the absence of sidewinds and lateral motion (yaw, roll, sideslip), $\vec{R}_r$ acts in the z-direction of the vehicle. In general, however, $\vec{R}_r$ acts slightly out of the pitch plane. The nominal design value for this load was assumed to be

$$\left|R_{r_o}\right| = 4 \times 10^5 \text{ N}$$

Only loads in excess of R_{r_o} were therefore accounted for in determining associated payload penalties.

The second largest effect on payload is due to maximum engine gimbal angle requirements for pitch plane deflections as required for pitch and roll corrections. It was assumed that the vehicle design was based on

$$\left|\delta_{\theta_{T_o}}\right| \leq 7^\circ$$

gimbal angle requirement. Engine deflections in excess of 7 degrees were therefore accounted for in determining the payload penalty

$$\frac{\partial P}{\partial \delta_{\theta_T}} \left(\left|\delta_{\theta_{T_{max}}}\right| - \left|\delta_{\theta_{T_o}}\right| \right) \equiv \Delta P_{\delta_\theta}$$

Time histories of these two major payload penalties (ΔP_R and $\Delta P_{\delta_{\theta_T}}$) are included in all recordings of vehicle response.

Typical results are shown in Fig. 6.1-1, which shows responses to the headwind profile $\alpha_{w_A}(t)$ for constant gain pitch plane controller, optimal pitch plane controller, and optimized elevon blending ratio k_e. Figure 6.1-2 shows some responses to headwind profile $\alpha_{w_B}(t)$. The optimal schedule of $a_{0\theta}(t)$ and $a_{1\theta}(t)$ (the pitch plane control feedback gains) were obtained under another contract (NAS8-25578). The optimal schedules are shown in the top two strips of Figs. 6.1-1b and 6.1-2b. These optimal schedules were programmed on diode function generators and the blending ratio $k_e(t)$ was set up to be optimized. The shuttle response to the resulting optimal $k_e(t)$ schedules is shown in Fig. 6.1-1c and 6.1-2c for winds $\alpha_{w_A}(t)$ and $\alpha_{w_B}(t)$, respectively. Figures 6.1-1a and 6.1-2a are included to show the vehicle response using constant gain controllers of $a_{0\theta} = 1.5$, $a_{1\theta} = 0.5$ sec, and $k_e = 0$.

Dramatic reductions in payload penalty due to structural interface loads at the orbiter's two rear attachment points were achieved (1200 kg). The elevons assisted the gimbaled engine in allowing the vehicle to rotate more freely into the wind. These trends are easily seen when examining the response of θ and α. One adverse effect was noted, it being an increase in magnitude of gimbal angle δ_{θ_T} when elevons are blended in. A brief analysis seems to indicate this may be caused by rapid transients of the engine being superimposed on the nominal response. The engines are able to react much faster than the larger elevon surface. Removal of the $\dot{\theta}$ feedback term into the blending ratio $K_e(t)$ would probably improve the δ_{θ_T} response. More study in this area would be needed to determine the reasons for these initial adverse effects of elevon blending on engine gimbaling.

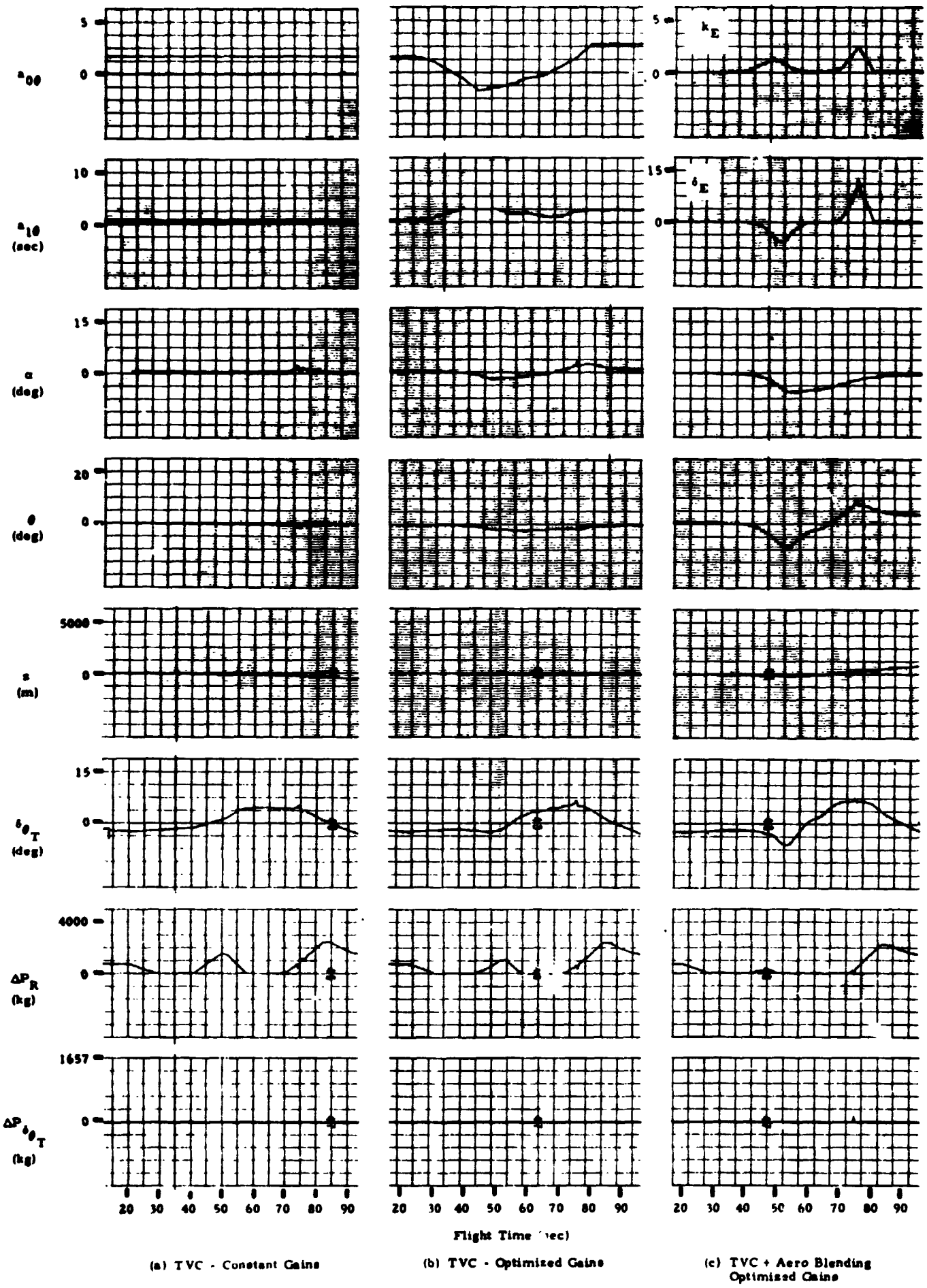

Fig. 6.1-2 - Shuttle Ascent (MDAC-20) Pitch Plane Response to α_{w_B} (headwind) for (a) Constant TVC Gain Controller, (b) Optimized TVC Gain Controller and (c) Optimized Blending of Optimal TVC Gain Controller

6.2 REENTRY

The primary objective of this study was to perform optimization studies on the problems related to the booster reentry. These problems consist of the optimization of the control system performance, the minimization of APS fuel consumption and control system related weights and the optimum blending of APS and aerodynamic control.

The optimization of the control system performance requires the formulation of performance criteria which are functions of the closed-loop control system error. For this study, mean-square error is chosen. Since a mean-square error performance function, $J_{(c)}$, penalizes large errors much more severely than small ones, the resulting system reacts quickly to large errors but resonates for an extended period with relatively small errors. Then,

$$J_{(c)} = a_1 \int_0^{395} (\alpha_E^2 + \phi_{XE}^2 + \phi_{ZE}^2)\, dt + a_2 \int_0^{395} (\dot{p}^2 + \dot{q}^2 + \dot{r}^2)$$

where a_1 and a_2 are weighting parameters which are used to adjust flying quality.

Total APS propellant consumption for the control of a reentry vehicle can be expressed as

$$W_{(p)} = \int_0^{395} \left[\dot{W}_{x(p)} + \dot{W}_{y(p)} + \dot{W}_{z(p)}\right]$$

$$= \frac{1}{I_{sp}} \int_0^{395} \left[\frac{I_{sp}\,\overline{X}\,\dot{W}_{x(p)}}{\overline{X}} + \frac{I_{sp}\,\overline{Y}\,\dot{W}_{y(p)}}{\overline{Y}} + \frac{I_{sp}\,\overline{Z}\,\dot{W}_{z(p)}}{\overline{Z}}\right] dt$$

$$= \frac{1}{I_{sp}} \int_0^{395} \left[\frac{1}{\bar{X}} \left| M_{x(p)} \right| + \frac{1}{\bar{Y}} \left| M_{y(p)} \right| + \frac{1}{\bar{Z}} \left| M_{z(p)} \right| \right] dt$$

where $W_{x(p)}$, $W_{y(p)}$ and $W_{z(p)}$ are the total propellant expenditures for the control of roll, pitch and yaw axes, respectively; $\bar{X}$, $\bar{Y}$ and $\bar{Z}$ are the moment arms of the APS thrusters for producing roll, pitch and yaw control moments, respectively; and I_{sp} is the specific impulse. The performance function for APS propellant consumption can be written as

$$J_{(p)} = \int_0^{395} \left[b_1 \left| M_{x(p)} \right| + b_2 \left| M_{y(p)} \right| + b_3 \left| M_{z(p)} \right| \right] dt$$

where b_1, b_2 and b_3 are APS control quality weighting parameters. They are used to prevent over emphasis of fuel consumption resulting in determination of control quality about an axis. This might otherwise happen because the integral of the absolute value of control moment penalizes the axis requiring large control moments more heavily than the axis requiring smaller control moments.

The control system related weight minimization depends on the flight control system performance. The performance function based on the detailed discussion given in Section 4.4 is comprised of the following important terms

$$J_{(w)} = \left(\frac{\partial W}{\partial \dot{\delta}_e} \right)_h \Delta \dot{\delta}_e + \left(\frac{\partial W}{\partial \dot{\delta}_r} \right) \Delta \dot{\delta}_r + \left(\frac{\partial W}{\partial \delta_e} \right) \Delta \delta_e + \left(\frac{\partial W}{\partial I_{(p)}} \right) \Delta I_{(p)} + \left(\frac{\partial W}{\partial T_{(p)}} \right) \Delta T_{(p)}$$

where $(\partial W / \partial I_{(p)}) = 0.0035 \text{ sec}^{-1}$, which shows the adjustment in system weight due to the variation in total impulse $I_{(p)}$. Also, $(\partial W / \partial T_{(p)}) \cong 0.15$, which shows the adjustment in system weight due to the variation in total system thrust $T_{(p)}$. The changes in total impulse and total system thrust are given as

$$\Delta I_{(p)} = I_{(p)} - \left[I_{(p)}\right]_{design} \quad \text{and} \quad \Delta T_{(p)} = T_{(p)} - \left[T_{(p)}\right]_{design}$$

The above mentioned performance functions can be used separately or jointly as

$$J = c_1 J_{(c)} + c_2 J_{(p)} + c_3 J_{(w)}$$

where c_1, c_2 and c_3 are design goal weighting parameters which are used to adjust design emphasis and are related to well-established design guidelines.

In order to evaluate the phase plane design of APS control, the raw and fine control law designed in Appendix E for single-level torque is used in the hybrid simulation of a hypothetical vehicle with $I_x = 2.007 \times 10^6$, $I_y = 1.33 * 10^7$, $I_z = 1.41 \times 10^7$, and $I_{xz} = 0.2 \times 10^6$. The rotational equations of motion (Eqs. (4.1-4), (4.1-5) and (4.1-6)) are used in the simulation. Figure 6.2-1 shows time histories of the vehicle angular accelerations and angular rates for 5 deg attitude errors. In this figure, $\hat{P}$, $\hat{Q}$, and $\hat{R}$ are directly related to APS firings. The APS is seen firing continuously to decelerate the vehicle and to reduce error and increase the absolute value of the error until the attitude error and error rate satisfy the switching criterion. Then the APS reverses firing to accelerate the vehicle and reduce vehicle attitude error and the absolute value of error rate until they are eliminated.

If the dynamics of the fuel control valve, etc., are approximated by a simple time delay, the optimum switching laws used in the above simulation is no longer optimum and limit cycle behavior occurs. The modified control laws, which compensates for the time delay in the control logic, are used in the simulation. Figure 6.2-2 shows the time history of the vehicle angular accelerations and angular rates with and without the control law modification for 10 deg attitude errors. It is seen that marked savings in fuel and improved dynamic response are achieved by using the modified attitude control laws.

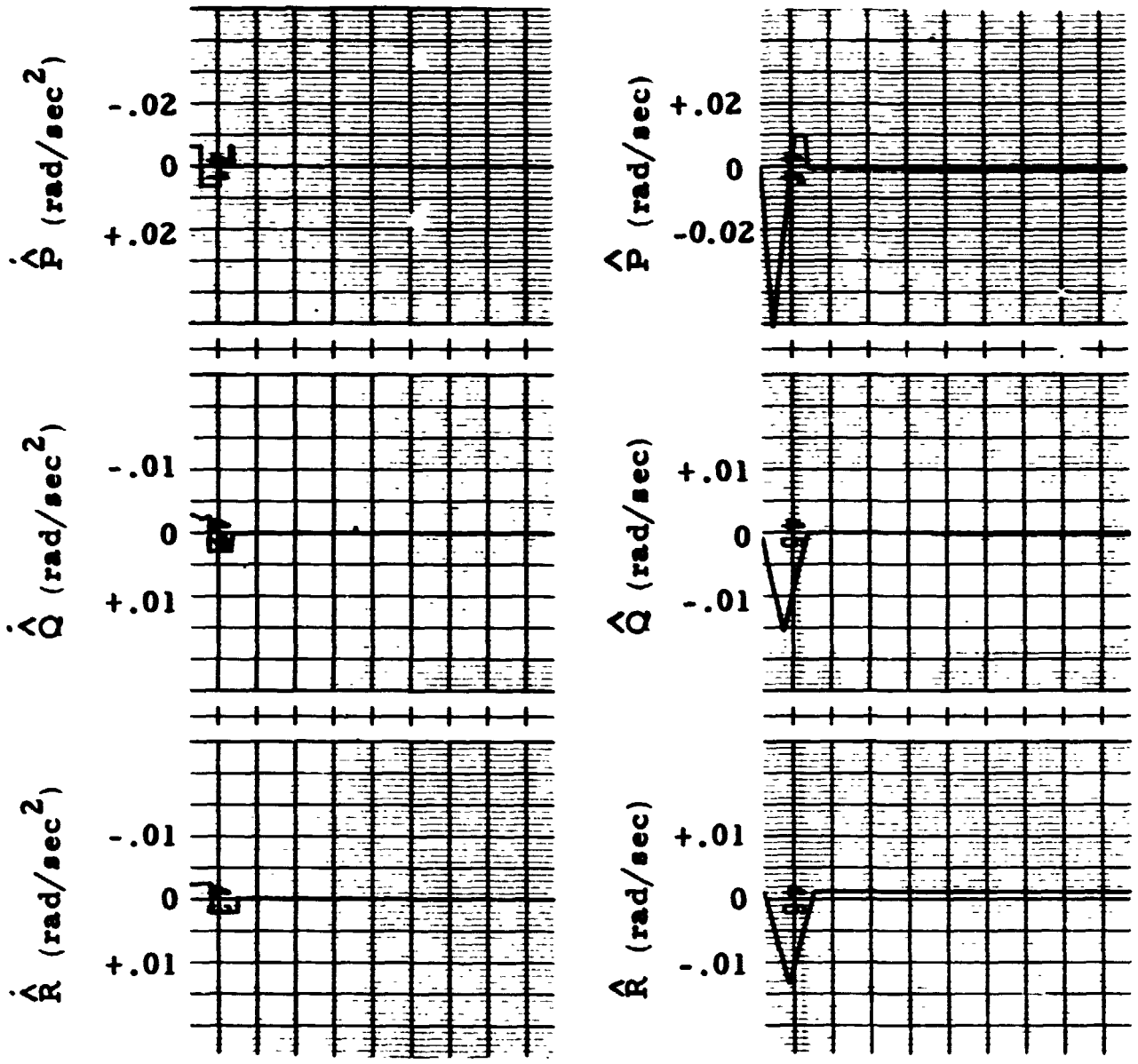

Fig. 6.2-1 - Vehicle Angular Accelerations and Angular Velocities Versus Time During the Elimination of 5 deg Attitude Errors

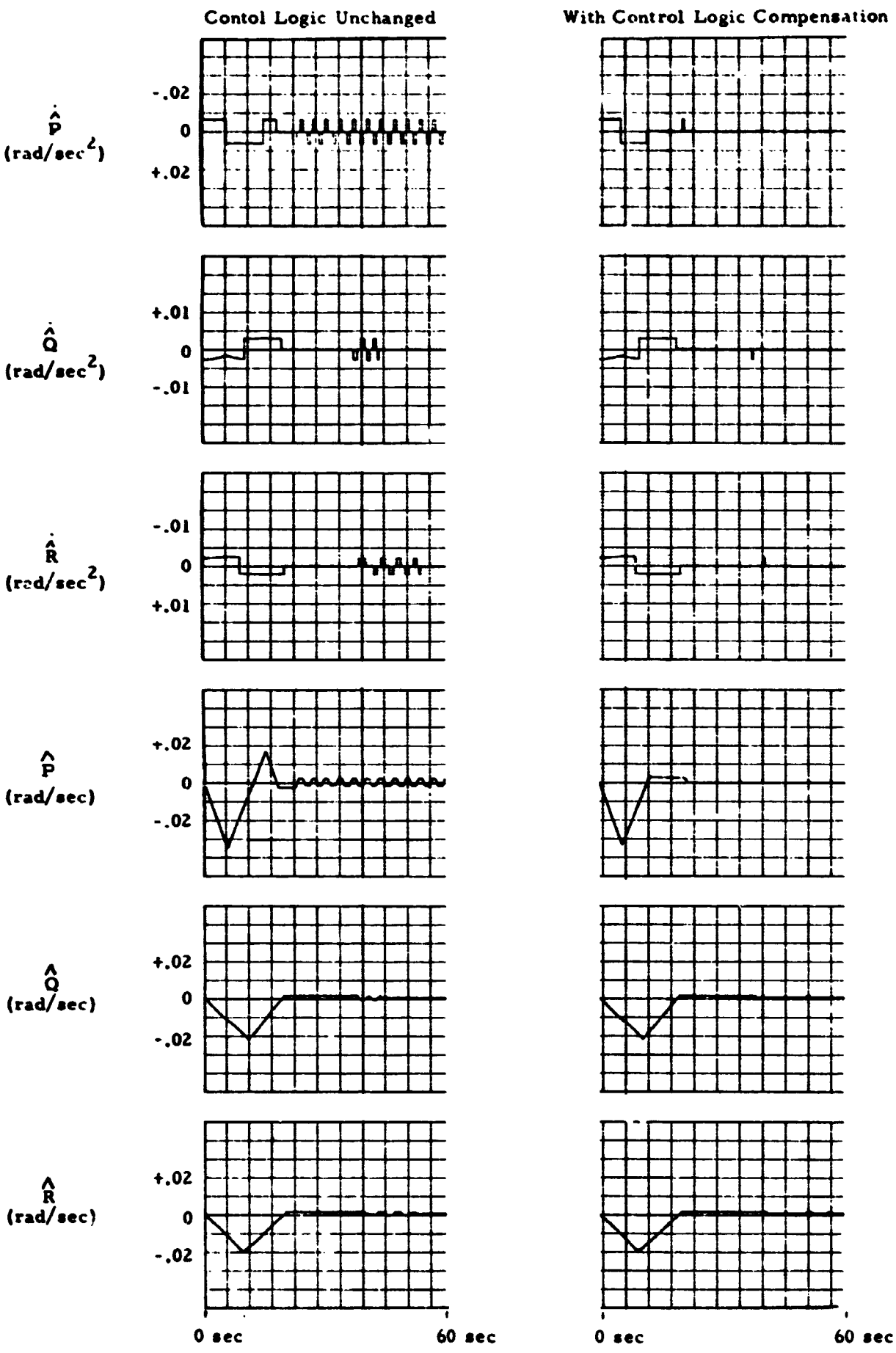

Fig. 6.2-2 - Vehicle Angular Accelerations and Angular Velocities Versus Time During the Elimination of 10 deg Attitude Errors and with a 0.14 Second System Time Delay

A preliminary hybrid computer optimization of the GDC/B-9U APS has been achieved. The optimization parameters are the position and velocity feedback gains for roll, pitch and yaw thrusters. The objective of the optimization was to minimize the fuel consumption and optimize the control system performance. The performance function chosen is

$$J = c_1 J_{(c)} + c_2 J_{(f)}$$

The blending strategy for this initial optimization was to leave the elevons on all the time, to turn rudder and aileron on at 220 sec, and to turn the APS off at 240 sec. The chosen pitch and bank angle commands are alternating pulses at 20 sec intervals. These pulses have a pulse height of 1 deg and pulse width of 10 sec. The staircase switching lines of the APS controllers are approximated by straight lines as shown in Fig. 4.2-2.

The aero control laws used during APS optimization are listed below

$$\delta_{ac} = K_{VIA}\beta + K_{DA}(\phi_x - \phi_{xc}) - K_{RA}p$$

$$\delta_{ec} = -K_{\alpha}(\alpha - \alpha_c) - K_q q$$

$$\delta_{rc} = K_{VIR}\beta - K_{DR}(\phi_z - \phi_{zc}) - K_{RR}r$$

where all aero control gains are time scheduled and are obtained from the control gain synthesis program. Figure 6.2-3a shows the aero controller block diagram. The APS control laws for the simulation are of the attitude error and rate form

$$E_x = K_{1x}(\phi_x - \phi_{xc}) + K_{2x}p$$

$$E_y = K_{1y}(\alpha - \alpha_c) + K_{2y}q$$

$$E_z = K_{1z}(\phi_z - \phi_{zc}) + K_{2z}r$$

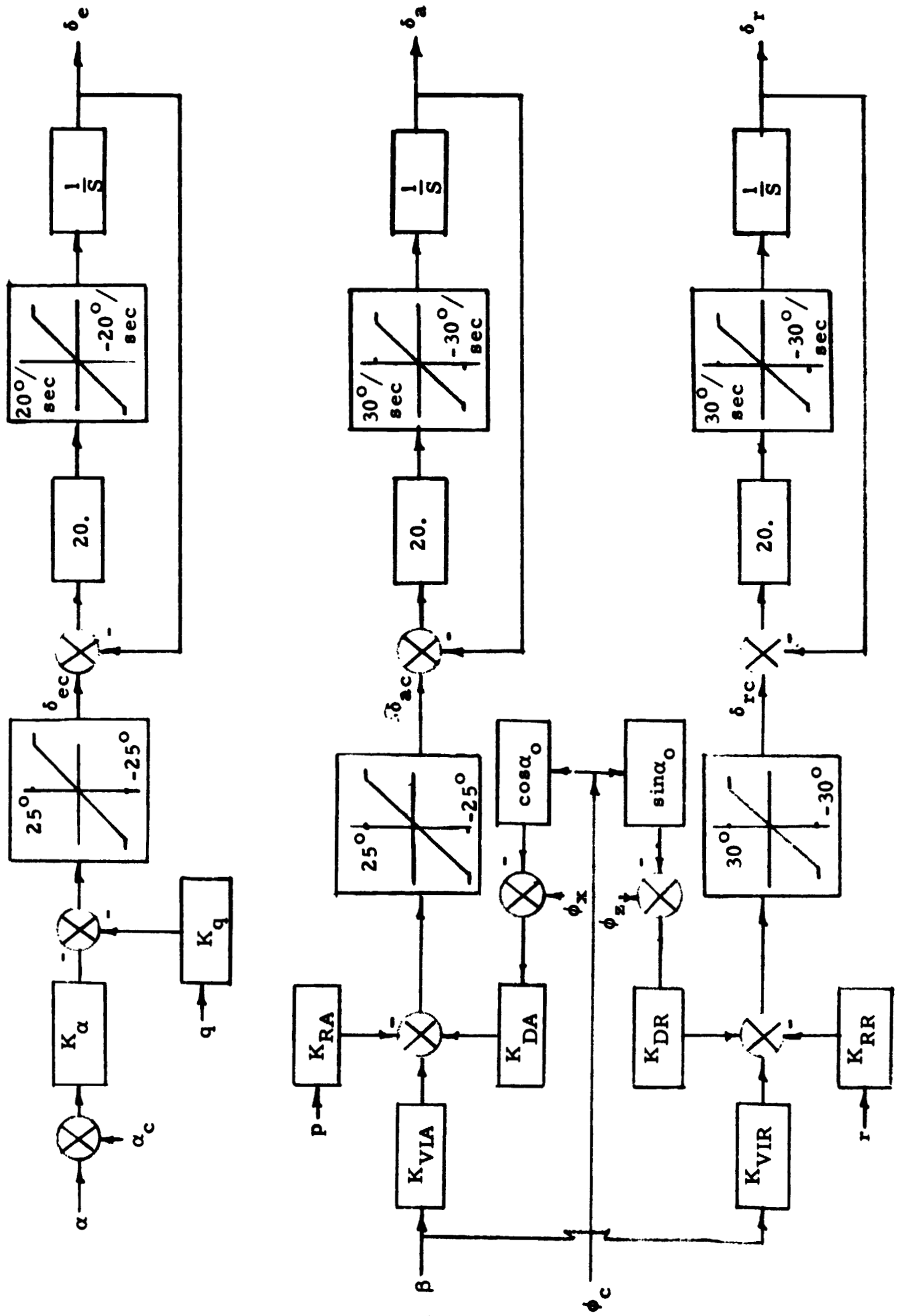

Fig. 6.2-3a - Booster Reentry Aero Controller Block Diagram Used in the Simulation and APS Optimization

where all APS control gains are used as the optimization parameters for the minimization of the performance index J. Figure 6.2-3b shows the APS controller block diagram. The optimization was performed by optimizing the pitch feedback gains first. Then using the optimized pitch gains, optimizing yaw gains. Finally, using the optimized pitch and yaw gains, optimizing roll gains. The runs were performed at 100 and 1000 times real time. Table 6.2-1 shows the preliminary results of the hybrid computer optimization of the GDC/B-9U APS. The optimized results show that the difference between 100 times real time and 1000 times real time runs are very small. Therefore, the optimization runs can, in the future, be performed at 1000 times real time. Figure 6.2-4 shows the history of control moment required for each body axis during the final portion of optimization runs. Figure 6.2-5 shows the components of the performance function. $J_{(c)}$ is the sum of J_{error} and $J_{\dot{error}}$ shown in this figure. Figure 6.2-6 shows the simulation results using optimized APS gains. Figure 6.2-7 shows the history of control moment requirements for nonoptimized and optimized APS firings. From these figures, it is seen that a marked improvement in control performance and a sizeable minimization in fuel consumption has been achieved. The resulting optimum APS laws for the alternating pulse type disturbances are

$$E_x = 0.9\,(\phi_x - \phi_{xc}) + 0.95\,p$$

$$E_y = 0.53\,(\alpha - \alpha_c) + 0.99\,q$$

$$E_z = 1.42\,(\phi_z - \phi_{zc}) + 2.41\,r$$

where angles are in degrees and rates in degrees/second.

Figure 6.2-8 shows the simulation results with alternating pulse type of pitch and bank commands which are equivalent to a triangular wave of pitch and bank commands. These pulses have a pulse height of 0.04 degree and a pulse width of 50 sec. The vehicle is seen to respond to rate command fairly closely.

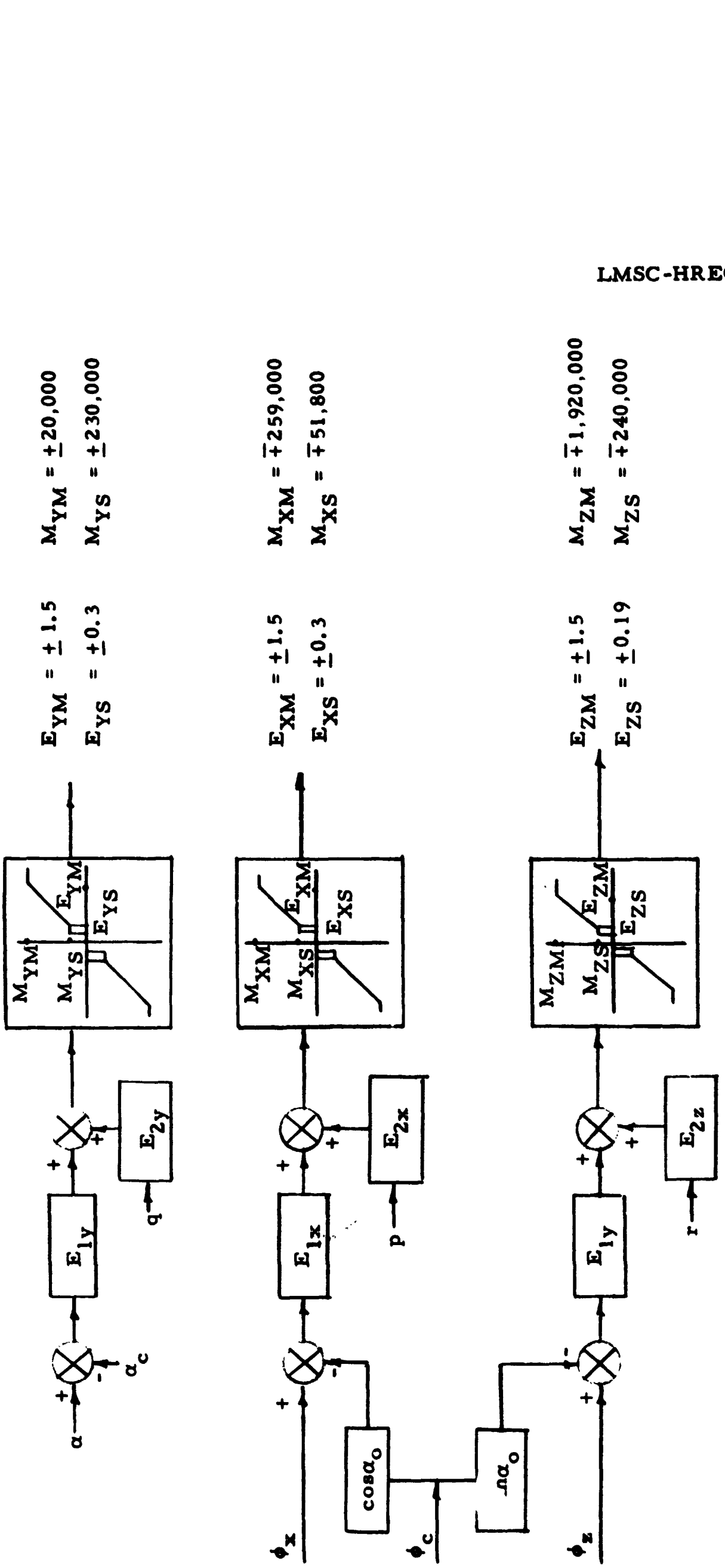

Fig. 6.2-3b - Booster Reentry APS Controller Block Diagram Used in the Simulation and APS Control Gain Optimization

Table 6.2-1

PRELIMINARY RESULTS OF HYBRID COMPUTER OPTIMIZATION OF GDC/B-9U

Run Code	Command	Grid Points	Optimized Parameters		Starting Point		Grid Spacing		Run Speed	Minimum J	Optimized Value	
A_{1000}	None	6 x 6	K_{1y}	K_{2y}	0.1	0.1	0.2	0.2	1000 X	0.11		
P_{100}	Alternate Pulse	16 x 16	K_{1y}	K_{2y}	0.25	0.25	0.06	0.06	100 X	0.5	0.53	0.99
P_{1000}			K_{1y}	K_{2y}	0.25	0.25	0.06	0.06	1000 X	0.52	0.49	0.91
Y_{100}			K_{1z}	K_{2z}	0.50	0.50	0.12	0.12	100 X	0.47	1.42	2.41
Y_{1000}			K_{1z}	K_{2z}	0.50	1.0	0.12	0.12	1000 X	0.47	1.5	2.52
R_{100}			K_{1x}	K_{2x}	0.50	0.8	0.12	0.12	100 X	0.47	0.90	0.95
R_{1000}			K_{1x}	K_{2x}	0.7	0.7	0.12	0.12	1000 X	0.48	0.82	0.92
$P_{dh_{100}}$		6 x 6	*	**	0.05	0.05	0.1	0.1	100 X	0.48	0.05	0.05

*Pitch deadband.

**Pitch Hysteresis.

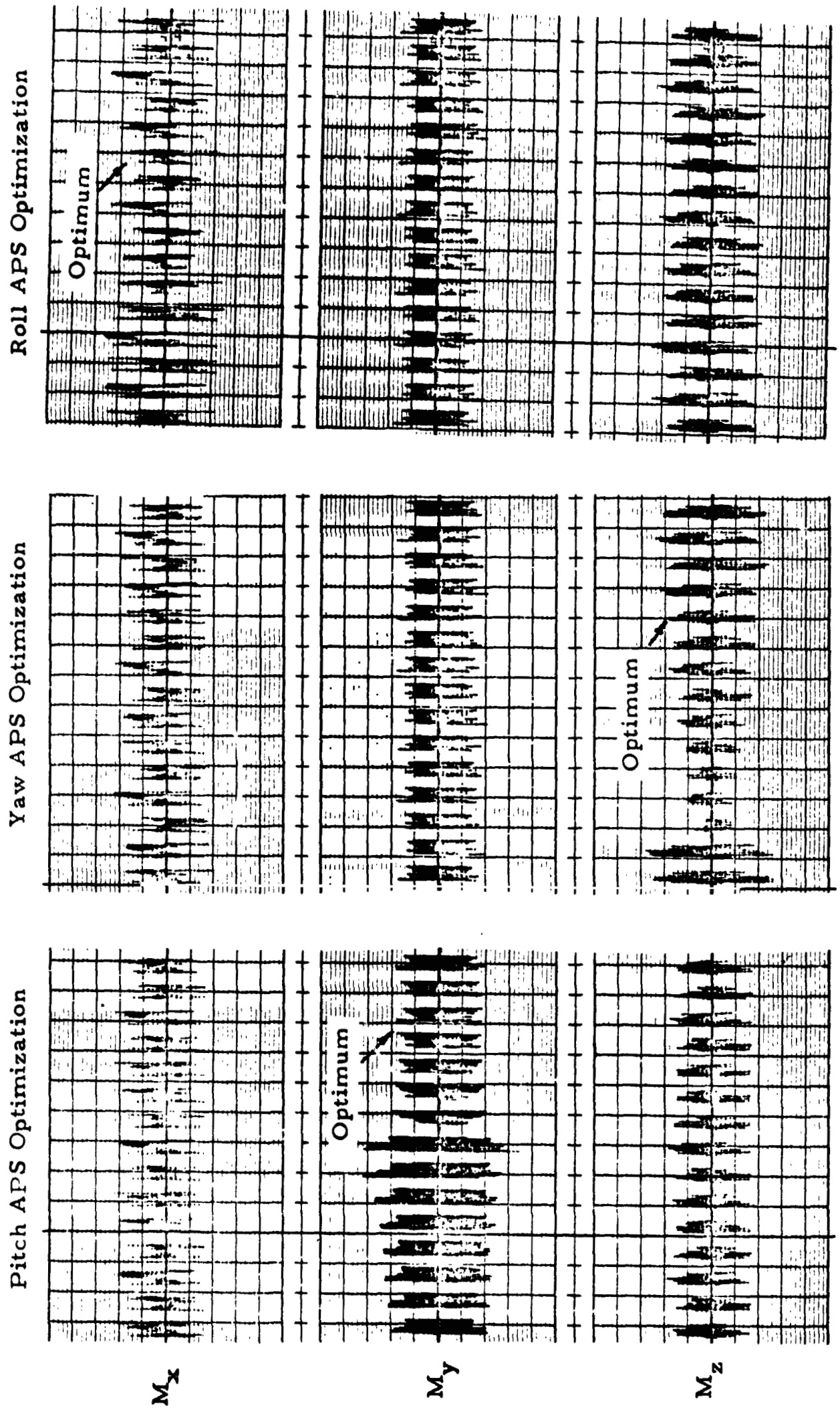

Fig. 6.2-4 - APS Optimization (Fuel Consumption and Response)

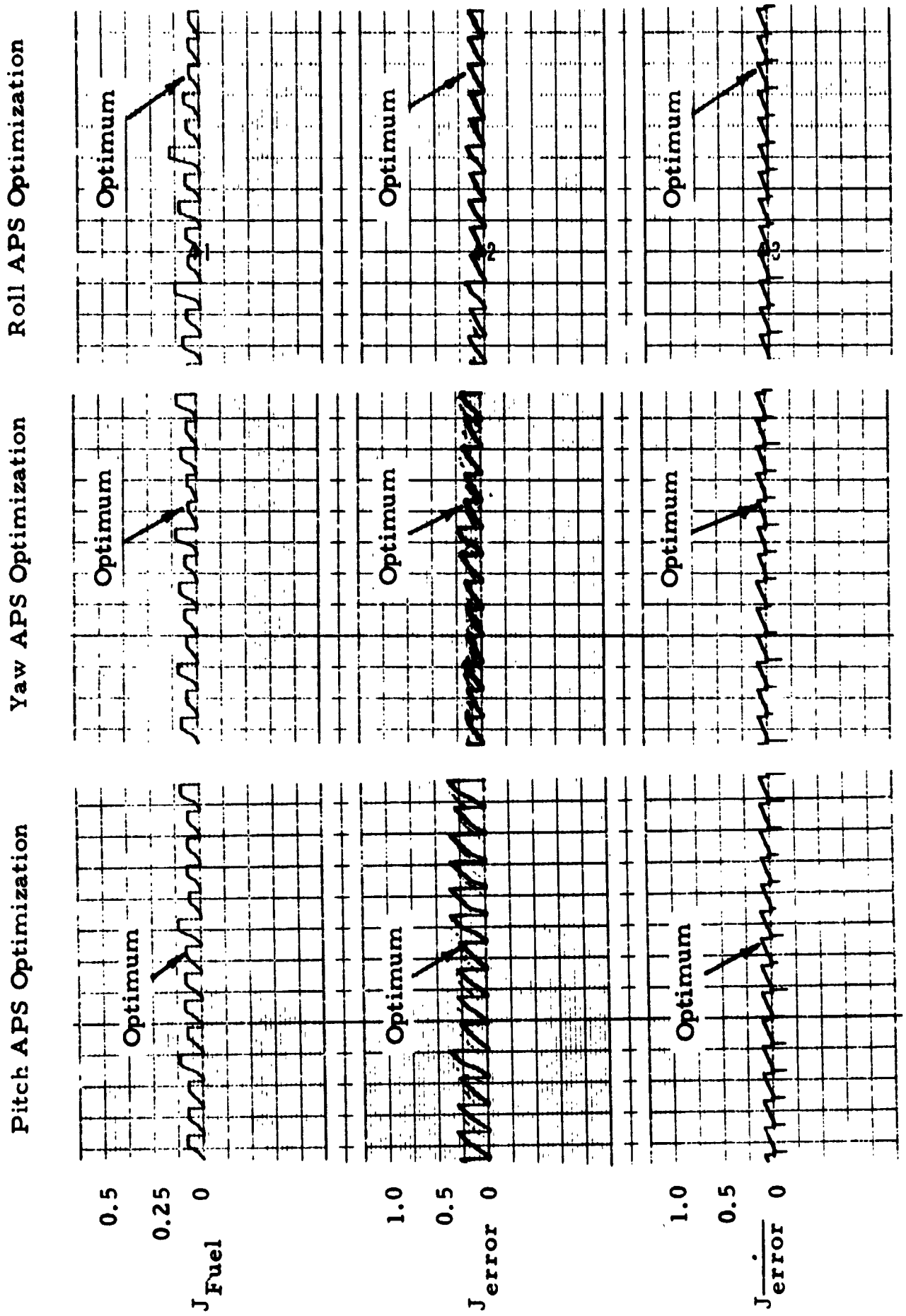

Fig. 6.2-5 - APS Optimization (Components of Performance Index)

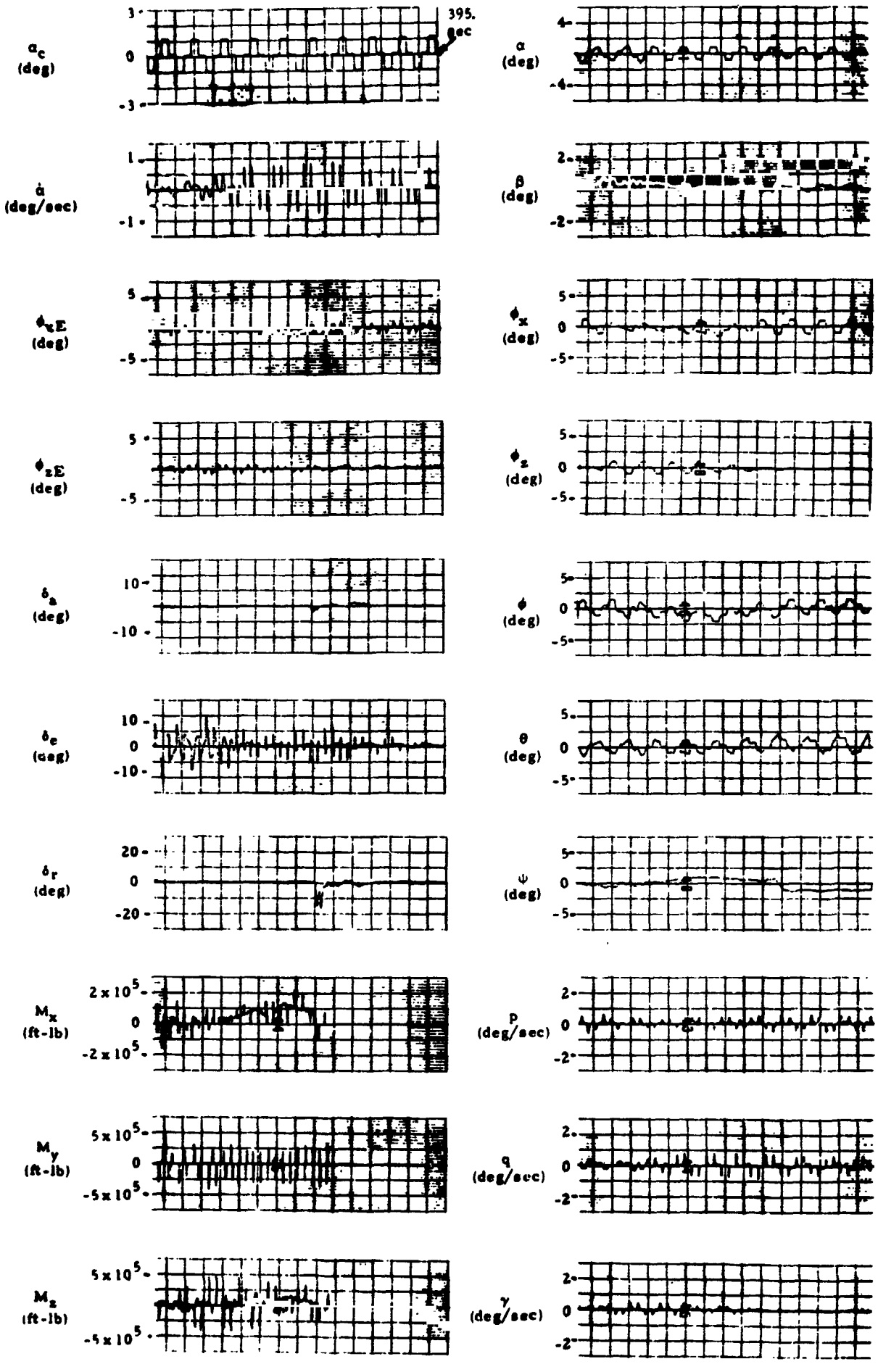

Fig. 6.2-6 - GDC/B-9U Two-Degree Alternating Pulse Perturbation Response During Reentry to 395 Sec After Separation Using the Optimized APS Gains. (APS turned off at 240 sec and operated by linearized switching lines. Lateral aero-controller turned on at 220 sec. Elevons in operation through reentry.)

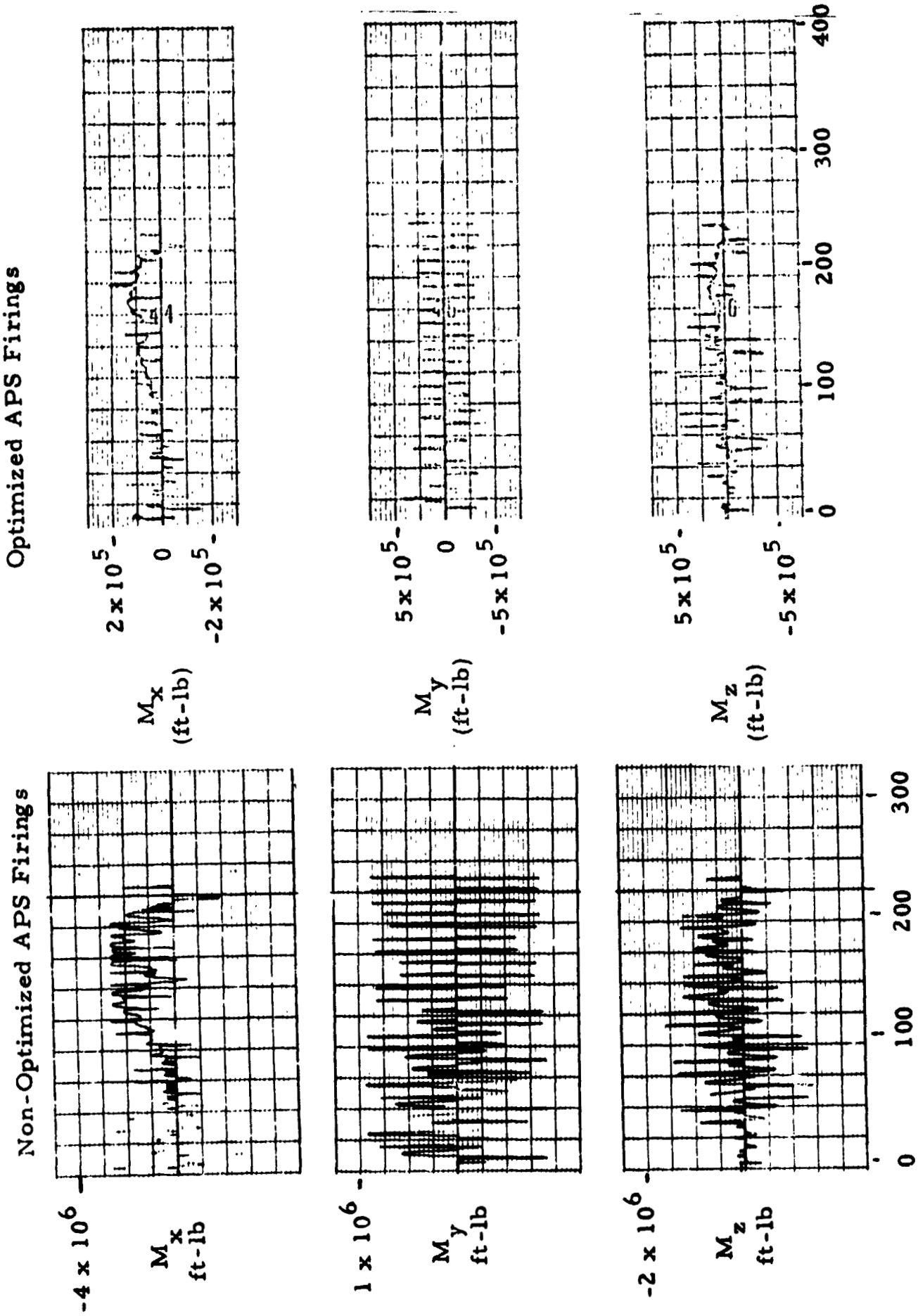

Fig. 6.2-7 - Optimized and Nonoptimized Control Moment Requirement

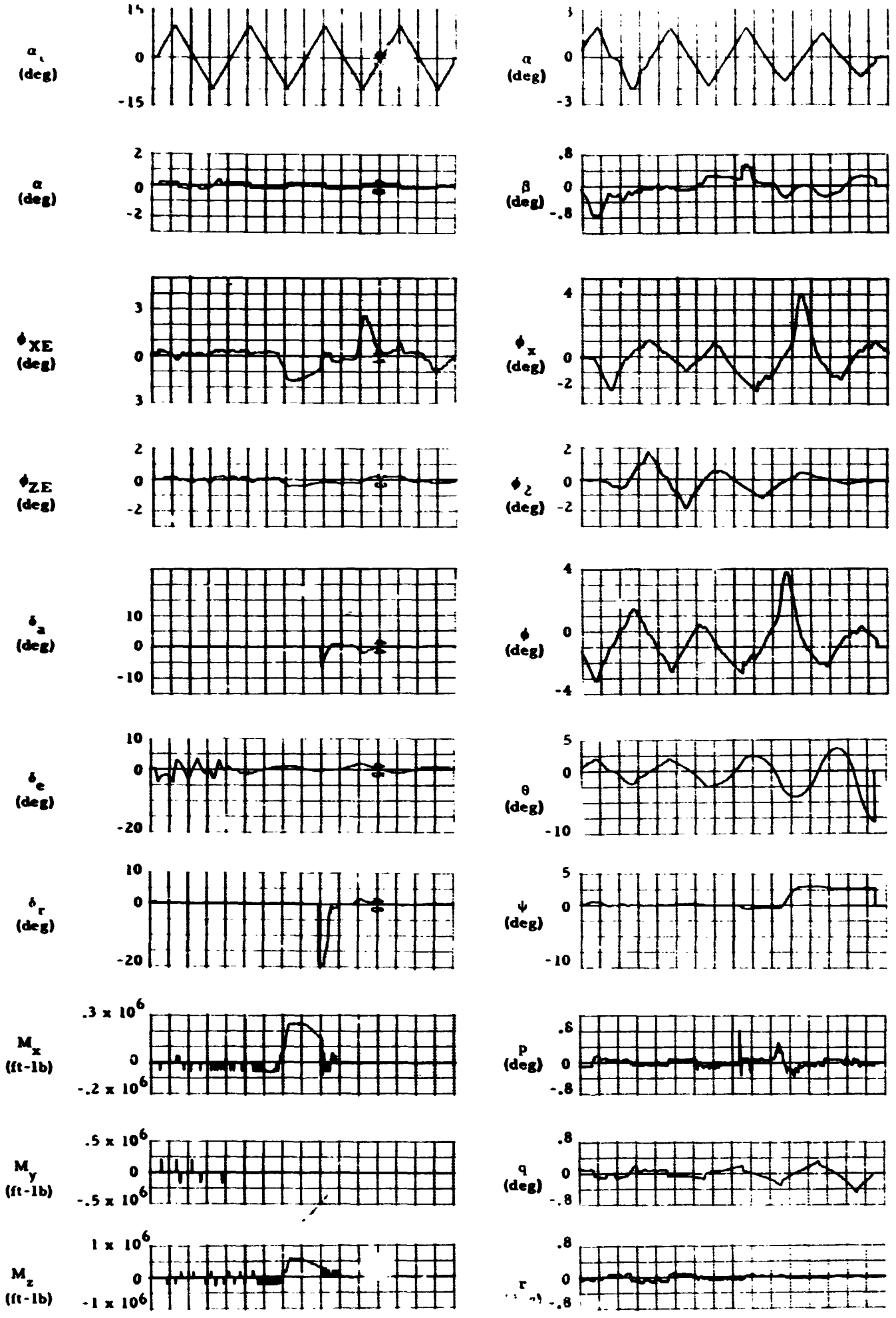

Fig. 6.2-8 - GDC/B-9U Two-D[illegible]ngular Wave Perturbation During Reentry. (APS t[illegible] 240 sec and operated by linearized switching lines. Lateral aero-controller turned on at 230 sec.) Elevons in operation throughout reentry.)

Section 7
CONCLUSIONS AND RECOMMENDATIONS

A practical design tool, which combines realistic simulation of vehicle and control system dynamics with an iterative gradient minimization scheme for near-optimal adjustment of design parameters, has been developed to perform the required tasks (Appendix I). The designer is only required to formulate the design objectives in meaningful engineering terms. This often requires close cooperation and cross talk between engineers and various fields to provide and integrate the necessary data for performance evaluation. The optimal designs evolving from such a broad multi-disciplinary effort then account for all the major and often conflicting systems aspects early in the design. Therefore, extensive use of this tool can contribute to a more economical design due to this total systems approach practiced at an early development stage.

A major shortcoming of this design approach is its initial development stage, namely the time-consuming tooling-up effort for each new application has been overcome after various preprocessor programs have been developed to operational status during the study for quick reduction of the trajectory, vehicle configuration and environmental data into a suitable form for control gain schedules synthesis, as well as hybrid and digital simulation. Although the development of these general purpose service programs has hampered the progress in hybrid optimization and simulation, a very efficient and versatile design tool has now been brought to operational status which is readily applicable to a wide class of new low-cost shuttle concepts.

The requirements for blending aerodynamic surface and TVC system to achieve control of the composite launch vehicle have been investigated. A blending logic to achieve integrated control of the vehicle has been studied and optimized for maximum payload. Analytical studies have been performed

to determine APS/aerodynamic reentry control effectiveness and the optimum blend of APS and aerodynamic control. Blending logic and control system related weight penalty functions and their sensitivities have been derived and analyzed. Optimal adjustments for major APS control system parameters were obtained.

7.1 ASCENT

The major advantages of this design technique became evident in the analysis of the space shuttle ascent control requirements for blending aerodynamic surface and thrust vector control.

The true total systems approach was required to identify important tradeoffs and parameters influential to configuration design. The maximization of all payload affected by the ascent control system was therefore chosen as the overriding design goal and a corresponding performance criterion was formulated. It consisted of the sum of all major payload penalties that are affected by ascent control system performance. These included structural weight penalties as indicated by the dynamic loads transmitted through the booster/orbiter attachment points, weight penalties associated with engine gimbal angle requirements, aerosurface hinge moments and trajectory deviations in position and velocity.

In the course of the computerized design and optimization studies, substantial reductions in these payload penalties were achieved in the commonly most critical flight region of high dynamic pressure in the order of 1200 kg. At a later flight regime when atmospheric disturbances have virtually tailed off, a trajectory and configuration dependent region of high structural loads was identified which is almost insensitive to controller design. Payload gains of more than 2000 kg could be realized if the trajectory or configuration design were modified. Such a finding proves the merits of this multidisciplinary total system design approach where flight and control system dynamics, structural loads, and trajectory performance characteristics are simultaneously considered during early stages of vehicle design.

The pitch plane blending studies showed the elevons assisting the gimbaled engines in allowing the vehicle to rotate more freely into the wind. One adverse effect was noted during this study – it being an increase in magnitude of the gimbal angle when the elevons were blended in. A brief analysis indicated this might be caused by rapid transients of the engines being superimposed on the nominal response since the engines are able to react much faster than the larger elevon surfaces. Selection of different feedback laws for aerodynamic and TVC control would probably improve the engine gimbaling response. More study in this area would be needed to improve these transient response characteristics.

7.2 REENTRY

A hybrid computer program for reentry studies has been developed. The major features built into this program are: flexible on-line engineering interface, high-speed operation, and applicability to a wide range of vehicle configurations and trajectories.

Several other hybrid computer service programs have been developed to speed up and to computerize the preparatory processes prior to hybrid computation.

Hybraulic system related weight penalties are sensitive to elevon and rudder maximum deflection rates and deflections in the reentry flight from 340 sec to 395 sec after separation, but thermal protection system and structural weight penalties are insensitive for the entire reentry flight.

Phase plane design of the digitized APS control system is very attractive for the APS control dominant region. It provides optimum switching curves which can be implemented by a simple digital computer program. The switching curves are time optimal in the sense of eliminating small system errors in the minimum period of time corresponding to the minimum torque level by a single switching. For large errors, a tradeoff is made

between time-optimal and minimum fuel switching. Large errors are initially reduced in a time-optimal manner to a lower level, followed by a gradual reduction in control torque magnitude to save fuel.

The linearized APS design approach is particularly convenient in producing APS gain schedules for the transition regime with both APS and aerodynamic control effective. It is capable of producing "in phase" operation with a linear aerodynamic surface control system and provides a method to tailor the APS control to the desired closed-loop characteristics. A smooth transition from APS control to aerodynamic control can be achieved in a straightforward design approach.

By using augmented characteristic equations, the desired closed-loop characteristics can be obtained by using a digital computer to compute appropriate gain feedbacks. The computed gain schedules for the entire ascent or reentry can provide a controlled system with fixed characteristics.

The mixed control system operation logic for blending APS and aerodynamic control has a higher controlability and flexibility, and has lower fuel expenditure. However, the operation logic is considerably more complex.

The hybrid simulation runs at 1000 times real time yield very accurate results. This hybrid optimization and simulation program can be used for additional feedback gain schedule synthesis (other than the basic feedback gains for initially stabilizing the vehicle) to meet special control and stability requirements.

A variety of realistic excitations during reentry such as cg-offsets and a variety of likely guidance commands should be used in the hybrid optimization and simulation so that the resulting optimum control system will be capable of compensating for a wide range of disturbances.

Phase plane design of the APS control system in the transition regions should be investigated further in order that the inherent nonlinear effects of the digitized APS control are accounted for in the design.

The effects of hysteresis on the design of optimum response switching curves for the digitized APS control system should be analyzed so that excessive APS firings due to limit cycle behavior can be minimized or eliminated.

Practical experience and limitations on the control gains should be incorporated into the control gain synthesis procedure so that realizable control gain schedules for the desired dynamic characteristics are obtained.

This hybrid optimization and simulation program can be used to perform vehicle handling quality design based on a model reference system (exhibiting desired handling qualities) used in conjunction with a performance index that penalizes model-following errors.

Section 8
REFERENCES

1. Trautwein, W., and J. G. Tuck, "Control System Optimization for Saturn V Launch Vehicles Using Gradient Techniques," Final Report, LMSC-HREC A791836, Lockheed Missiles & Space Co., Huntsville, Ala., October 1968.

2. Connor, C. L., and W. Trautwein, "The Application of Optimal Control Technique to Advanced Manned Missions," LMSC-HREC D225541-I and -II, Lockheed Missiles & Space Co., Huntsville, Ala., February 1972.

3. Lockheed Missiles & Space Co., "Contract NAS8-26772, 'Study of Aerodynamic Surface Control of Space Shuttle Boost and Reentry,' Monthly Progress Report," LMSC-HREC D225313, Huntsville Research & Engineering Center, Huntsville, Ala., 18 August 1971.

4. "Space Shuttle Program Phase B Final Report — Technical Summary," Report MDC E0308 Part II, McDonnell Douglas Corp., St. Louis, Mo., 15 March 1971.

5. Anderson, H. A., "Booster Hydrogen Tank Cylinder Design," Design Note B-WEST-STR-3, McDonnell Douglas Corp., St. Louis, Mo., 16 September 1970.

6. Wright, F. M., "Minimum Weight Design of Flanged Isogrid Cylinders in Compression," Design Note B-WEST-STR-7, McDonnell Douglas Corp., St. Louis, Mo., 11 September 1970.

7, Amick, J. L., and Paul B. Hass, "Interaction Effects of Side Jets Issuing from Flat Plates and Cylinders Aligned with a Supersonic Stream," WADD TR-60-329, University of Michigan, Ann Arbor, June 1960.

8. Giles, H. L., and J. W. Thomas, "Analysis of Hypersonic Pressure and Heat Transfer Tests on a Flat Plate with a Flap and a Delta Wing with Body, Elevons, Fins and Rudders," NASA CR-536, The Boeing Company, Seattle, Wash., August 1966.

9. Pate, S. R., "Investigation of Flow Separation on a Two-Dimensional Flat Plate Having a Variable-Span Trailing Edge Flap at $M = 3$ and 5," AEDC-TDR-64-14, Von Karman Gas Dynamics Facility, ARO, Inc., Arnold Air Force Station, Tenn., March 1964.

10. Greenwood, D. T., Principles of Dynamics, Prentice-Hall, Inc., Englewood Cliffs, N. J., 1965.

11. "Dynamics of the Airframe," Northrop Norair, September 1952.

12. Etkin, B., Dynamics of Flight-Stability and Control, John Wiley & Sons, Inc., New York, 1963.

13. Tore, J. T., Digital and Sampled-Data Control Systems, McGraw-Hill Book Co., Inc., New York, 1959.

14. Del Toro, V., and S. R. Parker, Principles of Control Systems Engineering, McGraw-Hill Book Co., Inc., New York, 1960.

15. Truxal, J. C., Control System Synthesis, McGraw-Hill Book Co., Inc., New York, 1955.

16. Merriam, C. W., Optimization Theory and the Design of Feedback Control Systems, McGraw-Hill Book Co., Inc., New York, 1964.

17. McRuer, D., Analysis of Nonlinear Control Systems, John Wiley & Sons, Inc., 1961.

18. Clark, D. C., "The Model Reference Self Adaptive Control System as Applied to the Flight Control of a Supersonic Transport," Proc. Joint Autom. Control Conf., Stanford, Calif., 1964.

19. Whitaker, H. P., "The MIT Adaptive Autopilot," Proc. Self Adaptive Flight Controls Symp., Wright Air Development Center, Wright-Patterson AFB, Ohio, January 1959.

20. Wolowicz, C. H., "Considerations in the Determination of Stability and Control Derivatives and Dynamic Characteristics from Flight Data," Report 549, AGARD, 1966.

21. Ashkenas, I. L., and D. T. McRuer, "Approximate Airframe Transfer Functions and Application to Single Sensor Control Systems," WACD TR 58-82, Wright-Patterson Air Force Base, Ohio, June 1958.

22. Bekey, G. A., and J. Karplus Walter, Hybrid Computation, John Wiley & Sons, Inc., New York, 1968.